Numerical and Analytical Multiscale Modeling of High Cycle Fatigue in Advanced Materials

by

Shardul Singh Panwar

A dissertation submitted in partial fulfillment
of the requirements for the degree of
Doctor of Philosophy
(Aerospace Engineering)
in The University of Michigan
2018

Doctoral Committee:

Associate Professor Veera Sundararaghavan, Chair
Professor John E. Allison
Professor KrishnaKumar R. Garikipati
Professor J. Wayne Jones
Professor Anthony M. Waas

[The Columbia (NX-02) undergoing construction in 2153. (Star Trek: Enterprise episode:"The Expanse")] [1].

Shardul Singh Panwar

sspanwar@umich.edu

ORCID iD: 0000-0002-5379-9472

To my mom, Satya Panwar

ACKNOWLEDGEMENTS

First, I would like to thank my advisor Prof. Veera Sundararaghavan for supporting me during my course of study at the University of Michigan. He allowed me the freedom to pursue my research interests, and he has been a constant source of optimism.

I would like to thank Professors Krishna Garikipati, John Allison, J. Wayne Jones, and Anthony M. Waas for taking the time to be on my committee. Prof. Krishna Garikipati taught the course on advanced finite element methods and kindly answered my questions related to the variational multiscale method. I am grateful to Prof. John Allison for letting me be a part of the PRISMS's student community. I would like to thank Prof. J. Wayne Jones for giving me helpful insights on fatigue and for his guidance. I am thankful to Prof. Anthony M. Waas for teaching the course on the mechanics of composite structures and for allowing me to conduct research in his lab during the summer of 2012. I would also like to thank Prof. John Shaw for supervising my independent study on NiTi tubes during the first semester of my aerospace masters program and Prof. Carlos E. S. Cesnik for supervising my independent study on low velocity panel flutter of thin membranes during the second semester of my aerospace masters program.

I am very grateful to Dr. Umesh Gandhi for allowing me to do co-ops at Toyota Technical Center and giving me a valuable industrial research experience.

The financial support for the dissertation was provided by the U.S. Department of Energy, Office of Basic Energy Sciences, Division of Materials Sciences and Engineer-

ing under Award no. DE-SC0008637 that funds the PRedictive Integrated Structural Materials Science (PRISMS) Center at the University of Michigan, and I would like to thank them for this support.

I would like to thank Jacob Adams for providing the experimental data used in this dissertation. I would also like to thank Multiscale Structural Simulations Lab's former and current group members: Aaditya, Abhishek, Adam, Ali, Arunabha, Christian, Iman, Jiangyi, Nick, Pinar, Shang, Siddhartha, Srihari, and Sriram for their support. I would like to thank my friends Prerit, Anna, Nhung, Puneet, Rohit, Yuki, and Kyle for making this a wonderful journey. I would like to thank my friends Shishir and Shalab in India for their support. I am very grateful to Denise Phelps for her help and support throughout this process.

A special thanks goes to my spouse Corin (Corey) Bowen who spent countless hours proofreading my papers and this dissertation. My journey would have been very difficult and incomplete without her. Our dog Sophie also deserves a special thanks for her unconditional love and support. I would like to thank my in-laws Frank and Donna Bowen for being really wonderful people and Mattie for being a supportive sister-in law. I would also like to thank my brother Shivender Singh Panwar and his family for supporting me through this journey.

Lastly and most importantly, I would like to thank my dad Surender Singh Panwar for igniting my passion in engineering at an early age and my mom Satya Panwar for the hard work she did over the past two decades to help me get to this point in my career.

TABLE OF CONTENTS

LIST OF FIGURES

Figure

LIST OF TABLES

Table

LIST OF APPENDICES

Appendix

ABSTRACT

Integrated Computational Materials Engineering (ICME) approaches are gaining popularity in various industries, such as electronics, automobile, and aerospace, due to their focus on multiscale simulation-based design and analysis. The multiscale approach is especially useful for fatigue modeling of advanced materials that have different local structure-property relationships at different length scales. Broadly, fatigue crack growth is classified into the following categories: crack initiation (atomic-scale), microstructurally short crack growth (micro-scale), physically short crack growth (meso-scale), and long crack growth (macro-scale).

In this dissertation, we develop numerical and analytical models to primarily predict microstructural effects on fatigue crack growth and subsequent long crack growth behavior. In the macro-scale, the new contribution is a variational multiscale cohesive method (VMCM) to determine the fatigue crack growth rates in the long crack growth regime. The calibration of the macro-scale VMCM cohesive parameters, which represent the crack tip mechanics, is addressed with the development of a linear elastic fracture mechanics (LEFM)-based irreversible cohesive model. The LEFM-based irreversible cohesive model is validated with macro-scale experiments. The model also provides a way to link the cohesive parameters with micro-scale experiments. In the micro-scale, we develop a VMCM approach that incorporates local microstuctural information, such as grain orientations and slip systems, and predicts the microstructurally short crack growth paths through slip planes that are in multiple grains and across grain boundaries. We employ dislocation theories to calibrate the microstructural cohesive parameters. This dislocation theory-based cohesive model

efficiently predicts the microstructurally short fatigue crack growth rates through multiple grains. The calibration of this model is done with micro-scale experiments on a single crystal and on a polycrystalline modification of a Ni-based CMSX-4 alloy.

For a microstructurally short crack, the local microstructure plays an important role in the fatigue behavior of the material. Thus, for accurate representation of the mechanisms happening at the crack front, microstructural barriers such as grain boundaries have to be taken into consideration. This mechanism of crack plane-grain boundary interaction is addressed next with the development of a phenomenological grain boundary interaction model. This model takes into account the coupling between the tilt and twist misorientations (located between the crack plane and a favorable plane in the next grain and calculated at a grain boundary), the Schmid factor, and the critical crack transmission stress, which is a form of a microscopic stress intensity factor. However, these two-dimensional models can only give information about the surface crack growth rates. The last chapter extends a three-dimensional microstructurally short fatigue crack growth model in order to better understand the sub-surface crack interactions with multiple grain boundaries. This method is utilized to model two cases of microstructurally short fatigue crack-grain boundary interactions in a magnesium WE43 alloy: the interaction of a crack front growing towards a grain boundary with the grain boundary and the interaction of a crack front spanning across multiple grains with the grain boundary it crosses. Thus, the tools developed in this dissertation aid in improving our understanding of the interaction between the microstructurally short fatigue crack growth and the local microstructure.

CHAPTER I

Introduction

The increase in the demand for lightweight high strength materials in aerospace, automobiles, electronics, and other industries has led to an increased rate of material discovery. This has increased the demand for closely linked experiments and numerical methods to model the behavior of these advanced materials. In recent years, this has resulted in an entirely new field that closely integrates materials science experiments with computational models at multiple length scales called Integrated Computational Materials Engineering (ICME). Horstemeyer [2] describes ICME as a new simulation-based tool that employs hierarchical multiscale methodology for the optimization of load-bearing structures.

[1]In the mid-1980's to early 1990's, multiscale methodology was born out of effort from the United States Department of Energy national labs to reduce and eliminate the need for underground nuclear tests. After the Comprehensive Test Ban Treaty of 1996, the large-scale system level tests were discarded completely and replaced with simulation-based design and analysis tools. Thus, parallel computing and multiscale modeling were brought into main-stream research focus. Multiscale modeling approaches also shifted experimental paradigms from large-scale tests to multiscale

[1]Reproduced from Mark F Horstemeyer. *Integrated Computational Materials Engineering (ICME) for metals: using multiscale modeling to invigorate engineering design with science.* John Wiley & Sons, 2012

tests that provide material models at different length scales. If the modeling and simulations were physically based and less empirical, then a predictive capability could be realized for other conditions.

In the case of the modeling of materials, depending on the industrial application, the multiscale modeling approaches have been called by different names, such as "Atoms to Auto" [2] and "Atoms to Airplanes" [3]. Generally, multiscale modeling is divided into following length scales: macro-scale (10^1 to 10^{-3} m), micro-scale (10^{-3} to 10^{-6} m), nano-scale (10^{-6} to 10^{-9} m), and sub-atomic scale ($< 10^{-9}$ m). Thus, multiscale modeling approaches deal with the individual length scale models and the information transfer that happens between the length scales.

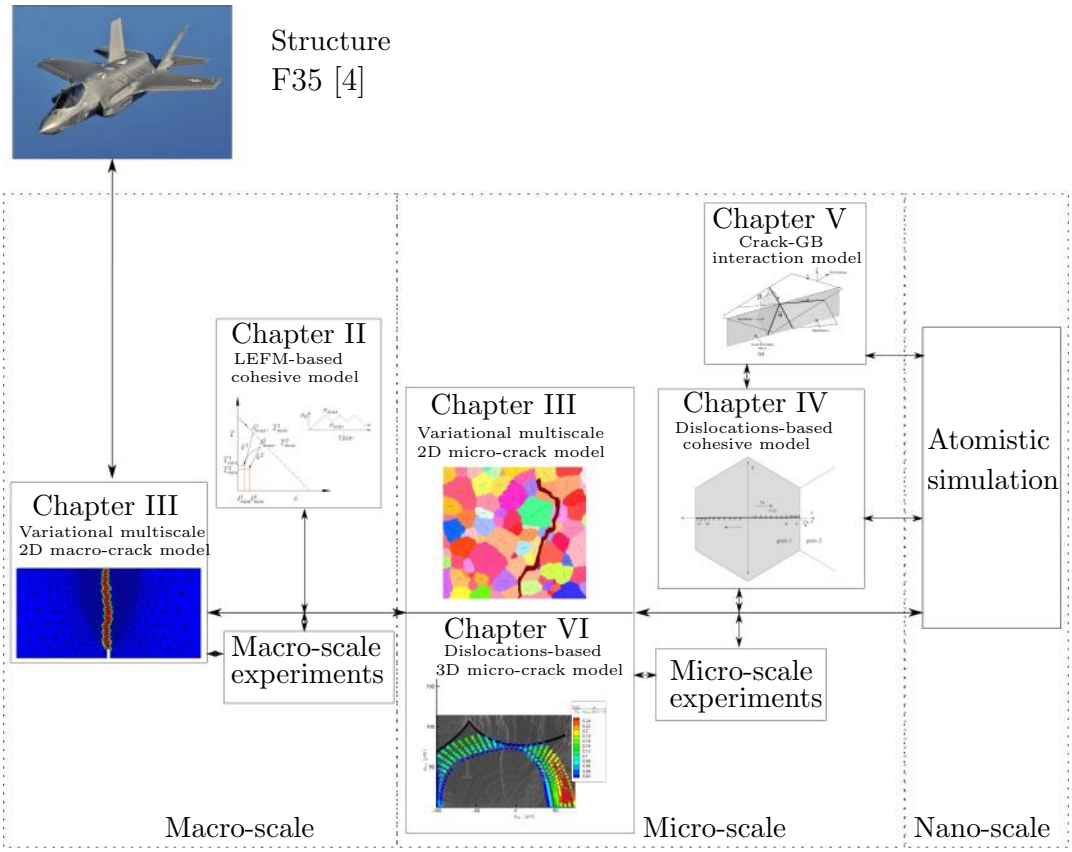

Figure 1.1: Multiscale modeling framework for fatigue response

In this dissertation, we develop analytical and numerical models that address mechanisms happening at some of these length scales and the linkages between them.

Before we proceed with the introduction to each chapter, we present in Figure 1.1 a graphical representation of the connections between the chapters.

In the case of fatigue, there are different length scales of interest, such as the length scale of local inclusions or defects, which induce local stress concentrations that eventually give rise to fatigue cracks, and the short crack length scale, in which grain boundaries can cause short crack growth to retard or even arrest. This difference in length scales due to fatigue crack initiation, short crack growth, and long crack growth was first addressed by Lankford et al. [5, 6]. Further research into the short crack growth length scale led to its classification into two separate regimes [7, 8]: microstructurally short cracks and physically short cracks. The microstructurally short crack regime covers the crack growth from crack initiation to a few microstructural dimensions (e.g. grain diameters). Thus, in this regime, the crack growth is strongly influenced by microstructural features, such as grain boundaries, inclusions, and precipitates. After this, the crack growth enters the physically short crack growth regime, which covers crack growth until the length of the crack is smaller than the smallest specimen dimension.

Traditionally, for the long crack growth regime, linear elastic fracture mechanics (LEFM) has been used to predict material failure. The LEFM approach is based on Griffith's [9] energy-based and Irwin's [10] stress intensity factor-based theories of failure, among others. In LEFM, the crack tip stress singularities resulting from linear elasticity theory are assumed to lie in a small region in front of the crack tip. These stress singularities are theoretically linked to the actual finite stresses that occur in the physical material through a fracture parameter called the stress intensity factor. The basis of LEFM is the assumption that this small region in front of the crack tip contains the crack tip nonlinearities and produces little effect on the global energy or stresses. The LEFM approach has been very successful in predicting the strength of engineering structures. For failure due to cyclic loading, Paris et al. [11, 12] in

their pioneering work suggested a relationship between Irwin's stress intensity factor (ΔK) and the rate of crack growth per cycle. This relationship is written as

$$\frac{da}{dN} = C(\Delta K)^m \tag{1.0.1}$$

where C is the intercept of the curve and m is the slope. The above equation (Eq. 1.0.1), called the Paris Law, is a phenomenological relationship between LEFM-based local notch parameters and the fatigue life. In the long crack growth regime, the Paris Law can quantify experimental fatigue crack growth rates under idealized conditions of small scale yielding and constant amplitude loading [13]. In the years since the introduction of the Paris Law, it has undergone a number of modifications to make it applicable to a wide range of conditions, such as crack closure [14], variable amplitude loading and overloads [15], and small cracks [16]. Most of these modifications are based on LEFM; thus, they are not able to capture the physical mechanisms happening at the crack tip. To overcome some of the limitations of LEFM, Dugdale [17] in 1960 and Barenblatt [18] in 1962 independently proposed nonlinear cohesive theories that have become the foundation of cohesive zone models (CZM). Dugdale's model assumes that all the plastic deformation is localized inside a zero-width zone in front of the crack tip called the strip yield zone. Inside this zone, the upper and lower surfaces of the strip are held together by a constant stress equal to the yield stress of the material. Barenblatt's model, however, assumes a small cohesive zone behind the crack tip in which the upper and lower surfaces are held together by a cohesive traction with a magnitude on the order of the theoretical strength of the material. In an asymptotic sense, Willis [19] has shown the equivalence between Barenblatt's modulus of cohesion and Griffith's surface energy. In Dugdale's model, the strip yield zone can be treated as a cohesive zone with a constant surface traction. Generally speaking, in cohesive zone models, the fracture process is represented in a phenomenological

form by the relationship between the surface traction and the displacement between the two surfaces. This relationship is called the traction-separation law. Hillerborg et al. [20] utilized the cohesive zone modeling approach in a computational framework to predict crack formation, growth, and failure in concrete. Their work led to the utilization of cohesive zone models in tackling more complicated problems using computers. There is an enormous body of research focused on developing cohesive zone models for computational fracture mechanics; some of these efforts can be found in [21, 22, 23, 24, 25]. For monotonic failure, Zin and Sun [26] used LEFM to derive a cohesive relationship from a first order approximation of necking in metals. They show that, if energy dissipation at the cohesive tip is not allowed, the cohesive zone model cannot assume a linear hardening law with a cohesive traction that is initially zero. On the other hand, energy dissipation at the cohesive tip can happen due to a variety of physical phenomena, such as cracking in brittle matrix composites' reinforcement [27] and unbroken ligaments during cleavage cracking [28]. The latter models are classified as crack bridging models. Budiansky et al. [27] applied LEFM to the crack bridging problem to determine the relationship between the fracture toughness and the bridge length of a ceramic composite at fracture. A good review of these two models and an extension of crack bridging models to fatigue is given in [29]. In the case of fatigue, there have also been numerous applications of cohesive zone models in metals [30, 31, 32], adhesive interfaces [33], and quasi-brittle materials [34]. One of the main features present in recent fatigue cohesive zone models is the hysteresis between the loading and the unloading parts of the traction-separation law [32, 34, 33]. This hysteresis represents dissipative mechanisms, such as crystallographic slip [35] and frictional wear at bridge/matrix boundaries [36], and prevents elastic shake-down [32].

In Chapter II, we use a two-parameter phenomenological irreversible cohesive model by Maiti and Geubelle [37] with LEFM in order to develop an LEFM-based

fatigue cohesive model, which enables the progressive degradation of the cohesive zone strength during reloading events while the unloading is assumed to be elastic. The advantages of this model are simplicity, fast calibration, and good predictive capability under ideal small-scale yielding conditions. This framework allows us to quickly calibrate the fatigue cohesive parameters from macro-scale experiments.

In the context of the finite element method (FEM), the framework of the Galerkin-based traditional FEMs are not particularly suited to solve a boundary value problem with a crack or multiple cracks inside the domain. This is due to limitations such as spurious mesh-related length scales [38, 39] and the requirement that the mesh be aligned relative to the strain localization band [40, 41], which has kinematics similar to those of the crack boundaries. In recent years, however, a whole new class of finite element methods has emerged that can solve the problem of new boundaries emerging inside a domain without experiencing any of the limitations of traditional FEMs. Depending upon how these new boundaries are embedded in the finite element framework, these methods are broadly classified into two families: node enrichment FEM (e.g. X-FEM) and elemental enrichment FEM (e.g. E-FEM). Between these two families, Oliver et al. [42] showed that, under similar conditions, X-FEM is more computationally expensive. Therefore, E-FEM would be a favorable option for problems requiring more computational time. One such problem is fatigue failure, in which crack growth can occur over millions of cycles, so computational solutions are very expensive (in terms of computing time). In addition, these methods need to include microstructural information through either homogenization methods [43, 44] or through concurrent multiscaling [45].

In Chapter III, we use a type of E-FEM introduced by Hughes [46] and referred to as the Variational Multiscale Method (VMM) by Garikipati [47]. VMM uses a multi-scale interpolation scheme to embed cracks into the continuum domain (representing discontinuities using a Heaviside function). The main advantage of the multiscale

interpolation scheme over the partition of unity interpolation scheme that is used in X-FEM is the local-to-element nature of the discontinuous displacement field. This means that the additional degree of freedom needed to represent the discontinuity will be condensed out at the elemental level, thereby leaving the sparsity pattern of the global problem untouched. This is why the computational cost of multiscale interpolation-based VMM (E-FEM) is less than the partition of unity interpolation-based X-FEM and why the former is more suitable for fatigue problems. To model the correct physical representation of the mechanics of the crack tip, we again use the two-parameter irreversible cohesive model developed by Maiti and Geubelle [37]. The coupling of a cohesive zone model with the VMM has been demonstrated by Rudraraju et al. [48]; they used a simple linear CZM inside the framework of the VMM to successfully demonstrate crack propagation in laminated fiber reinforced composites and showed experimental comparisons. However, the VMM has not yet been utilized in problems involving cyclic loading. Maiti and Geubelle used their cyclic irreversible cohesive model in the framework of the standard finite element method. However, the use of zero-volume elements or interface elements in the standard finite element framework makes this method dependent on the numerical discretization scheme. To solve this issue, we combine the fatigue cohesive model with the VMM to model fatigue crack growth behavior in the macro- length scale. VMM with an embedded cohesive zone model can also be used to model microstructurally short crack growth. In this chapter, we have shown an approach in which microstructural information, such as grain orientations and slip system traces on the surface of the specimen, are included in the finite element model. This approach produces a correct distribution of microstructurally short crack growth across crystallographic and grain boundary planes. However, using cohesive theory to accurately predict any failure process requires proper calibration of the cohesive model parameters. One approach is to fit the cohesive parameters to one or more experiment(s) and then use those fit-

ted parameters in a numerical simulation to predict other experimental results. Using this approach, uniaxial tensile tests can be used to determine the cohesive parameters for mode I fracture [49]. Another approach is to determine these parameters from a lower-scale calculation [50, 51]. In the next chapter, this latter approach is followed to determine the cohesive parameters for predicting microstructurally short fatigue crack growth rates.

In the case of microstructurally short fatigue crack growth, there are various models that have been proposed in recent years, such as Newman's crack closure model [52, 8] and models based on the explicit incorporation of microstructural features, such as grain boundaries and precipitates, and their interactions with the crack tip. Christ et al. [53] have classified these latter type of models into three categories: (1) empirically-based models that are informed and driven by experiments [54], (2) mechanism-based models, such as the Bilby-Cottrell-Swinden (BCS) model [55], the Taira-Tanaka-Nakai model [56, 57], and the Navarro-Rios model [58, 59, 60, 61], and (3) models based on discrete dislocations [62]. The mechanism-based models find their origin in the work of Bilby et al. [55]. The BCS model follows on the work of Head and Louat [63] and approximates the crack and the associated plastic zone by a continuous distribution of dislocations. In the BCS model, Bilby et al. [55] derived the plastic zone length for a macroscopic crack in an infinite domain and showed that their plastic zone expression is similar to the expression used in the cohesive zone models of Dugdale [17] and Barenblatt [18]. Cohesive zone models have also been used to study failure processes in other materials, such as ceramics [24], polymers [64, 65], and ductile metals [21]. A good overview of the application of cohesive zone models to the materials previously mentioned is given by Elices et al. [66]. As described before, in cohesive zone models, the fracture process is represented as a gradual process of separation between two material surfaces [67]. This process is similar to a softening process that occurs at the front of a crack tip. On the other hand,

Weertman [68] has modified the BCS model to include the effect of work hardening at the fatigue crack tip by relating the average stress in the plastic zone in front of the crack tip to the crack tip displacement. He assumed this relationship to be a power law with two parameters. In the Taira-Tanaka-Nakai model, the BCS model is applied to the case of slip bands emanating from a crack tip inside a grain; Taira et al. [56] recognized that, when a plastic tip reaches a grain boundary, the dislocations pile up against the grain boundary. Using Muskhelishvili's inversion formula [69], they solved a two-dimensional dislocation density equation with the plastic tip blocked by a grain boundary by assuming that, mathematically, dislocation density becomes infinite at a grain boundary. They refer to this as an unbounded solution; conversely, the original BCS model employs a bounded solution. Tanaka et al. [57] have extended the Taira-Tanaka-Nakai model by including the crack closure for stage II cracks and calculating the fatigue crack growth rates across stage I and stage II. Later, Navarro and De Los Rios (N-R) [58, 59, 60, 61] combined both the bounded and unbounded solutions into a general expression for the dislocation distribution. In addition, they applied a critical grain boundary strength parameter that a crack needs to overcome in order to propagate into the next grain. To examine the statistics of the short fatigue crack growth in textured FCC polycrystals, Wilkinson [70, 71] used the N-R model within the Monte Carlo framework.

In Chapter IV, we present a new method for the integration of a cohesive zone model (such as [18, 17]) within the BCS [55] and the Taira-Tanaka-Nakai [56] models to simulate microstructurally short fatigue crack growth through multiple grains. The BCS and Taira-Tanaka-Nakai models assume that the friction stress opposing the dislocation motion is the local yield stress of the material. Similarly, for a macroscopic crack, Dugdale's model assumes that the cohesive stress opposing the opening of a mode I crack tip is the yield stress of the material. However, molecular dynamics (MD) simulations have shown that the cohesive strength varies with the crack

opening displacement [72], and, in the shear mode, it is closely approximated by an exponential relationship [73]. In this chapter, we assume that the friction stress opposing the dislocation motion is a function of the crack displacement, as is shown by MD simulations. Incorporating this assumption in the BCS and Taira-Tanaka-Nakai models, we derive an expression for the bounded and unbounded solutions to the dislocation density distribution equations. These expressions are solved numerically to get the crack displacement and the crack tip stress field. This allows cohesive zone models (obtainable from a lower scale simulation, such as molecular dynamics) to be integrated into a dislocation theory-based model, for the first time, to predict microstructurally short fatigue crack growth. The details of this new formulation are shown for the two cases: the crack and the associated plastic zone inside a grain, and the crack and the associated plastic zone tip at the grain boundary. The main features of this new model are discussed along with an experimental comparison to the case of microstructurally short fatigue crack growth across two grains in a Ni-based CMSX-4 alloy.

In recent years, with carefully targeted experiments, the above mentioned mechanism-based models have produced good microstructurally short fatigue crack growth predictions in many structural alloys [59, 74, 75, 76]. However, these models utilize the assumption that the crack growth happens on a straight slip plane [55], and they don't take into account the effects of the three-dimensional (3D) crack-grain boundary interactions [77]. To overcome some of these limitations, Schick [78] has developed a boundary element method based on dislocation dipoles and has used this method to solve a two-dimensional (2D) microstructurally short fatigue crack growth problem. This boundary element method has been extended to simulate the crack transition from the stage I crack growth phase (in which the crack propagates along a single slip plane) to the stage II crack growth phase (in which there are more than one slip plane activated on the crack tip) [79, 80]. However, the 3D aspects of the crack plane, slip

plane, and grain boundary plane interactions have not been considered. Some of the aspects of these interactions, such as tilt and twist misorientations between the crack plane and the slip plane in the next grain calculated at a grain boundary, have been considered through phenomenological relationships between the various interactions [59, 81, 82].

In Chapter V, we present an improved phenomenological grain boundary model to simulate the effect of a grain boundary on microstructurally short fatigue crack growth along crystallographic planes. This model combines various geometrical features of the interaction between the crack plane and the grain boundary plane. The tilt and twist misorientations, calculated at a grain boundary between a crack plane and a favorable plane in the next grain, are incorporated into this model, as are the Schmid factor and a critical crack transmission stress.

In recent years, new experiments using innovative experimental techniques [83, 84] have improved our understanding of the 3D interactions between the crack plane, precipitates, and grain boundaries. Recently, Köster et al. [85] have used the distributed dislocation technique developed by Hills et al. [86] to extend the 2D microstructurally short fatigue crack growth models described above and in [78, 79] to 3D to model some of these 3D interactions. The distributed dislocation technique is based on the concept of equivalent eigenstrains [87] or transformation strains [88]. In general, the three-dimensional (3D) crack problem is converted to a set of two-dimensional (2D) hyper-singular integral equations and solved for either the crack displacements or the strains. In the past, this technique has been used to solve these hyper-singular integral equations for the following problems: two dissimilar semi-elliptical interacting cracks under tension and bending [89], a 3D crack terminating at bimaterial interface [90], the partial closure and frictional slip of a 3D crack [91], two interacting cracks in an elastic half-space [92], and a 3D crack with a constant yield plastic zone in front of the crack [93]. These 3D dislocation models have been used to investigate the effect of

crack depth on the interaction of a microstructurally short fatigue crack with a grain boundary [85]. Recently, these models have been used to investigate the effect of tilt and twist misorientations on microstructurally short fatigue crack growth rates at a grain boundary in a virtual microstructure [94]. Recent experiments involving microstructurally short cracks have included using scanning electron microscopy-based fractography to measure 3D microstructurally short fatigue crack growth evolution, X-ray computed tomography to provide high resolution 3D crack surface morphology, and X-ray diffraction microscopy to provide 3D grain geometry and orientations [77]. These experiments have expanded our understanding of the mechanisms surrounding microstructurally short fatigue crack growth. Using ultrasonic fatigue and scanning electron microscopy (UF-SEM) [95], Adams et al. [96] have performed experiments on a magnesium WE43 alloy to allow *in situ* observation of damage accumulation and fatigue crack growth on the microstructural scale. Fractographic investigation of the crack surfaces to examine micro-beach marks on the fracture surfaces has provided greater insights into crack initiation and microstructurally short fatigue crack growth in this alloy.

In Chapter VI, we use the distributed dislocation technique developed by Hills et al. [86] to investigate microstructurally short fatigue crack growth in a magnesium WE43 alloy using the experimental micro-beach marks provided by Adams et al. [97]. The micro-beach marks on the magnesium WE43 alloy's fracture surfaces are first converted into crack geometries and then approximated by a many-sided polygon with a triangular mesh. The resulting finite domain problem is solved for crack displacements and stress intensity factors. We use this method to model two cases of microstructurally short fatigue crack-grain boundary interactions in a magnesium WE43 alloy: the interaction of a crack front growing towards a grain boundary with the grain boundary and the interaction of a crack front spanning across multiple grains with the grain boundary it crosses.

Finally, in the last chapter we conclude with a summary of the key contributions of the dissertation and a list of areas for future research.

CHAPTER II

A Fracture Mechanics-Based Irreversible Cohesive Model

In this chapter, we present a linear elastic fracture mechanics (LEFM)-based two-parameter irreversible cohesive model for predicting fatigue crack growth rates within the long crack growth regime. The main feature of this cohesive model is the hysteresis between the reloading and unloading paths. This hysteresis represents the energy dissipation due to various physical phenomena. This irreversible cohesive zone model, which represents the crack tip mechanics, is combined with linear elastic fracture mechanics to predict fatigue crack growth rates in metal alloys. The advantages of this method compared to a finite element-based method are simplicity, fast calibration, and good predictive capability under ideal small-scale yielding conditions.

This chapter is divided into the following sections. Section 2.1 gives a brief overview of the fracture mechanics equations that are used to calibrate the cohesive model. Section 2.2 describes the modified two-parameter irreversible cohesive model for both the zero applied stress ratio and the positive applied stress ratio conditions. In Section 2.3, we describe the numerical scheme utilized to solve the Fredholm integral equations that arise from embedding a cohesive zone in front of the crack tip. Section 2.4 explains the rationale for the determination of the cohesive zone length and the fatigue crack growth rates. In Section 2.5, a sensitivity study is performed

to show the impact of the cohesive zone length on the fatigue crack growth rate. To test the accuracy of this LEFM-cohesive model, fatigue crack growth rate curves for aluminum 7075-T6 and steel 4340 alloys are compared with experimental results.

2.1 Overview of fracture mechanics

In this section, we give a brief overview of the two-dimensional center crack problem and solve it using the complex function potential method [69]. In the complex function potential method, stresses and displacements are represented in terms of analytic functions of complex variables. Then, the Westergaard approach [98] is used to convert this solution to that of the equivalent mode I problem.

The biharmonic equation $\nabla^4\Phi = 0$ is solved by expressing the Airy stress function Φ in terms of two functions ϕ and ψ as shown below:

$$2\Phi = Re[\bar{z}\phi(z) + \psi(z)] \tag{2.1.1}$$

The Airy stress function Φ is defined through

$$\sigma_{xx} = \frac{\partial\Phi^2}{\partial y^2},\ \sigma_{xy} = -\frac{\partial\Phi^2}{\partial x\partial y},\ \sigma_{yy} = \frac{\partial\Phi^2}{\partial x^2}$$

The two functions, ϕ and ψ, are analytic functions of $z = x + iy$, where $i = \sqrt{-1}$.

In the case of mode I fracture, if the external loads are symmetric with respect to the x-axis, then $\sigma_{xy} = 0$ along $y = 0$. Using this symmetry, the Westergaard approach [98] is used in Eq. (2.1.1) by setting $\psi'' = -z\phi''$. The resulting stresses are

$$\sigma_{xx} = Re\phi' - yIm\phi''$$

$$\sigma_{yy} = Re\phi' + yIm\phi''$$

$$\sigma_{xy} = -yRe\phi''$$

and the displacements are

$$2\mu u_x = \frac{\kappa - 1}{2} Re\phi - yIm\phi'$$
$$2\mu u_y = \frac{\kappa + 1}{2} Im\phi - yRe\phi' \tag{2.1.2}$$

where $\kappa = 3-4\nu$ for plane strain and $\kappa = \frac{3-\nu}{1+\nu}$ for plane stress, ν is the Poisson's ratio, ϕ'' is the second derivative with respect to z, ϕ' is the first derivative with respect to z, Re is the real part, and Im is the imaginary part. The general solution for ϕ' when a crack in an infinite plate is subjected to a traction $T(t)$ in the y-direction on the top surface and equal and opposite tractions on the bottom surface is

$$\phi' = \frac{1}{\pi\sqrt{z^2 - c^2}} \int_c^{-c} T(t) \frac{\sqrt{c^2 - t^2}}{z - t} dt \tag{2.1.3}$$

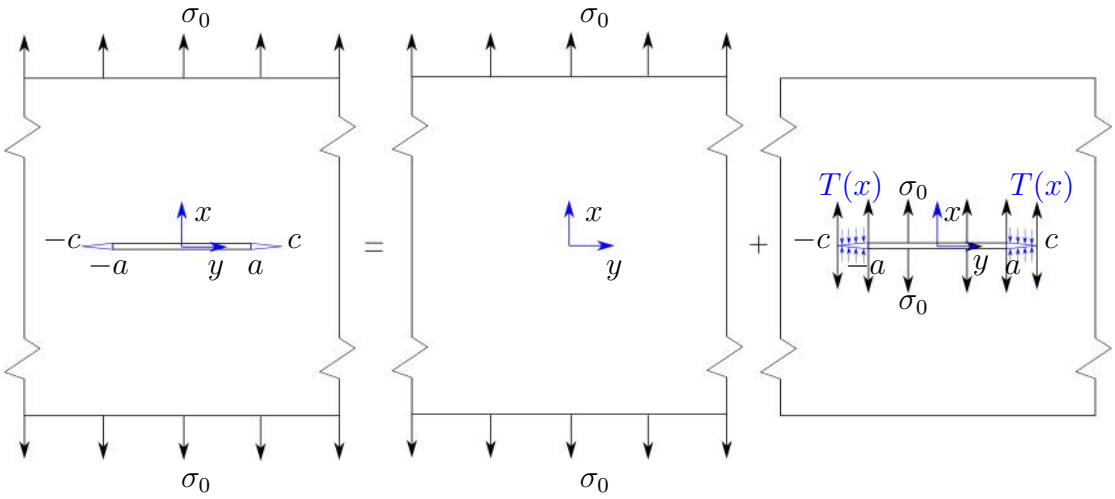

Figure 2.1: A finite crack in an infinite plate subjected to tensile loading is considered by superposing a uniform stress field with no crack and a constant pressure σ_0 acting on the crack faces ($-c \leqslant x \leqslant c$) and cohesive stresses $T(x)$ acting on the cohesive zone at the crack tip ($a \leqslant |x| \leqslant c$).

Now, consider an infinite plate containing a finite crack of length $2c$ (lying along y=0 as shown in Figure 2.1) with a cohesive zone on the crack tip of half length $c-a$ and a far field uniform stress $\sigma_{yy} = \sigma_0$, $\sigma_{xx} = 0$, and $\sigma_{xy} = 0$ applied in tension. This

problem can be solved by superposing two conditions: (1) a uniform stress field with no crack and (2) a constant pressure σ_0 acting on the crack faces ($-c \leqslant x \leqslant c$) and cohesive stresses $T(x)$ acting on the cohesive zone at the crack tip ($a \leqslant |x| \leqslant c$). As shown in Figure 2.1, for the infinite plate with no crack, a tensile stress $\sigma_{yy} = \sigma_0$ acts along $y = 0$, and, for the infinite plate with a crack and a cohesive zone, a compressive stress σ_0 is applied on the crack faces to make them traction free. For $-c < x < c$ and considering only the contribution from σ_0, Eq. (2.1.3) gives

$$\begin{aligned} \phi' &= \frac{\sigma_0 z}{\sqrt{z^2 - c^2}} - \sigma_0 \\ \phi &= \sigma_0 \sqrt{z^2 - c^2} - \sigma_0 z + \text{constant} \end{aligned} \tag{2.1.4}$$

Using Eqs. (2.1.2) and (2.1.4) and noting that $Re(\frac{\sigma x}{\sqrt{x^2-c^2}}) = 0$ along $-c \leqslant x \leqslant c$ and $y = 0$, the crack opening displacement $\delta_0(x)$ due to σ_0 is

$$\delta_0(x) = \sigma_0 c \frac{4}{E_1} \sqrt{1 - x^2/c^2} \tag{2.1.5}$$

where $E_1 = E$ for plane stress, $E_1 = \frac{E}{(1-\nu^2)}$ for plane strain, and E is the Young's modulus.

Similarly, the crack opening displacement due to the presence of the cohesive stresses $T(x)$ in the region $a \leqslant |x| \leqslant c$ and $y = 0$ can be obtained by integrating Eq. (2.1.3) and substituting the result into Eq. (2.1.2). The final equation becomes

$$\delta_c(x) = \frac{4}{\pi E_1} \int_a^c G(x, x') T(x') dx' \tag{2.1.6}$$

where

$$G(x, x') = \ln \left| \frac{\sqrt{1 - x^2/c^2} + \sqrt{1 - x'^2/c^2}}{\sqrt{1 - x^2/c^2} - \sqrt{1 - x'^2/c^2}} \right|$$

Eq. (2.1.6) represents the crack opening displacement due to the compressive stress that acts on the cohesive zone ($a \leqslant |x| \leqslant c$). Physically, this equation represents

the gradual formation of a surface at the crack tip. Thus, the total crack opening displacement due to the presence of a crack and the associated cohesive zone is given by

$$\delta(x) = \frac{4c\sigma_0}{E_1}\sqrt{1 - x^2/c^2} - \frac{4}{\pi E_1}\int_a^c G(x, x')T(x')dx', \ a \leqslant |x| \leqslant c \tag{2.1.7}$$

2.2 A two-parameter irreversible cohesive model

In the previous section, the expression for the crack opening displacement along the cohesive zone (Eq. (2.1.7)) was discussed. In this section, a phenomenological relationship between the crack surface traction and the crack opening displacement, called the traction-separation law [21], is described. The traction-separation law used in this chapter is a modification of the model proposed by Maiti and Geubelle [37]. As shown in Figure 2.2, the cohesive model (corresponding to an applied stress ratio of $R = \sigma_{min}/\sigma_{max} = 0$) exhibits a hysteresis between the reloading and unloading paths. This hysteresis represents the energy dissipation caused by the cycling loading process. In the first cycle, the cohesive traction T during loading follows the monotonic failure curve. The equation of this curve is

$$T = \sigma_f - h_n\delta \tag{2.2.1}$$

where h_n is the slope of the monotonic failure line and δ is the normal component of the displacement discontinuity on the crack face.

During unloading, the crack surfaces elastically unload; thus, there is no energy dissipation. Therefore, the equation for the slope of the unloading path is

$$k^1 = \frac{T^1}{\delta^1} \tag{2.2.2}$$

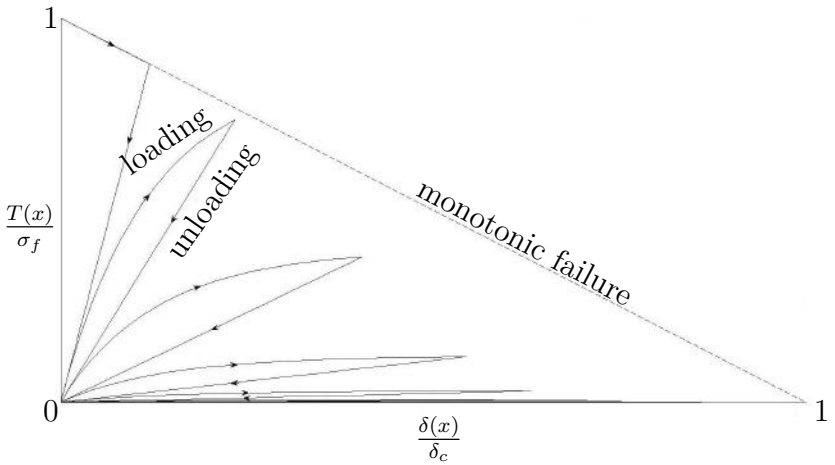

Figure 2.2: Subcritical vs. critical failure. σ_f and δ_c are the Mode I failure stress and critical crack opening displacement, respectively [99].

After the first cycle, the following reloading curves have progressively degrading cohesive tractions. The instantaneous slope h_n of this curve is

$$h_n = \frac{dT}{d\delta} = k^1 - \gamma_N T \tag{2.2.3}$$

where

$$\gamma_N = \frac{1}{\alpha} N^{-\beta},$$

k^1 is the slope of the first unloading path, and N denotes the number of cycles experienced by a material point since the onset of failure. In the above equation, a two-parameter power law relationship is used to model the rate of decay of the cohesive stiffness h_n. α and β are the cohesive parameters that degrade the cohesive strength during reloading. The cohesive parameter α has dimensions of length, while β denotes the history dependence of the failure process. Both of these parameters account for the reloading-unloading hysteresis. As discussed in the introduction section, this hysteresis may, in the phenomenological sense, account for the dissipative mechanism arising either from reverse yielding upon unloading [100] or as a result of the repeated rubbing of asperities.

2.2.1 Irreversible cohesive model with the condition $R = 0$

In this subsection, we show the cohesive model equations for the zero applied stress ratio condition. The cohesive traction for reloading in the Nth cycle is derived by integrating Eq. (2.2.3). The result is

$$T^N_{max} = \frac{k^{N-1}}{\gamma_N}\left(1 - e^{-\gamma_N \delta^N_{max}}\right) \tag{2.2.4}$$

where $k^{N-1} = \frac{T^{N-1}_{max}}{\delta^{N-1}_{max}}$. In Figure 2.3, this equation is plotted along with Eq. (2.2.1).

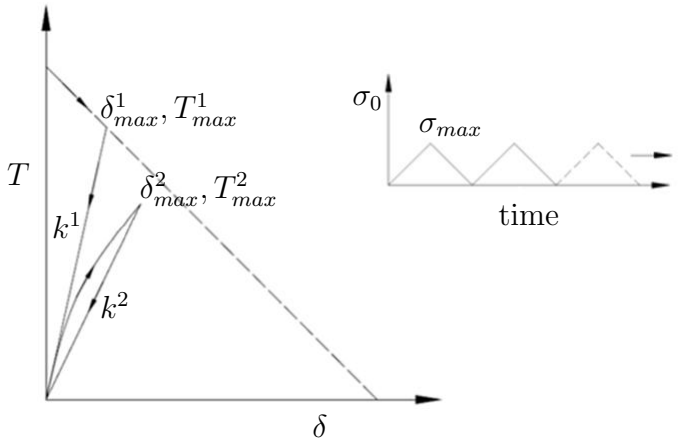

Figure 2.3: Traction-separation curve for the condition $R = 0$

The crack opening displacement for the loading in the first cycle is calculated by putting Eq. (2.2.1) into Eq. (2.1.7). The resulting equation is

$$\delta^1_{max}(x) = \frac{4}{\pi E_1}\left(\sigma_0 \pi c\sqrt{1 - x^2/c^2} - \sigma_f \int_a^c G(x, x')dx'\right) + \frac{4h_n}{\pi E_1}\int_a^c G(x, x')\delta^1_{max}(x')dx',$$
$$a \leqslant |x| \leqslant c \tag{2.2.5}$$

Eq. (2.2.5) is a linear Fredholm integral equation of the second kind with a weakly singular kernel. Similarly, the crack opening displacement for the loading in the Nth

cycle is calculated by putting Eq. (2.2.4) into Eq. (2.1.7). The resulting equation is

$$\begin{aligned}\delta^N_{max}(x) =& \frac{4c\sigma_0}{E_1}\sqrt{1-x^2/c^2} - \frac{4k^{N-1}}{\pi E_1 \gamma_N}\int_a^c G(x,x')\big(1-e^{-\gamma_N \delta^N_{max}(x')}\big)dx', \\ & a \leqslant |x| \leqslant c\end{aligned} \tag{2.2.6}$$

Eq. (2.2.6) is a nonlinear Fredholm integral equation of the second kind with a weakly singular kernel. These two equations (Eqs. (2.2.5) and (2.2.6)) are numerically solved using the Newton-Raphson scheme with a piecewise polynomial collocation method [101]. The discretization and solution procedure is described in Section 2.3.

2.2.2 Irreversible cohesive model with the condition $R > 0$

The cohesive traction equation for the loading in the first cycle is given by Eq. (2.2.1). For the reloading in the Nth cycle, the maximum cohesive traction T^N_{max} corresponding to the maximum applied stress σ_{max} is

$$T^N_{max} = T^{N-1}_{min} + \frac{k^{N-1}}{\gamma_N}\Big(1-e^{-\gamma_N\left(\delta^N_{max}-\delta^{N-1}_{min}\right)}\Big) \tag{2.2.7}$$

As discussed in the previous section, the unloading path of the cohesive model is assumed to be elastic; therefore, no material degradation occurs during unloading. Thus, the minimum cohesive traction T_{min} corresponding to the minimum applied stress σ_{min} can be written as

$$T^{N-1}_{min} = k^{N-1}\delta^{N-1}_{min} \tag{2.2.8}$$

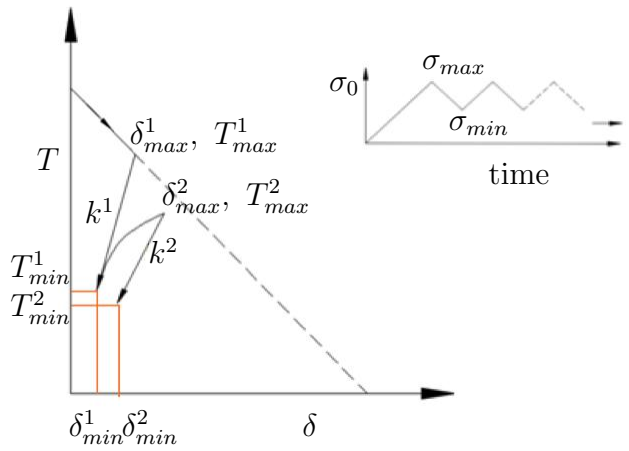

Figure 2.4: Traction-separation curve for the condition $R > 0$

In Figure 2.4, Eqs. (2.2.7) and (2.2.8) are plotted for a positive R. The crack opening displacement equation for the loading in the first cycle is given by Eq. (2.2.5). For the loading in the Nth cycle, the crack opening displacements δ_{max} and δ_{min} are obtained by putting Eqs. (2.2.7) and (2.2.8), respectively, into Eq. (2.1.7). The resulting equations are

$$\delta^{N-1}_{min}(x) = \frac{4c\sigma_0}{E_1}\sqrt{1-x^2/c^2} - \frac{4k^{N-1}}{\pi E_1}\int_a^c G(x,x')\delta^{N-1}_{min}(x')dx', a \leqslant |x| \leqslant c \qquad (2.2.9)$$

and

$$\begin{aligned}\delta^N_{max}(x) =& \frac{4}{\pi E_1}\left(\sigma_0\pi c\sqrt{1-x^2/c^2} - \left(T^{N-1}_{min} + \frac{k^{N-1}}{\gamma_N}\right)\int_a^c G(x,x')dx'\right) \\ &+ \frac{4k^{N-1}}{\pi E_1\gamma_N}\int_a^c G(x,x')e^{-\gamma_N\left(\delta^N_{max}(x')-\delta^{N-1}_{min}(x')\right)}dx', \\ & a \leqslant |x| \leqslant c\end{aligned} \qquad (2.2.10)$$

Again, these two equations (Eqs. (2.2.9) and (2.2.10)) are Fredholm integral equations of the second kind with weakly singular kernels. The solution procedure for solving these equations is shown in Section 2.3.

2.3 Numerical scheme for solving a Fredholm integral equation of the second kind with a weakly singular kernel

The Fredholm integral equations (Eqs. (2.2.5), (2.2.6), (2.2.9), and (2.2.10)) are discretized using a piecewise polynomial collocation method [101]. The discretization procedure is briefly described in this section.

In these equations, the kernel $G(x, x')$ is singular when $x = x'$, $x = c$, or $x' = c$. As discussed in [101], we make use of polynomial splines with a graded mesh and split the domain ($a < |x| < c$) in half. The partition points for the first half are $a = x_0 < x_1 < ... < x_n = \frac{c+a}{2}$, while the points for the second half of the domain $(x_{n+1}, ..., x_{2n})$ are obtained by reflecting the partition points of the first half about $x_n = \frac{c+a}{2}$. The graded mesh nodes for the first half of the domain are calculated by

$$x_j = a + \left(\frac{j}{n}\right)^r \frac{c-a}{2},\ j = 0, 1, 2, ..., n \tag{2.3.1}$$

where r determines the distribution of the grid points. For $r = 1$, the grid points are evenly spaced, and, for $r > 1$, the grid points are close to zero in the domain $(0,\ (c+a)/2)$. The points for the second half of the domain are calculated by

$$x_{j+n} = c + a - x_{n-j},\ j = 1, 2, ..., n \tag{2.3.2}$$

For every subinterval $[x_j,\ x_{j+1}]$ for $j = 1, 2, ..., 2n$, we use two collocation points. These points are given by

$$\xi_{ji} = x_j + \frac{\eta_i + 1}{2}\big(x_{j+1} - x_j\big),\ \text{where } \eta_1 = \frac{1}{\sqrt{3}},\ \eta_2 = -\frac{1}{\sqrt{3}} \tag{2.3.3}$$

The continuous function $\delta(x)$ that represents the crack opening displacement is replaced by an interpolation function that is independently defined on each subinterval

$[x_j,\ x_{j+1}]$ for $j = 1, 2, ..., 2n$. This interpolation function may be discontinuous at the interior grid points $x = x_j$ for $j = 1, 2, ..., 2n-1$. Thus, within the interval $[x_j,\ x_{j+1}]$, for $j = 1, 2, ..., 2n$, the function is

$$\delta(x) = s_{j1}\frac{\xi_{j2} - x}{\xi_{j2} - \xi_{j1}} + s_{j2}\frac{x - \xi_{j1}}{\xi_{j2} - \xi_{j1}},\ x_{j-1} \leqslant x \leqslant x_j \tag{2.3.4}$$

Eq. (2.3.4) is put into Eqs. (2.2.5), (2.2.6), (2.2.9), and (2.2.10), and the resulting equations are solved using the Newton-Raphson scheme.

2.4 Determination of the Cohesive zone length and fatigue crack growth rates

For monotonic failure, the cohesive zone length $c-a$ is calculated from the assumption of zero energy dissipation at the cohesive tip [26, 102]. Using this assumption, the applied stress intensity factor at the cohesive tip K_0 is equal to that of the cohesive traction K_{coh}. This is written as

$$K_{tip} = K_0 - K_{coh} = 0 \tag{2.4.1}$$

where K_{tip} is the net stress intensity factor at the cohesive tip and $K_0 = \sigma_0\sqrt{\pi c}$. Eq. (2.4.1) represents a single nonlinear damage mechanism in the cohesive zone. In a single nonlinear damage mechanism, the crack growth process is the same as the crack opening process. This is true for the original Dugdale's [17] cohesive zone model of yielding in metals. In this original cohesive model, the assumption was that the crack growth happens when the cohesive tip yields, and the same yield stress was used for the cohesive traction. However, in many materials, the stress required for crack growth at the cohesive tip and the stress in the cohesive zone are different. Near the cohesive tip, the crack growth process consists of breaking strong material

elements at small strains, while smaller tractions are needed for the crack to open within the cohesive zone immediately behind the cohesive tip. Thus, in Eq. (2.4.1), $K_{tip} \neq 0$, and the equation becomes

$$K_{tip} = K_0 - K_{coh} = K_c \tag{2.4.2}$$

where K_c is the critical stress intensity factor required for the crack to grow. However, in fatigue failure, Eq. (2.4.2) does not hold, as failure can happen at stresses that are lower than the monotonic failure stress.

To determine the length of the cohesive zone for fatigue crack growth, we make use of the elementary material block of size ρ proposed by Noroozi et al. [103]. Noroozi et al. calculated the value of ρ from the Creager-Paris solution. We assume that the cohesive zone spreads across the elementary material block; therefore, $c - a = \rho$. We follow the approach outlined by Noroozi et al. to calculate the average fatigue crack growth rates. Thus, the relationship is

$$\frac{da}{dN} = \frac{\rho}{N^*} \tag{2.4.3}$$

The only unknown parameter in the above equation is N^*. This parameter is the number of cycles to failure of the elementary material block of size ρ. $N*$ is calculated by solving Eqs. (2.2.5) and (2.2.6) for $R = 0$ and Eqs. (2.2.9) and (2.2.10) for $R > 0$. These calculations are repeated for each cycle until the cohesive traction $T(x)$ at the crack tip $x = a$ reaches a zero value, at which $N^* = N$. For each cycle, the range of the applied stress intensity factor ΔK required to calculate the Paris curve is calculated from the expressions provided in Tada et al. [104].

2.5 Results and discussion

In this section, we show the capability of our LEFM-based irreversible cohesive model to predict fatigue crack growth rates in metal alloys. Towards this end, we first perform a sensitivity study of the impact of the cohesive zone length on the fatigue crack growth rates. Next, we use the model to predict fatigue crack growth rates for two metal alloys by calibrating the model using experiments with $R = 0$ and predicting fatigue crack growth rates for different applied stress ratios. The two metal alloys are aluminum 7075-T6 [105] and steel 4340 [106] alloys. For all the results presented in this section, the numerical parameters used in the model are shown in Table 2.1.

Variable	Value
n	16
r	3.2

Table 2.1: Numerical parameters

2.5.1 A sensitivity study of the cohesive zone length

A sensitivity study is carried out to show the impact of the cohesive zone length on the average fatigue crack growth rates. In this study, the numerator ρ in Eq. (2.4.3) is assumed to be constant. The denominator is nonlinearly dependent on the cohesive zone length through Eqs. (2.2.5) and (2.2.6) for $R = 0$ and Eqs. (2.2.9) and (2.2.10) for $R > 0$. Thus, the main objective of this study is to quantify the effect of this nonlinear dependence. For this analysis, we fixed all the parameters and varied only the cohesive zone length as some fraction of ρ. The parameters used in this analysis are shown in Table 2.2.

Variable	Value	Unit
E	71	GPa
ν	0.32	
σ_f	780	MPa
G_{IC}	9.80	N/m
ρ	4.03×10^{-6}	m
α	0.7	μm
β	0.7	

Table 2.2: Parameters used in sensitivity study

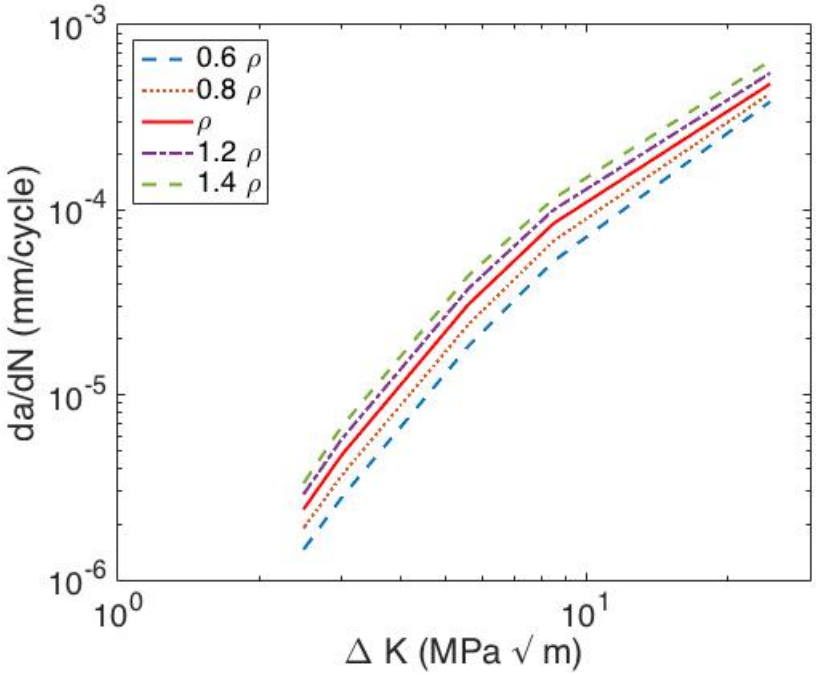

Figure 2.5: Impact of the variation of the cohesive zone length on fatigue crack growth rates

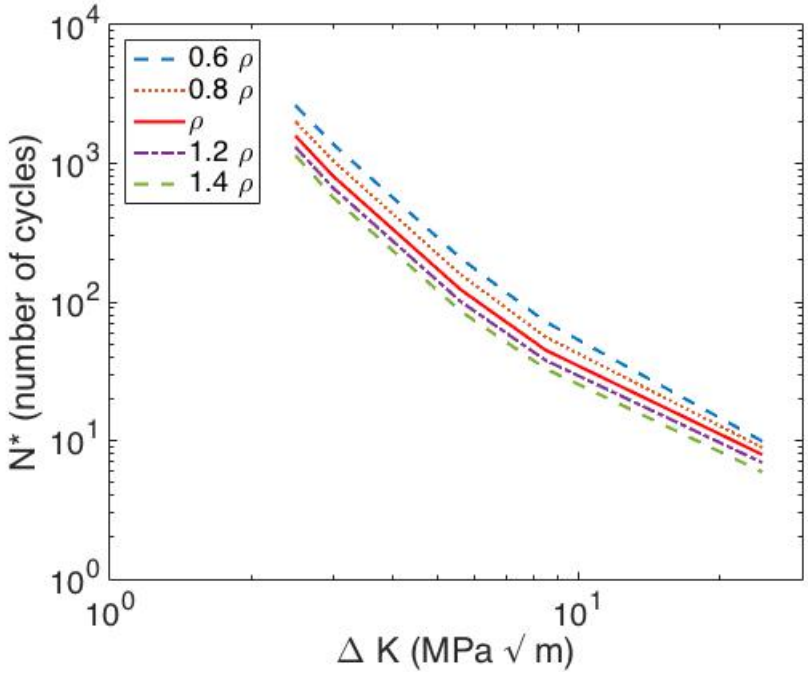

Figure 2.6: Impact of the variation of the cohesive zone length on the number of cycles to failure

In Figure 2.5, the impact of the variation of the cohesive zone length on the fatigue crack growth rates is shown. We have also plotted the impact of the variation of the cohesive zone length on the number of cycles to failure (Figure 2.6). For the same range of applied stress intensity factors, increasing the cohesive zone length reduces the number of cycles to failure and increases the fatigue crack growth rates. This is consistent with literature, such as [75], in which it is shown that the length of the cyclic cohesive zone is smaller than the length of the monotonic cohesive zone. In addition, at higher values of the range of applied stress intensity factors, the assumption of a constant cohesive zone length does not hold. Thus, to maintain the same slope of the Paris curve (Figure 2.5), the cohesive zone length should increase with the range of the applied stress intensity factors. However, in this chapter, we have assumed that the length of the cyclic cohesive zone is constant. This assumption is valid for a small range of applied stress intensity factors. However, care must be taken in using the correct value of the cohesive zone length.

2.5.2 Validation of the LEFM-based cohesive model using experimental fatigue crack growth rates

In this part, we show the validation of the LEFM-based cohesive model using experimental fatigue crack growth rates in aluminum 7075-T6 (Al 7075-T6) [105] and steel 4340 (St 4340) [106]. The materials properties for Al 7075-T6 are given in Table 2.3.

Variable	Value	Unit	Reference
E	71	GPa	[105]
ν	0.32		[105]
σ_f	780	MPa	[103]
G_{IC}	9.80	N/m	[107]
ρ	4.03×10^{-6}	m	[103]

Table 2.3: Material properties of Al 7075-T6 alloy

The only unknown parameters in Eqs. (2.2.5), (2.2.6), and (2.4.3) are α and β. These two parameters control the slope m and the intercept C of the Paris curve [37, 99]. Increasing the value of α reduces the slope and increases the intercept of the Paris curve, while increasing the value of β increases the slope and reduces the intercept. Thus, to calibrate these two parameters, numerous simulations were performed with different values of cohesive parameters α and β.

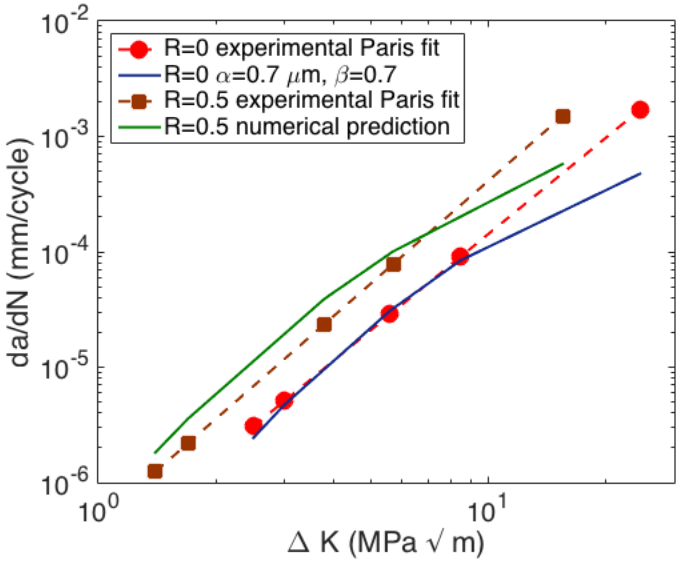

Figure 2.7: Calibration of cohesive parameters using Paris fit of Al 7075-T6 with $R = 0$ and model prediction for $R = 0.5$

In Figure 2.7, using Eqs. (2.2.5) and (2.2.6), the cohesive model parameters are calibrated with a Paris fit of Al 7075-T6 with $R = 0$. Paris fits of Al 7075-T6 with $R = 0$ and 0.5 are used in the above figure due to a large scatter within the experimental data. The calibrated parameters are $\alpha = 0.7\ \mu m$, $\beta = 0.7$. These calibrated cohesive parameters are then used in Eqs. (2.2.5), (2.2.9), and (2.2.10) to predict the Paris curve with $R = 0.5$. The numerical fatigue crack growth rates shown in Figure 2.7 match quite well with the Paris fit of the experimental data.

Variable	Value	Unit	Reference
E	200	GPa	[106]
ν	0.30		[106]
σ_f	1897	MPa	[103]
G_{IC}	81.72	N/m	[106]
ρ	1.1×10^{-5}	m	[103]

Table 2.4: Material properties of St 4340 alloy

A similar procedure is employed to predict fatigue crack growth rates within St 4340. The material properties for this alloy are listed in Table 2.4.

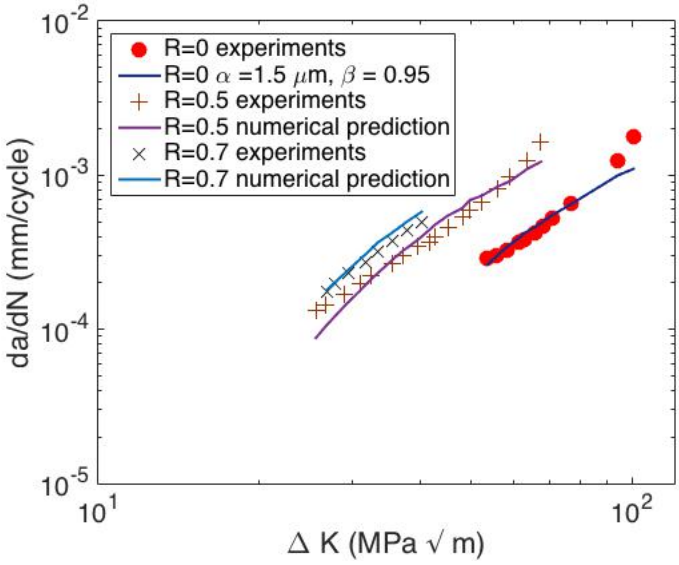

Figure 2.8: Calibration of cohesive parameters using fatigue crack growth rates within St 4340 with $R = 0$ and model predictions for $R = 0.5,\ 0.7$.

In Figure 2.8, the cohesive parameters in Eqs. (2.2.5) and (2.2.6) are calibrated using experimental fatigue crack growth rates with $R = 0$. The calibrated parameters are $\alpha = 1.5\ \mu m,\ \beta = 0.95$. Also plotted in the same figure are the experimental and numerical fatigue crack growth rates for $R = 0.5$ and $R = 0.7$. The model predictions correlate well with experimental fatigue crack growth rates for $R = 0.5$ and $R = 0.7$. Thus, the LEFM-based cohesive model is well suited to predict fatigue crack growth rates within the long crack growth regime.

2.6 Conclusion

This chapter outlines the main features of a new linear elastic fracture mechanics-based irreversible cohesive model. The irreversible cohesive model is combined with fracture mechanics to predict high cycle fatigue crack growth rates within the long crack growth regime. The key contribution of this chapter is the ability to quickly

calibrate the cohesive parameters based on one Paris curve as well as to predict high cycle fatigue crack growth rates for various stress ratios. To test the accuracy of this new formulation, we first perform a sensitivity study of the cohesive zone length. The new formulation is then used to predict high cycle fatigue crack growth rates in two metal alloys. The advantage of this new formulation over finite element-based formulations is that, using this method, the cohesive parameters are easily calibrated to experimental high cycle fatigue crack growth rates. The numerical results show good correlation with aluminum 7075-T6 and steel 4340 experimental fatigue crack growth rates.

CHAPTER III

Modeling Fatigue Failure using the Variational Multiscale Method

[1]In this chapter, we study fatigue failure using the variational multiscale method (VMM). In the VMM, displacement jumps are represented using finite elements with specially constructed discontinuous shape functions. These elements are progressively added along the crack path during fatigue failure. The stiffness of these elements changes non–linearly in response to the accumulation of damage during cyclic loading. The evolution law for stiffness is represented as a function of traction and the number of loading cycles since the initial onset of failure. Numerical examples illustrate the use of this new methodology for modeling macroscopic crack growth under mode I loading as well as microscopic crack growth under mixed mode loading within the elastic regime. We find that the discontinuous elements can consistently predict the mode I stress intensity factor (SIF) and the microstructurally short crack growth paths, and that the computed Paris law for steady crack growth is controlled primarily by two parameters in the decohesion law.

The objectives of this chapter are: (1) to successfully demonstrate the coupling of the fatigue cohesive model with the variational multiscale method, (2) to correctly

[1]Reproduced from Shardul Panwar, Shang Sun, and Veera Sundararaghavan. Modeling fatigue failure using the variational multiscale method. *Engineering Fracture Mechanics*, 162:290–308, 2016

predict the macro-scale mode I stress intensity factor, (3) to correlate the experimental microstructurally short crack path with the VMM crack path, (4) to introduce an approach for calibrating the fatigue cohesive law parameters from the macro experiments, and (5) to show that different steady-state crack growth rates (or Paris laws) can be simulated by different cohesive parameters that control the loading stiffness of the fatigue CZM.

This chapter is divided into three sections. Section 3.1 gives a brief description of the Variational Multiscale Method. Section 3.2 describes the cohesive model used for modeling fatigue failure. In Section 3.3, we present our numerical results for fatigue failure using different representative two-dimensional problems.

3.1 The Variational Multi-Scale Method (VMM)

The presence of cracks in a continuum domain necessitates a discontinuous representation of the displacement field. A numerical treatment of such discontinuities and the resultant singular strain field was done in the work of Temam and Strang [108], which was on the space BD(Ω) (of functions of bounded deformation). This idea was later used to develop a numerical framework for the problem of strong discontinuities due to strain localization by Simo et al. [109], Simo and Oliver [110], and Armero and Garikipati [38]. Later, this approach was adopted by Garikipati [47] to embed micro-mechanical surface laws into a macroscopic continuum formulation in a multiscale setting. The mathematical model of this variational multiscale method is briefly described in Section 3.1.1.

3.1.1 A mathematical model of the Variational Multiscale Method

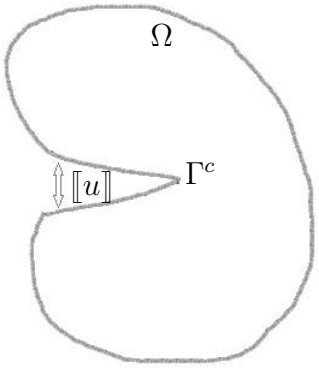

Figure 3.1: 2Dimensional representation of a crack opening$[\![u]\!]$ and the crack surface Γ^c

The crack surface (Γ_c) in a continuous domain (Ω) is shown in Figure 3.1. The standard weak form of the balance of linear momentum over the domain (Ω) is given by

$$\int_\Omega \boldsymbol{\nabla}^s \boldsymbol{w} : \boldsymbol{\sigma}\, dV = \int_\Omega \boldsymbol{w} \cdot \boldsymbol{f}\, dV + \int_{\partial\Omega_t} \boldsymbol{w} \cdot \boldsymbol{T}\, dS \tag{3.1.1}$$

where $\boldsymbol{\sigma}$ is the stress, $\boldsymbol{w}$ is an admissible displacement variation, $\boldsymbol{\nabla}^s \boldsymbol{w}$ is the symmetric gradient of the variation, $\boldsymbol{T}$ is the external traction and $\boldsymbol{f}$ is the body force. The displacement fields ($\boldsymbol{u}$ and variation $\boldsymbol{w}$) can be decomposed into continuous coarse-scale ($\bar{\boldsymbol{u}}, \bar{\boldsymbol{w}}$) and discontinuous fine-scale ($\boldsymbol{u\prime}, \boldsymbol{w\prime}$) components. Such a decomposition is possible because of the requirement that the fine-scale fields $\boldsymbol{u\prime}$ and $\boldsymbol{w\prime}$ must vanish outside the fine-scale subdomain Ω'. In crack propagation problems, the fine-scale field ($\boldsymbol{u\prime}$) represents the discontinuity.

$$\boldsymbol{u} = \bar{\boldsymbol{u}} + \boldsymbol{u\prime} \tag{3.1.2}$$

$$\boldsymbol{w} = \bar{\boldsymbol{w}} + \boldsymbol{w\prime} \tag{3.1.3}$$

$$\bar{\boldsymbol{u}} \in \bar{\boldsymbol{S}} = \{\boldsymbol{v} | \boldsymbol{v} = \boldsymbol{g}\ \boldsymbol{on}\ \partial\Omega_{\boldsymbol{u}}\}$$

$$\bar{\boldsymbol{w}} \in \bar{\boldsymbol{\nu}} = \{\boldsymbol{v} | \boldsymbol{v} = \boldsymbol{0}\ \boldsymbol{on}\ \partial\Omega_{\boldsymbol{u}}\}$$

$$\boldsymbol{u\prime} \in \boldsymbol{S\prime} = \{\boldsymbol{v} | \boldsymbol{v} = \boldsymbol{0}\ \boldsymbol{on}\ \Omega \backslash \boldsymbol{int}(\Omega\prime)\}$$

$$\boldsymbol{w\prime} \in \boldsymbol{\nu\prime} = \{\boldsymbol{v} | \boldsymbol{v} = \boldsymbol{0}\ \boldsymbol{on}\ \Omega \backslash \boldsymbol{int}(\Omega\prime)\}$$

where $\boldsymbol{S} \subset \boldsymbol{BD}(\Omega)$, $\boldsymbol{\nu} \subset \boldsymbol{H^1}(\Omega)$, $\boldsymbol{S} = \bar{\boldsymbol{S}} \oplus \boldsymbol{S\prime}$,

and $\boldsymbol{\nu} = \bar{\boldsymbol{\nu}} \oplus \boldsymbol{\nu\prime}$. $\bar{\boldsymbol{\nu}}$ and $\boldsymbol{\nu\prime}$ are chosen to be linearly independent. More concisely, the choice of space $\bar{\boldsymbol{S}}$ at the elemental level can be represented using linear polynomials, while space $\boldsymbol{S\prime}$ contains non-nodal supported functions (e.g. discontinuities) that are independent from $\bar{\boldsymbol{S}}$.

Using this additive decomposition, the weak form (Eq. (3.1.1)) can be separated into two equations, one involving only the coarse-scale variation $\bar{\boldsymbol{w}}$, and another involving only the fine-scale variation $\boldsymbol{w\prime}$.

$$\int_\Omega \boldsymbol{\nabla^s \bar{w}} : \boldsymbol{\sigma}\, dV = \int_\Omega \bar{\boldsymbol{w}} \cdot \boldsymbol{f}\, dV + \int_{\Gamma_h} \bar{\boldsymbol{w}} \cdot \boldsymbol{T}\, dS \tag{3.1.4}$$

$$\int_\Omega \boldsymbol{\nabla^s w\prime} : \boldsymbol{\sigma}\, dV = \int_\Omega \boldsymbol{w\prime} \cdot \boldsymbol{f}\, dV + \int_{\Gamma_h} \boldsymbol{w\prime} \cdot \boldsymbol{T}\, dS \tag{3.1.5}$$

Eq. (3.1.5) can be simplified by using integration by parts and variational arguments to [47]:

$$\int_{\Gamma^c} \boldsymbol{w\prime}\, \boldsymbol{\sigma} \cdot \boldsymbol{n}\, dS = \int_{\Gamma^c} \boldsymbol{w\prime} \cdot \boldsymbol{T^c}\, dS \tag{3.1.6}$$

where $\boldsymbol{T^c}$ is the external traction on the crack faces.

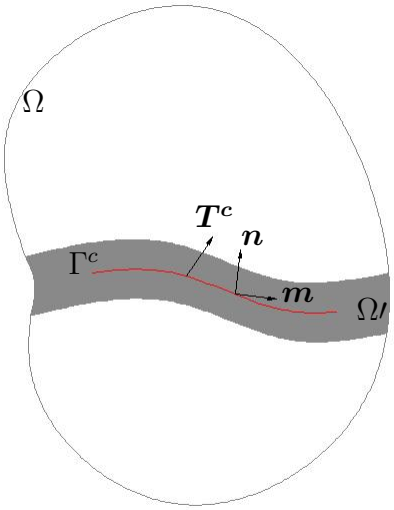

Figure 3.2: Microstructural domain $\Omega\prime$ and crack surface Γ^c, along with crack directions normal $\boldsymbol{n}$ and tangent $\boldsymbol{m}$

3.1.2 The Micro-Mechanical Surface Law

The micromechanics of crack growth (Figure 3.2) can be explained by a traction-separation law. This traction-separation law is inserted into the continuum formulation through Eq. (3.1.6). The traction $\boldsymbol{T^c}$ is decomposed into two components (for 2D problems), one normal to the crack face (T_n^c) and another tangent to the crack face (T_m^c).

$$\boldsymbol{T^c} = T_n^c\,\boldsymbol{n} + T_m^c\,\boldsymbol{m} \tag{3.1.7}$$

The fine scale-field $\boldsymbol{u\prime}$, which is composed of a displacement discontinuity $[\![\boldsymbol{u}]\!]$, can be similarly decomposed into its components $[\![u_n]\!]$ (opening) and $[\![u_m]\!]$ (shear) along the $\boldsymbol{n}$ and $\boldsymbol{m}$ directions respectively.

$$[\![\boldsymbol{u}]\!] = [\![u_n]\!]\,\boldsymbol{n} + [\![u_m]\!]\,\boldsymbol{m} \tag{3.1.8}$$

Using the above two equations (Eqs. (3.1.7) and (3.1.8)), the micro-mechanical cohesive law (discussed in Section 4) can be utilized by specifying the relationship between

traction components and discontinuous displacement components in both the normal and tangential directions. For the case of monotonic loading, a simple surface traction law is used, given by [111]:

$$T_n^c = T_{n0}^c - \mathcal{H}_n[\![u_n]\!], T_m^c = T_{m0}^c - \mathcal{H}_m[\![u_m]\!] \tag{3.1.9}$$

where T_{n0}^c and $\mathcal{H}_n$ are the mode I critical opening traction and mode I softening modulus, respectively, and T_{m0}^c and $\mathcal{H}_m$ are the mode II critical opening traction and mode II softening modulus, respectively. In Section 3.2, we modify the surface traction law to account for cyclic irreversibility.

3.1.3 Finite-Dimensional Formulation (2Dimensional)

In a finite-dimensional setting, the domain Ω can be divided into a number of connected non-overlapping elements such that $\Omega = \cup_1^{\boldsymbol{nel}} \Omega_e^h$, where $\boldsymbol{nel}$ represents the number of elements in the finite domain. The fine-scale displacement $\boldsymbol{u\prime}$ can be written in terms of local interpolation functions as:

$$\boldsymbol{u\prime_e} = \boldsymbol{M_{T^c}}\,[\![\boldsymbol{u}]\!]_{\boldsymbol{e}} \tag{3.1.10}$$

where $[\![\boldsymbol{u}]\!]_{\boldsymbol{e}}$ is the elemental value of the fine-scale displacement discontinuity. $\boldsymbol{M_{T^c}}$ is a multiscale shape function given by

$$\boldsymbol{M_{T^c}} = \boldsymbol{N} - \boldsymbol{H_{T^c}} \tag{3.1.11}$$

where $\boldsymbol{N}$ is the usual linear shape function for triangular elements, and $\boldsymbol{H_{T^c}}$ is the Heaviside function, which is used to introduce a discontinuity within the sub domain Γ_c. This construction ensures that $\boldsymbol{M_{T^c}} = \boldsymbol{0}$ on $\Omega \backslash int(\Omega\prime)$. The construction of this multiscale shape function $\boldsymbol{M_{T^c}}$ in two-dimensions is shown in Figure 3.3. In the weak

form, $\boldsymbol{M_{T^c}}$ comes into the system of equation as $\boldsymbol{\nabla M_{T^c}}$ through the expression for $\boldsymbol{\nabla u\prime}$.

$$\boldsymbol{\nabla u\prime} = \boldsymbol{\nabla M_{T^c}} [\![\boldsymbol{u}]\!] \tag{3.1.12}$$

where

$$[\![\boldsymbol{u}]\!] = \begin{bmatrix} [\![u]\!]_x \\ \\ [\![u]\!]_y \end{bmatrix}, \quad \nabla \boldsymbol{M_{T^c}} = \frac{1}{h^i} \boldsymbol{G} - \delta_{\Gamma^c} \boldsymbol{H},$$

$$\boldsymbol{G} = \begin{bmatrix} n_x^i & 0 \\ \\ 0 & n_y^i \\ \\ n_y^i & n_x^i \end{bmatrix}, \; and \; \boldsymbol{H} = \begin{bmatrix} n_x & 0 \\ \\ 0 & n_y \\ \\ n_y & n_x \end{bmatrix}$$

$\boldsymbol{G}$ and $\boldsymbol{H}$ are the matrix representations of a crack element's out-normal and a crack face's normal directions, respectively. h_i is the element length.

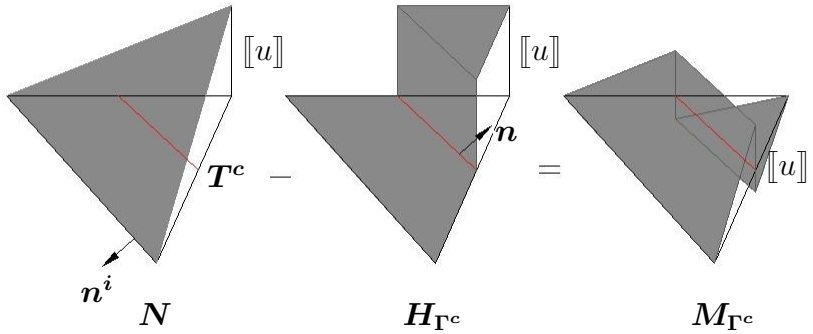

Figure 3.3: Construction of discontinuous multiscale shape function in 2D. n^i is the element out-normal and n is the normal direction of the crack face.

The expressions for strain and stress are given by [48],

$$\boldsymbol{\varepsilon} = \boldsymbol{Bd} + \left(\boldsymbol{G} - \boldsymbol{\delta_{T^c} H}\right) [\![\boldsymbol{u}]\!] \tag{3.1.13}$$

$$\boldsymbol{\sigma} = \mathbb{C} : \Big(\boldsymbol{Bd} + \boldsymbol{G} [\![\boldsymbol{u}]\!]\Big) \tag{3.1.14}$$

where $\boldsymbol{B}$ is the standard matrix form of the shape function gradient, $\boldsymbol{d}$ is the nodal value of the coarse-scale displacement, and $\mathbb{C}$ is the elastic stiffness matrix. Substituting these expressions into the weak form equations (Eqs. (3.1.4) and (3.1.6)), the resulting coarse-scale and fine-scale equations are respectively given by

$$\int_{\Omega} \boldsymbol{B}^T \mathbb{C} : (\boldsymbol{B}\boldsymbol{d} + \boldsymbol{G}[\![\boldsymbol{u}]\!])\, dV = \int_{\Omega} \boldsymbol{N} f\, dV + \int_{\Gamma_h} \boldsymbol{N} T\, dS \tag{3.1.15}$$

$$\boldsymbol{H}^T \mathbb{C} : (\boldsymbol{B}\boldsymbol{d} + \boldsymbol{G}[\![\boldsymbol{u}]\!]) = \boldsymbol{T}^{\boldsymbol{c}} \tag{3.1.16}$$

The resulting system of equation is solved using an iterative procedure [48] resulting in a coarse-scale residual ($\bar{\boldsymbol{r}}$) and a fine-scale residual ($\boldsymbol{r'}$).

$$\bar{\boldsymbol{r}} = \int_{\Omega} \boldsymbol{B}^T \mathbb{C} : (\boldsymbol{B}\boldsymbol{d} + \boldsymbol{G}[\![\boldsymbol{u}]\!])\, dV - \int_{\Omega} \boldsymbol{N} f\, dV - \int_{\Gamma_h} \boldsymbol{N} T\, dS \tag{3.1.17}$$

$$\boldsymbol{r'} = \boldsymbol{H}^T \mathbb{C} : (\boldsymbol{B}\boldsymbol{d} + \boldsymbol{G}[\![\boldsymbol{u}]\!]) - \boldsymbol{T}^{\boldsymbol{c}} \tag{3.1.18}$$

Linearization of the residual equations about $\boldsymbol{d}$ and $[\![\boldsymbol{u}]\!]$ gives the following system of equations in $\delta\boldsymbol{d}$, $\delta[\![\boldsymbol{u}]\!]$.

$$\begin{bmatrix} \boldsymbol{K}_{\bar{u}\bar{u}} & \boldsymbol{K}_{\bar{u}u'} \\ \boldsymbol{K}_{u'\bar{u}} & \boldsymbol{K}_{u'u'} \end{bmatrix} \begin{bmatrix} \delta\boldsymbol{d} \\ \delta[\![\boldsymbol{u}]\!] \end{bmatrix} = \begin{bmatrix} -\bar{\boldsymbol{r}} \\ -\boldsymbol{r'} \end{bmatrix} \tag{3.1.19}$$

where

$$\boldsymbol{K}_{\bar{u}\bar{u}} = \int_{\Omega} \boldsymbol{B}^{\boldsymbol{T}} \mathbb{C} \boldsymbol{B}\, dV \tag{3.1.20}$$

$$\boldsymbol{K}_{\bar{u}u'} = \int_{\Omega} \boldsymbol{B}^{\boldsymbol{T}} \mathbb{C} \boldsymbol{G}\, dV \tag{3.1.21}$$

$$\boldsymbol{K}_{u'\bar{u}} = \boldsymbol{H}^{\boldsymbol{T}} \mathbb{C} \boldsymbol{B} \tag{3.1.22}$$

$$\boldsymbol{K}_{u'u'} = \boldsymbol{H}^{\boldsymbol{T}} \mathbb{C} \boldsymbol{G} + \mathcal{H}_{\boldsymbol{n}} \boldsymbol{n} \otimes \boldsymbol{n} + \mathcal{H}_{\boldsymbol{m}} \boldsymbol{m} \otimes \boldsymbol{m} \tag{3.1.23}$$

The above finite element equations are solved using the static condensation method

[48].

3.2 Cohesive Model for Fatigue

An important requirement for any phenomenologically based fatigue model is that it should be able to represent material degradation over time. The law we have used to represent this degradation is a modified form of the fatigue cohesive law developed by Maiti and Geubelle [37]. As shown in Figure 3.4, for monotonic failure, the law is linear, whereas the law represents nonlinear behavior during cyclic loading. The main feature of this fatigue cohesive model is the difference between the loading and unloading paths in the traction-separation curve. This characteristic promotes sub-critical crack growth under cyclic loading due to progressive degradation of the cohesive properties, i.e. the slope of the traction-separation law.

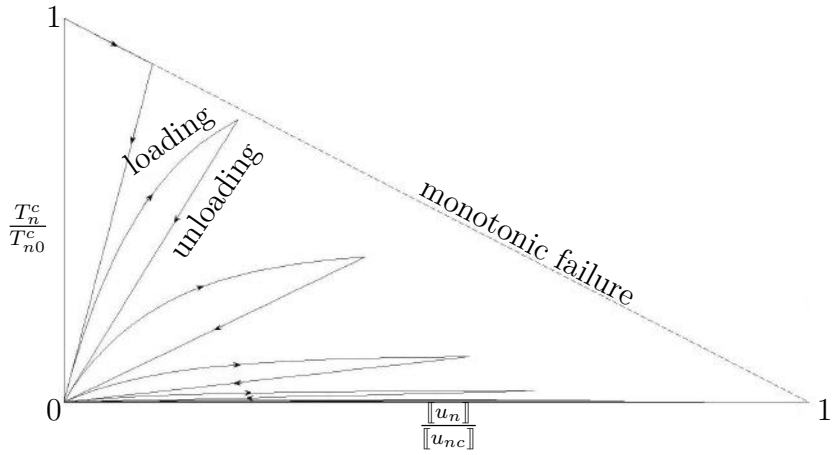

Figure 3.4: Subcritical vs. critical failure. T_{n0}^c and $[\![u_{nc}]\!]$ are mode I critical opening traction and displacement, respectively.

The instantaneous mode I cohesive stiffness $\mathcal{H}_n$ during reloading can be expressed as a nonlinear function of cohesive traction T_n^c and number of fatigue cycles as

$$\mathcal{H}_n = \frac{dT_n^c}{d[\![u_n]\!]} = f(T_n^c, N_f) \tag{3.2.1}$$

where N_f denotes the number of loading cycles experienced by a material point since the onset of failure, T_n^c denotes the normal component of traction on the crack face and $[\![u_n]\!]$ is the normal component of the displacement discontinuity on the crack face. A similar expression can be written for mode II failure. A two-parameter power law relationship can be used to model the rate of decay of the cohesive stiffness $\mathcal{H}_n$.

$$\mathcal{H}_n = f(T_n^c, N_f) = -\gamma(N_f) T_n^c \tag{3.2.2}$$

where

$$\gamma = \frac{1}{\alpha} N_f^{-\beta} \tag{3.2.3}$$

Here α and β are cohesive parameters that are related to the degradation of the cohesive strength. The cohesive parameter α has the dimension of length while β denotes the history dependence of the failure process. Both of these parameters account for the unloading-reloading hysteresis. The inclusion of this hysteresis may, in the phenomenological sense, account for the dissipative mechanism arising from reverse yielding upon unloading. Reverse yielding upon unloading may occur when the crack growth happens as a result of alternating crystallographic slip [100]. This dissipative mechanism can also be caused as a result of repeated rubbing of asperities, which may cause steady weakening of the cohesive surfaces. A simple phenomenological model that incorporates this assumption has been built by relating the cohesive stiffness to the number of loading cycles through a power law relationship (Eq. (3.2.2)). The above evolution law can be expressed in terms of the rate of change of the cohesive stiffness $\mathcal{H}_n$ as

$$\dot{\mathcal{H}_n} = \begin{cases} -\frac{1}{\alpha} N_f^{-\beta} \mathcal{H}_n [\![\dot{u_n}]\!] & [\![\dot{u_n}]\!] \geqslant 0 \\ 0 & [\![\dot{u_n}]\!] < 0 \end{cases} \tag{3.2.4}$$

The second equation states that there is no change in cohesive stiffness during unloading cycle. Eq. (3.2.4) can be converted from the temporal to the spatial

domain and, using a 1st order finite difference approximation, can be written as

$$\mathcal{H}_n^{(i+1)} = \mathcal{H}_n^{(i)}\Big\{1 - \frac{1}{\alpha}N_f^{-\beta}\big([\![u_n]\!]^{(i+1)} - [\![u_n]\!]^{(i)}\big)\Big\} \tag{3.2.5}$$

for $[\![\dot{u_n}]\!] \geqslant 0$,

superscripts (i+1) and (i) denote the adjacent load steps in a loading cycle. Thus, the traction-separation curve slope ($\mathcal{H}_n$) is progressively degraded as the number of loading cycles increases.

There are four independent fatigue cohesive model parameters that have to be calibrated. Fracture strength (T_{n0}^c), area under the traction-separation curve, and critical displacement ($[\![u_{nc}]\!]$) are three monotonic cohesive model parameters, of which only two are independent. For fatigue fracture, material parameters α and β are the additional two parameters that have to be calibrated. We can calibrate the first two monotonic cohesive model parameters by setting T_{n0}^c equal to the fracture strength of the elastic material and the area under the traction-separation curve equal to the mode I fracture toughness G_I^c of the elastic material. The cohesive parameters α and β are calibrated from macro-scale experiments. The procedure for calibrating these two parameters is described in next section.

3.3 Results and Discussions

In this section, examples are shown using this combined method (the VMM with the CZM) called the Variational Multiscale Cohesive Method (VMCM). These examples cover different concepts within fracture mechanics and are presented to show the capability of this method. Results are provided for the macroscopic stress intensity factor, the microstructurally short crack path, and fatigue crack growth. The later example is used to show that, by varying parameters α and β, fatigue crack growth curves of different materials can be predicted and inversely cohesive parameters α

and β can also be calibrated from macro experiments. These examples demonstrate the capability of this method to model failure in materials at the macro-level as well as at the micro-level.

The objectivity of this method with respect to numerical discretization has already been demonstrated by Rudraraju et al. [48]. Unless otherwise noted, the material used is an epoxy [37] with $E = 3.9\ GPa$, $\nu = 0.4$, and mode I fracture toughness $G_{Ic} = 88.97\ J/m^2$. The mode I critical opening traction T^c_{n0} is taken to be $50\ MPa$, while the material parameters α and β are taken to be $5\ \mu m$ and 0.5, respectively. In all numerical simulations, the length of the elements in front of the crack tip is defined to be smaller than $\frac{\pi}{8}\frac{E}{(1-\nu^2)}\frac{G_{Ic}}{\sigma_{avg}}$ [37] so that the fracture process is accurately captured in this region. Here, σ_{avg} $(T^c_{n0}/2)$ is the average stress in the cohesive zone.

To concentrate more on the accuracy and benefits of this method, we present only the local mode I simulation. Mode II and mixed-mode simulation can quite easily be carried out using this method. An in-house C++ based code has been developed to produce data for all the examples presented in this section. To solve the nonlinear equations that arise from the finite element formulations, a Newton-Raphson iterative scheme is used.

3.3.1 Comparison of the Linear Elastic Stress Intensity Factor and the J-Integral Stress Intensity Factor

A comparison between the theoretical stress intensity factor and the numerical stress intensity factor is important to determine the accuracy of the stress field surrounding the crack using the VMM approach. This serves as a basic verification of the numerical method. The theoretical mode I stress intensity factor (SIF) is calculated from a linear elastic fracture mechanics (LEFM) solution, while the numerical SIF is calculated using the J-integral method [112]. The SIF from linear elastic fracture

mechanics is given by [113]

$$K_I = \sigma\sqrt{\pi\, a}\left\{1.12 - 0.23\, a/b + 10.6\,(a/b)^2 \right. \\ \left. -21.7\,(a/b)^3 + 30.4\,(a/b)^4\right\} \tag{3.3.1}$$

where σ is the applied stress, b is the height of the specimen and a is the crack length. The J-integral SIF is calculated along the contour Γ surrounding the boundary of a cohesive zone as shown in Figure 3.5; this is given by Eq. (3.3.2).

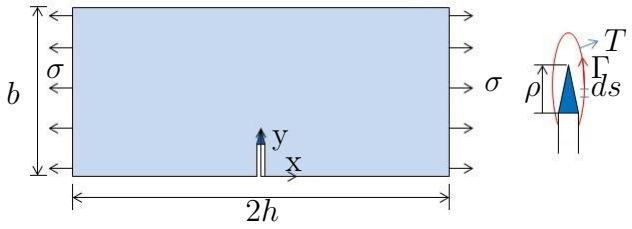

Figure 3.5: J-integral path taken around the cohesive zone, $b = 1mm$ (Cohesive zone length $\rho \approx 0.08mm$)

$$J = \int_{\Gamma}\left(W\, dy - T_i\frac{\partial u_i}{\partial x}ds\right) \tag{3.3.2}$$

where W is the strain energy density, T_i is the ith component of the traction vector perpendicular to Γ in the outward direction, u_i is the ith component of the displacement vector, and ds is an arc length element along contour Γ. For plane strain conditions, the following relation is given by Rice [112]

$$K_I = \left[\frac{JE}{(1-\nu^2)}\right]^{1/2} \tag{3.3.3}$$

The LEFM requirement of small scale yielding imposes the condition that the cohesive zone size should be much less than the crack length ($\rho < a$) in order for the stress field outside the cohesive zone to be nearly the same as the K-dominant stress field. Thus, the cohesive zone size maintains a constant value of $\rho \approx\ 0.08mm$, which

is smaller than the initial crack length $a = 0.1\ mm$.

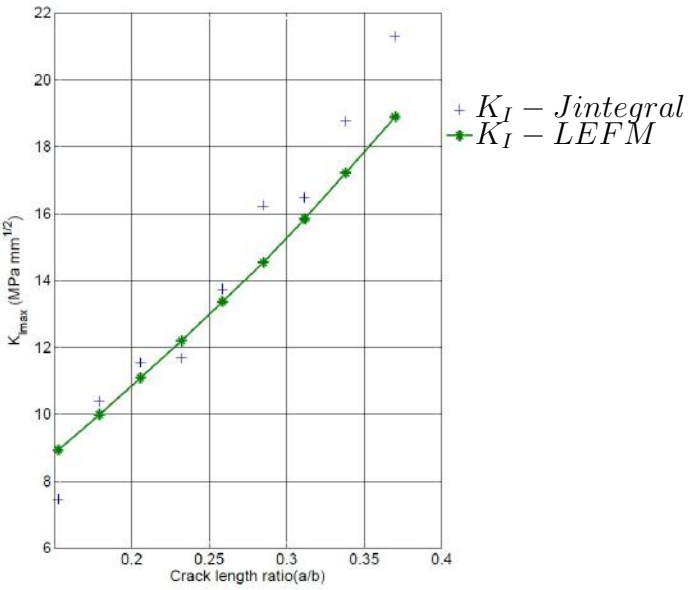

Figure 3.6: Comparison between LEFM SIF and J-integral SIF

The simulation parameters for calculating the J-integral from the FEM domain are the same as those used in the previous section.

As can be seen in Figure 3.6, the numerically computed values for the SIF using the J-integral method are close to the SIF values predicted by LEFM. The small discrepancy between the two results can be attributed to the size of the cohesive zone, since the LEFM solution is valid only for small-scale yielding. Thus, using the VMCM, we can accurately capture the stress field surrounding the crack.

3.3.2 Microstructurally Short Surface Crack Propagation

The subject of microstructurally short crack growth is used to show the ability of the VMCM to model two-dimensional microstructural failure. Microstructurally short crack growth refers to crack growth inside a grain (called trans-granular fracture) or at the grain boundaries (called inter-granular fracture). In this section, we show numerical simulation of crack growth across multiple grains where the crack could be a mixture of inter-granular and trans-granular fracture. In trans-granular fracture,

the crack can follow either the slip planes or a plane lying in-between the slip planes.

The material model we use in our simulation is a hexagonal closed packed (HCP) Mg alloy, WE43, with five elastic constants and two lattice constants, as shown below:

$$C_{11} = 58\ GPa, C_{12} = 25\ GPa, C_{13} = 20.8\ GPa,$$
$$C_{33} = 61.2\ GPa, C_{55} = 16.6\ GPa.$$
$$c = 5.21\mathring{A}, a = 3.21\mathring{A}$$

The material orientation data for individual grains are obtained from electron backscatter diffraction (EBSD) mapping (see Figure 3.7), and the crack growth path image is obtained from scanning electron microscopy(SEM) of the WE43 surface [114]. Using the grain orientations (Euler-Bunge angles), elastic constants for individual grains are transformed from the crystal frame to the global simulation frame. These transformed 3D elastic constants are converted to 2D using plane stress assumptions. This way, the VMM is combined with 2D crystal elasticity to model microstructurally short crack growth. The mathematical formulations are similar to those described in Section 3.1, where the microstructural domain contains the grain boundaries and $\mathbb{C}$ in Eq. (3.1.13) is the transformed 2D elastic anisotropic stiffness matrix.

The HCP Mg has, in total, 18 slip systems, 3 basal $< a >$, 3 prismatic $< a >$, 6 pyramidal $< a >$, and 6 pyramidal $< c + a >$ slip systems. In pure Mg, the primary slip plane is the basal plane, but when Mg is alloyed with other elements, other slip planes become active. In the case of WE43, the crack growth mostly occurs along the basal and the pyramidal $< a >$ planes [114]. To model a surface crack propagation problem using plane stress assumptions we use slip lines inside the grains. The slip lines are the intersections of the slip planes (basal and pyramidal $< a >$) and the simulation plane. For our simulation, we use 1 basal slip line and 3 pyramidal$< a >$ slip lines for simplicity. The crystal parameters for these 2 slip lines are taken from

Choi et al. [115] and are shown below:

$$T_{crss}^{basal} = 25\ MPa,\ T_{crss}^{pyramidal} = 68\ MPa$$

$$T_{c}^{gb} = 83\ MPa,\ T_{c}^{gb\ cross} = 100\ MPa$$

T_{crss} above corresponds to the critical resolved shear stress or the fracture strength of the slip plane, T_c^{gb} represents the grain boundary strength, and $T_c^{gb\ cross}$ is the increased grain boundary strength. The grain boundaries act as microstructural barriers to short crack propagation, the strength of which varies with the crystallographic orientation relationship. The higher the tilt and twist mis-orientation angles between adjacent slip bands the more effective the grain boundaries are as barriers to the transmission of slip into the adjacent grains. This also holds true for the crack growth from one grain to another grain across a grain boundary, and this increased grain boundary strength is labeled here as $T_c^{gb\ cross}$. A constant value of $T_c^{gb\ cross}$ is used to concentrate more on the varied applications of the VMCM. The crack growth along the slip lines is characterized as mode II fracture, while the crack growth along the grain boundary is mode I fracture.

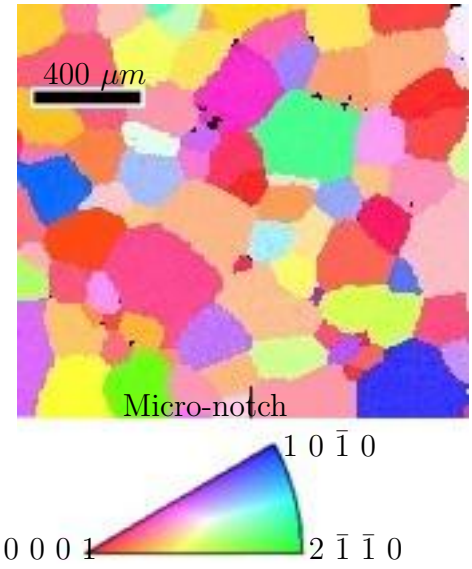

Figure 3.7: EBSD image with orientation data of a Mg WE43 experimental specimen [114]

In this simulation, there are six cohesive traction-separation laws to account for 1 basal slip crack (mode II), 3 pyramidal slips crack (mode II), 1 grain boundary cracking (mode I), and 1 grain boundary crossing. For all these laws, we assume a critical sliding/opening displacement value of 0.1 μm.

For a tension test, in a elastic material, the crack on the macroscopic level will grow perpendicular to the direction of the maximum principal stress. However, at the microscopic level, the cracks can only grow along certain planes within a grain. These planes are the slip planes, and for a Mg WE43 alloy, the crack grows predominantly along the basal plane and the pyramidal plane [114]. Thus, to model this crack path, we developed a crack tracking algorithm that takes into account all of these paths. At the crack tip, the algorithm searches through all the favorable lines (i.e. 1 basal and 3 pyramidal planes within a grain or 1 basal, 3 pyramidal, and 1 grain boundary at the grain boundary) that meet the fracture criteria and selects the line whose normal is closest to the maximum principal stress direction. This way, the crack grows along the slip lines and/or along the grain boundaries.

The finite element mesh for this model is created using a real microstructural image. The model domain consists of 82 grains with different orientations as shown in the color plot (Figure 3.7). The grain edges of this real microstructure are generated using ImageJ [116], and then the OOF [117] program is used to generate a finite element mesh from these edges. The steps outlined above are shown in Figure 3.8. The size of the micro-notch in Figure 3.8(c) is similar to the size of experimental micro-notch.

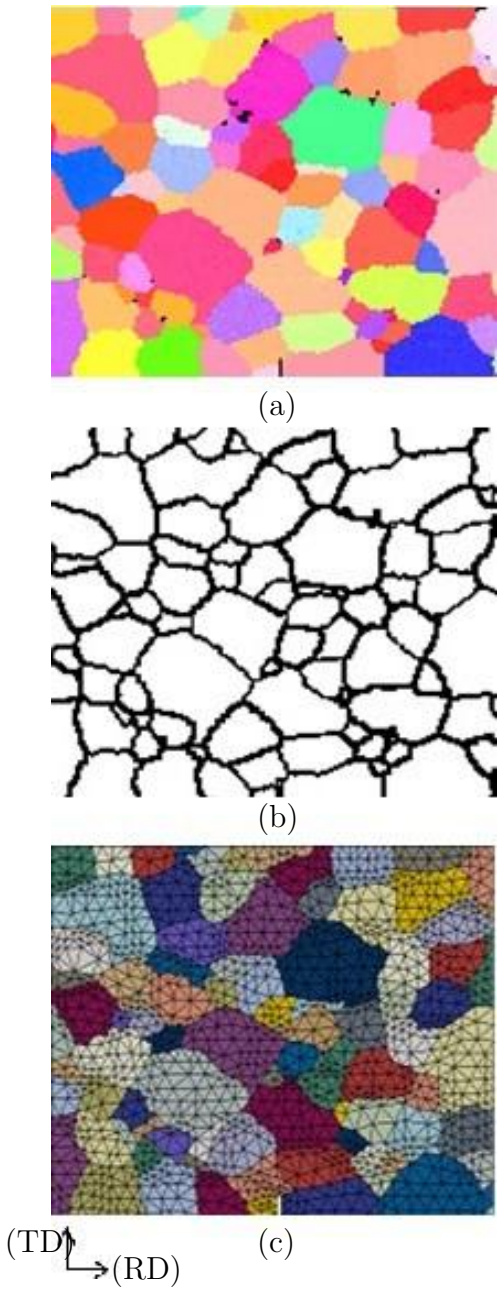

Figure 3.8: FE mesh generated from a real microstructure image, RD - Rolled direction, TD - Transverse direction. (a) EBSD image [114] (b) Grains edges generated from ImageJ [116] (c) FE mesh generated from OOF [117] with colors shown only for distinguishing different grains

The boundary conditions for this simulation are applied so as to match the experimental boundary conditions. In the experiment, the specimen is loaded in tension along the RD direction [114]. To produce similar loads on our model boundaries,

we apply tensile loads on the left and right boundaries of Figure 3.8(c), while loads from Poisson's effect ($\nu = 0.27$) are applied on the top and bottom boundaries. The loading is applied until the microstructural crack reaches the domain boundary.

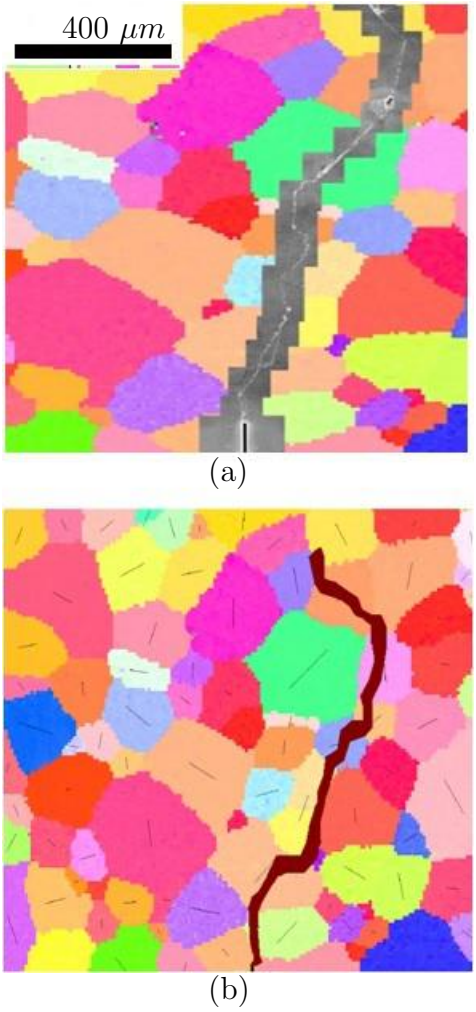

Figure 3.9: Comparison of experimental crack path and numerical crack path. (a) Experimental crack image - SEM crack image superimposed on EBSD image [114] (b) VMCM crack path (shown in dark red) superimposed on EBSD image with basal slip lines shown in each grain

In Figure 3.9, we show the comparison between the experimental crack path and our numerical crack path. Figure 3.9(b) is a superposition of the EBSD image with the numerical crack path. This figure also contains basal slip lines to show that the crack growth inside a grain closely follows these slip lines. On comparing these two figures (Figure 3.9(a) and (b)), we see that the crack path predicted using the VMCM

method is close to the experimental crack path even when using a coarse mesh. The differences between these two crack paths maybe due to our assumptions of constant grain boundary strength (T_c^{gb}) and plane stress and due to the use of a constant $T_c^{gb\ cross}$ value for all grain boundaries. These parameters need to be more carefully calibrated for the alloy from lower-scale simulations and/or experiments so that the crack path can be better reproduced. The short fatigue crack growth can also be modeled using the VMCM. However, for each cohesive law, there are two additional parameters α and β that have to be calibrated, along with the above-mentioned parameters. The fatigue parameters α and β are linked to each slip system. Thus, experimental fatigue crack growth rates for each individual slip system are needed to calibrate these two parameters. The crack growth rates for each slip system can be measured through method, such as beachmarking [118] or striations.

3.3.3 'Local' mode I Fatigue Crack Growth

For fatigue crack growth, we have again considered the SENT specimen (Figure 3.5). The crack evolution is considered to be 'local' mode I, which implies that, in the direction of crack path, there is no shear stress, and the mode II fracture toughness is zero. In Figure 3.5, the left boundary of the specimen has no displacement in the x-direction, and the bottom left corner of the specimen has zero displacement in the y-direction. Fatigue tests of specimens are carried out under displacement-controlled tension loading (Figure 3.10). The shape of the applied displacement does not affect the fatigue behavior, as the rate dependence of the material is ignored. The maximum displacement Δ_{max} is taken to be $0.009b$, the initial crack length is $a_0 = 0.1b$, and the amplitude ratio R ($\frac{\sigma_{max}}{\sigma_{min}}$) is 0.

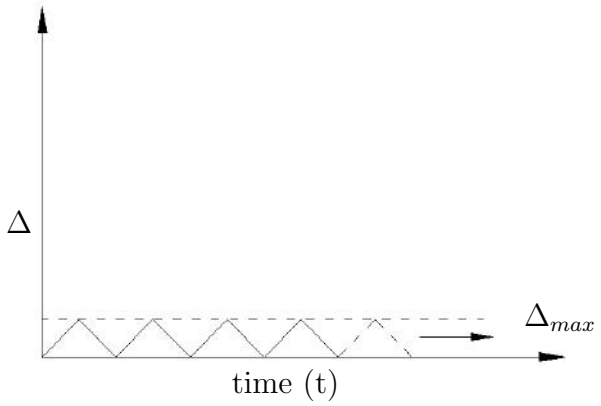

Figure 3.10: Variation of applied displacement Δ with time

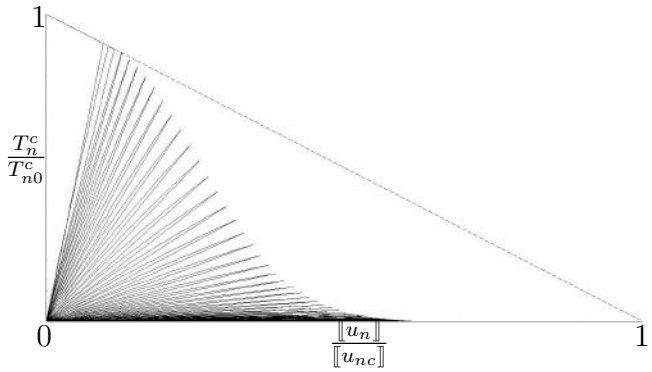

Figure 3.11: Evolution of traction-separation curve for a point on the cohesive zone

Figure 3.11 shows the evolution of traction-separation for a point on the cohesive zone. In the finite element model, this is the third element in the crack path. We can clearly see the dissipation between the loading-unloading cycles in this element. The dotted line in this figure is the monotonic failure line and is shown to indicate the sub-critical nature of the fatigue cracks. The nonlinear nature of the maximum crack opening traction per cycle can also be clearly seen in this figure.

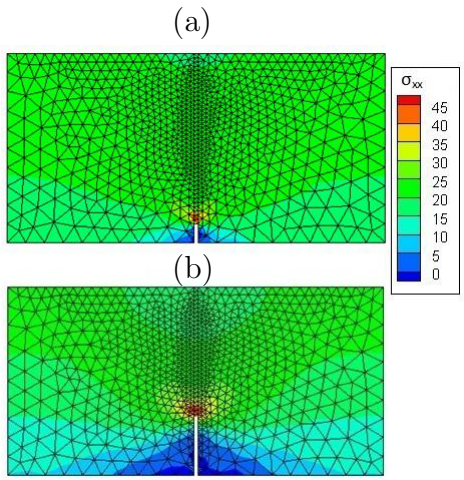

Figure 3.12: σ_{xx} stress (MPa) distribution for 'local' mode I fatigue crack growth. (a) Stress distribution at the end of the first cycle (b) Stress distribution at the end of 2200 cycles (cracked elements have been removed from the plot)

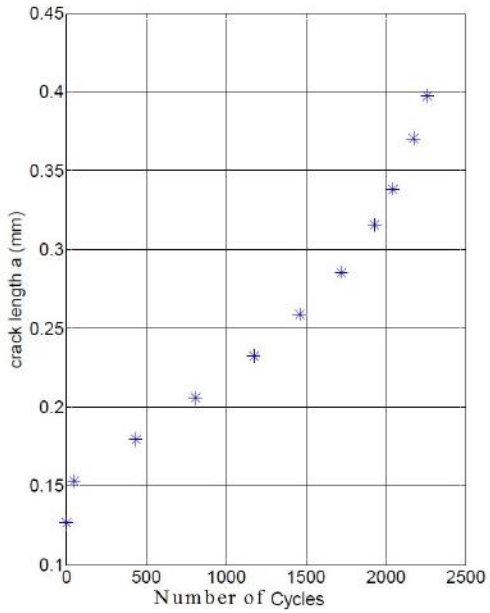

Figure 3.13: Fatigue crack growth in SENT specimen versus the number of loading cycles

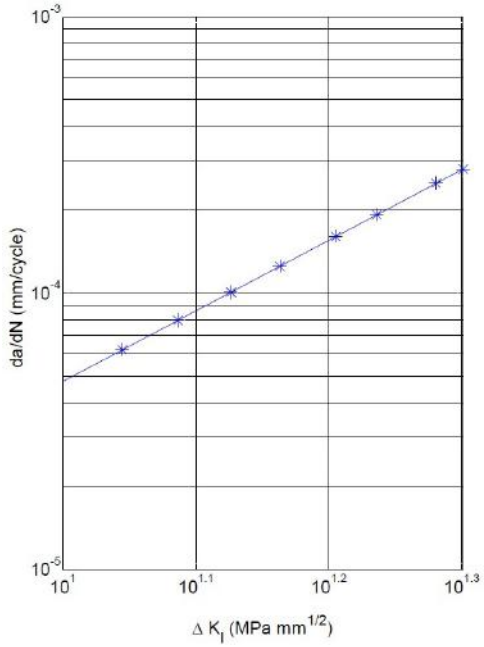

Figure 3.14: Paris curve, $\alpha = 5\mu m$ and $\beta = 0.5$

Figure 3.12 shows σ_{xx} distribution snapshots taken at different cycles. The crack has propagated ≈ 0.3 times the total width of the specimen after 2200 cycles. After this cycle,

$$K_I = 22\,MPa\sqrt{mm}\ (\approx K_{Ic} = 22.21\,MPa\sqrt{mm}) \tag{3.3.4}$$

and the crack propagates rapidly, indicating the final failure (K_{Ic} is monotonic fracture toughness) is as predicted by the LEFM solution.

As can be inferred from the above statement, the curve of the crack path versus the number of loading cycles (Figure 3.13) should be asymptotic. This is the expected behavior of the fatigue crack growth in the case of a SENT specimen. To get the Paris curve, we need the applied stress intensity factor. The applied stress intensity factor (K_I) is calculated using the J-integral method [112]. The details of K_I calculation are given in Section 3.3.1. By differentiating the crack length with respect to the number of loading cycles (Figure 3.13), we can calculate the crack growth rate (da/dN) and plot it versus the change in stress intensity factor (ΔK_I). This curve represents the steady state crack growth rate (Figure 3.14). The curve captures the final failure quite

well as indicated by Eq. (3.3.4). The slope of this curve (Figure 3.14) is $m = 2.5$ and the intercept $C \approx 10^{-07}$ mm/cycle.

3.3.4 Effect of Parameters α and β on the Paris Curve

In this section, we do a parametric study on the effect of cohesive parameters α and β on the crack growth rate and the Paris curve. Figure 3.15 plots crack tip advancement versus the number of loading cycles for three different values of α, while $\beta = 0.2$ is kept constant. As can be seen in this figure, the crack growth rate decreases as α increases. For $\alpha = 2$ μm, the crack advances nearly 0.4 times the width of the specimen in 80 cycles, whereas, for $\alpha = 5$ μm, the crack takes around 240 cycles to advance the same distance. Differentiating the crack length with respect to the number of cycles, we can plot (Figure 3.16) the crack growth rate (da/dN) versus the change in stress intensity factor (ΔK_I). Thus, for different values of α, we get Paris curves with different intercepts ($C = 1 \times 10^{-06}$ to 3×10^{-06} mm/cycle). Thus, for the same stress intensity factor we can get different crack growth rates and by changing α we can change these rates.

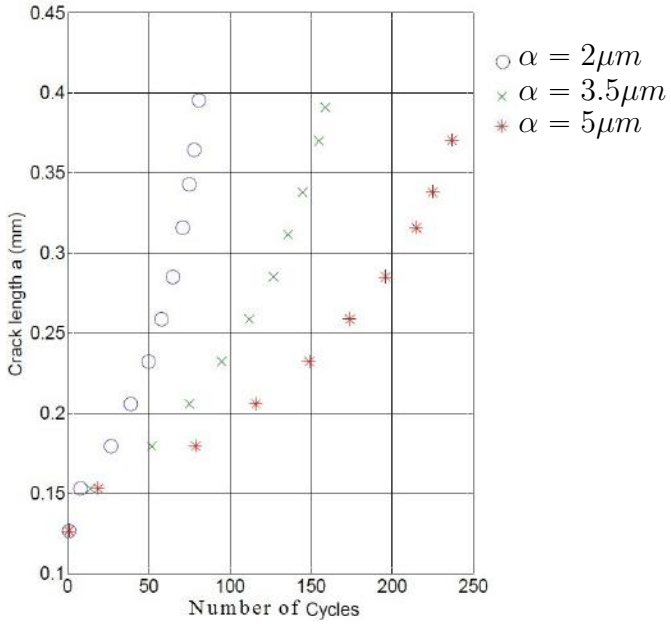

Figure 3.15: Effect of α parameter on crack propagation ($\beta = 0.2$)

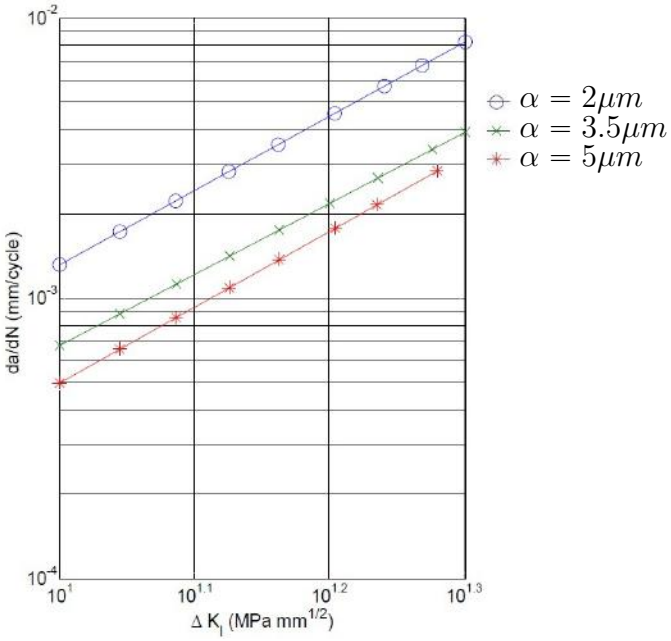

Figure 3.16: Paris curves for different values of α ($\beta = 0.2$)

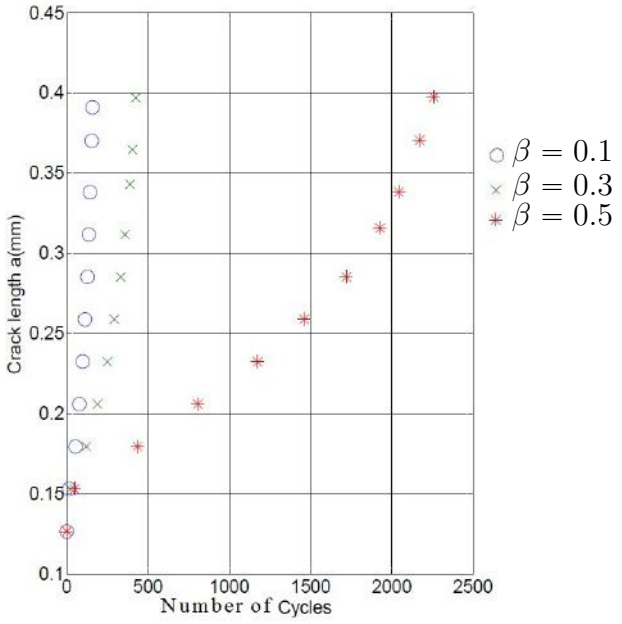

Figure 3.17: Effect of β parameter on crack propagation ($\alpha = 5\mu m$)

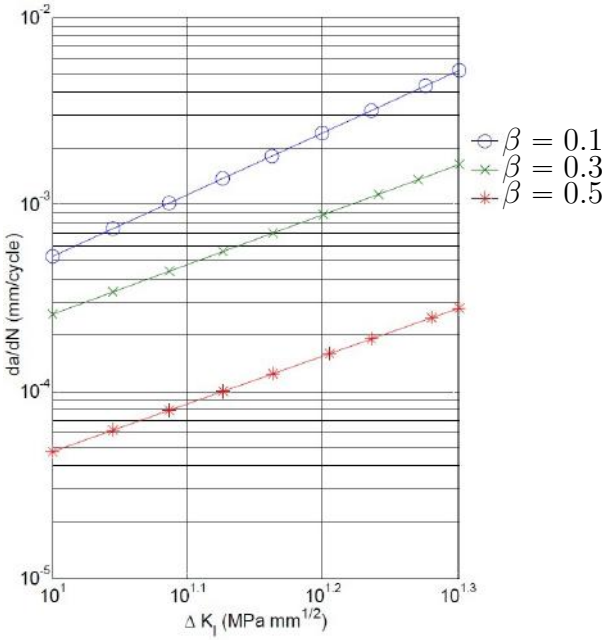

Figure 3.18: Paris curves for different values of β ($\alpha = 5$ μm)

In Figure 3.17, the plot of crack length versus number of cycles for different β-values is shown. For different values of β (0.1, 0.3, and 0.5), the crack growth rate changes, and by differentiating these curves we get different Paris curves (Figure 3.18) with different slopes ($m = 2.5$ to 3.3 , $C \approx 10^{-07}$ mm/cycle). Thus, by changing these two parameters, one can obtain Paris curves for different materials.

This procedure is followed with Polystyrene [119], which has $E = 3.1$ GPa, $\nu = 0.35$, and mode I fracture toughness $G_{Ic} = 1164.52$ J/m^2. The mode I critical opening traction T^c_{n0} is taken to be equal to the craze stress, 38 MPa [119]. The parameters α and β are calibrated from the experimental data [120], and the parameters are found to be in the range of $0.03 - 0.05$ mm and 0.5, respectively (Figure 3.19). The simulations were run on 150 mm x 50 mm x 3 mm SENT specimens with an initial crack length of $a_0 = 20$ mm [119].

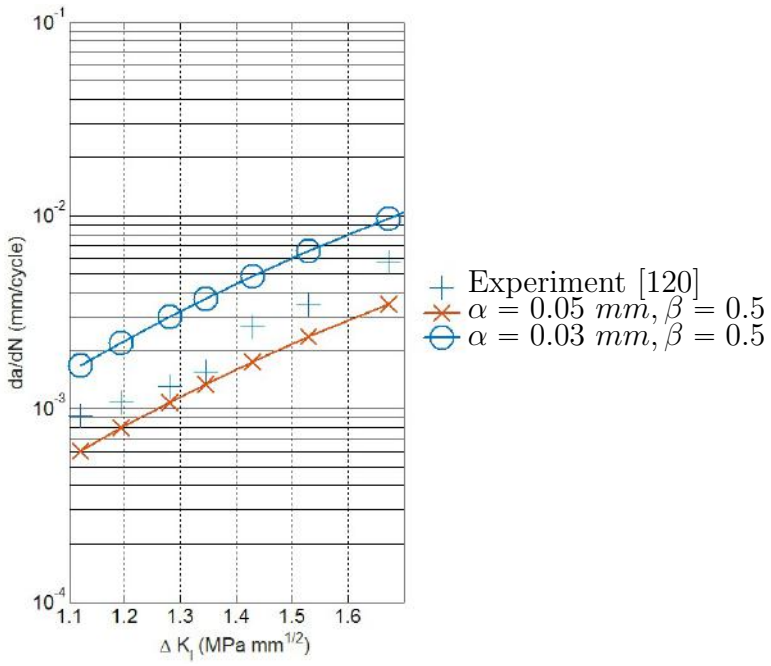

Figure 3.19: α and β parameters calibrated for Polystyrene [120]

3.4 Conclusion

Modeling fatigue failure is valuable for predictive modeling of component life and ensuring structural integrity in aerospace structures. In this chapter, the variational multiscale method (VMM) is used to model fatigue crack propagation for the first time. In this approach, a discontinuous displacement field is added to elements that exceed the critical values of normal or tangential traction during loading. This additional degree of freedom is represented within the cracked element using a special discontinuous shape function, which ensures that the displacement jump is localized to that particular element. The finite element formulation and code implementation details are presented. Compared to traditional cohesive zone modeling approaches, this method does not require the use of any special interface elements in the microstructure. This method is shown to produce accurate stress field near the crack tip. A microstructurally short crack growth simulation is performed along with an experimental comparison to demonstrate the accuracy of this method in predicting

microscopic crack paths and mixed-mode failure. A two-parameter phenomenological fatigue cohesive law is incorporated into the VMM via a traction continuity equation. The relationship between the phenomenological model parameters and the slope and intercept of the Paris curve are shown. We have shown that different Paris curves can be simulated by varying the parameters in the cohesive law. As an example, we have performed a comparison between our fatigue model and published experimental data. In Chapter IV, we focus on developing a micro-mechanical interpretation of these parameters and their calibration with experimental data.

CHAPTER IV

Dislocation Theory-Based Cohesive Model for Microstructurally Short Fatigue Crack Growth

[1] In this chapter, a continuous representation of dislocations is used to represent a mode II crack and the associated plastic zone. In the original formulation of dislocation theory, the friction stress that opposes the motion of the dislocations is represented by a constant stress (BCS model [55]). Both the BCS model and the model proposed by Taira et al., for crack and associated plastic zone blocked by a grain boundary (Taira-Tanaka-Nakai model [56]), assume that the friction stress opposing the dislocation motion is the local yield stress of the material. In our new formulation, we embed a cohesive zone in the plastic region in front of a crack tip by representing the friction stress as a function of the crack displacement. This allows cohesive zone models (obtainable from a lower scale simulation, such as molecular dynamics) to be integrated into a dislocation theory-based model, for the first time, to predict short crack growth. The details of this new formulation are shown for the two cases: the crack and the associated plastic zone inside a grain, and the crack and the associated plastic zone tip at the grain boundary. The main features of this new model are discussed along with an experimental comparison to the case of mi-

[1] Reproduced from Shardul Panwar and Veera Sundararaghavan. Dislocation theory-based cohesive model for microstructurally short fatigue crack growth. *Materials Science and Engineering: A*, 708:395–404, 2017

crostructurally short fatigue crack growth across two grains in a Ni-based CMSX-4 alloy.

This chapter has been divided into four sections. Section 4.1 gives an introduction of the BCS and Taira-Tanaka-Nakai formulations. Section 4.2 details our new formulation that combines the cohesive zone model with first the BCS model and then the Taira-Tanaka-Nakai model. We call this new formulation the Cohesive-BCS model. As has been done in Taira et al. [56], this new formulation is extended to fatigue in Section 4.3. In Section 4.4, the new features of this model are compared to those of the BCS and Taira-Tanaka-Nakai models. Finally, the new formulation is utilized in the prediction of microstructurally short fatigue crack growth rates in a Ni-based CMSX-4 specimen and results are compared to experiments [121].

4.1 The BCS and Taira-Tanaka-Nakai models

Based on the theory of continuously distributed dislocations [63], Bilby et al. [55] have derived the dislocation density expression for a uniformly stressed solid containing a notch with a plastic zone in the front. This is called a bounded solution, since the dislocation density is bounded at the plastic tip. Taira et al. [56] have derived the dislocation density expression for a slip band that is blocked at a grain boundary and is emanating from a crack tip. This solution is referred to as an unbounded solution, since the dislocation density is unbounded at the plastic tip due to the dislocation pile up. Both of these solutions are employed to calculate the microstructurally short fatigue crack growth rate across multiple grains by assuming that the crack growth rate is proportional to the crack tip displacement [61]. Using this assumption, the bounded solution gives the crack growth rate when the crack and the associated plastic zone are inside a grain (Figure 4.1), while the unbounded solution gives the crack growth rate when the plastic zone is blocked by a grain boundary (Figure 4.2).

This section is structured in two parts: Part I describes the important expressions for the bounded solution of the dislocation density, and Part II shows the dislocation distribution expression for the unbounded solution and the expression for the stress distribution in front of the plastic tip blocked by a grain boundary.

4.1.1 Part I: The bounded solution from the BCS model

In the BCS model, the plastic zone in front of the crack tip is simplified by assuming that it is in the same plane as the crack plane (Figure 4.1). Within the plastic zone, the friction stress $\tau_f(x)$ that resists the dislocation motion is assumed to be equal to the yield stress. The crack faces are considered to be traction free. The crack tip in this chapter is always at $x = \pm a,\ y = 0$, while the plastic tip is always at $x = \pm c,\ y = 0$.

The dislocation distribution that exists on the traction free crack plane ($-a < x < a$) has a stress associated with it. This stress $\tau(x)$ should be in equilibrium with the applied stress. Thus,

$$\begin{aligned} \tau(x) + \tau_A &= 0 \\ \tau(x) &= -\tau_A \end{aligned} \tag{4.1.1}$$

Moreover, the stress $\tau(x)$ produced by the dislocation distribution inside the plastic zone ($a < |x| < c$) is resisted by the friction stress $\tau_f(x)$. This resistance should be in equilibrium with the applied stress τ_A. Thus,

$$\begin{aligned} \tau_f(x) - \tau(x) &= \tau_A \\ \tau(x) &= \tau_f(x) - \tau_A \end{aligned} \tag{4.1.2}$$

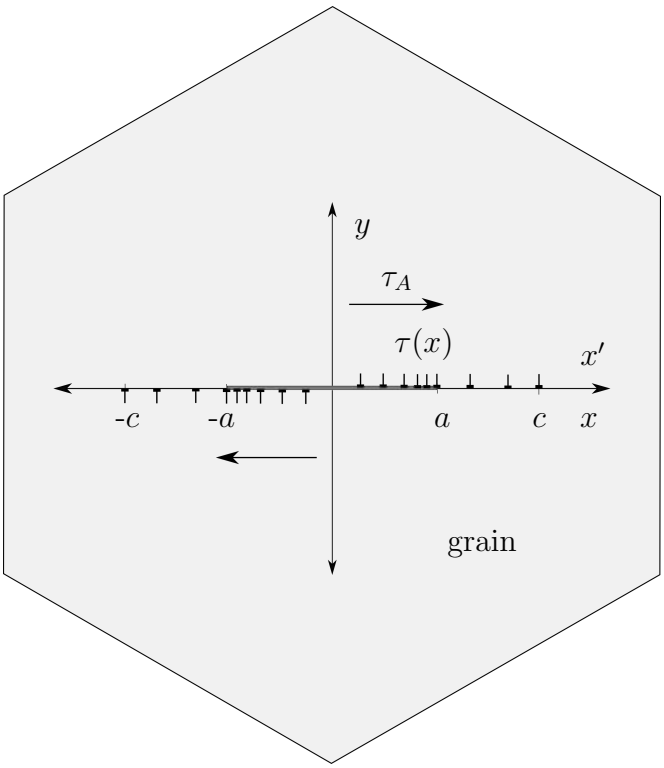

Figure 4.1: Dislocation distribution under an applied shear stress τ_A

In Figure 4.1, the shear stress at x due to the presence of a dislocation at x' is given by

$$\tau(x) = \frac{G}{2\pi\alpha}\int_{-c}^{c}\frac{B(x')}{x-x'}dx',\ -c<x<c \tag{4.1.3}$$

The above expression (Eq. (4.1.3)) is solved for the dislocation density $B(x)$ by Muskhelishvili's inversion formula [69]. The final expression is

$$B(x) = -\frac{2\alpha\sqrt{c^2-x^2}}{\pi G}\int_{-c}^{c}\frac{\tau(x')}{(x-x')\sqrt{c^2-x'^2}}dx',\quad -c<x<c \tag{4.1.4}$$

and the condition for the dislocation density $B(x)$ to be bounded at $x=\pm c$ is given by

$$\int_{-c}^{c}\frac{\tau(x)}{\sqrt{c^2-x^2}}dx = 0 \tag{4.1.5}$$

In the above expressions (Eqs. (4.1.4) and (4.1.5)), c represents the half length of the crack and the associated plastic zone, G is the shear modulus, $\alpha = 1$ for screw dislocation, $\alpha = 1 - \nu$ for edge dislocation, and ν is the Poisson's ratio. In general, c must also satisfy another condition [122], given by

$$\int_{-c}^{c} \frac{x\tau(x)}{\sqrt{c^2 - x^2}} dx = \frac{Gb_T}{2\alpha} \tag{4.1.6}$$

Here, $b_T = b_R + b_L$ is the net Burgers vector of all the dislocations, b_R is the net Burgers vector of the dislocations in the positive x direction, $0 < x < \infty$, and b_L is the net Burgers vector of the dislocations in the negative x direction, $-\infty < x < 0$. If $\tau(x)$ is a symmetric function of x, then $b_T = 0$ and Eq. (4.1.6) is satisfied by symmetry, regardless of the value of c.

Eq. (4.1.4) contains a singular kernel and is solved in the Cauchy principal value sense. Eq. (4.1.5) is called the existence condition, and it determines the length of the plastic zone $(c - a)$.

4.1.2 Part II: The unbounded solution from the Taira-Tanaka-Nakai model

Taira et al. [56] found that the BCS model can be used in the analysis of crystallographic slip bands emanating from the crack tip. They showed that, when these slip bands are on the order of the grain size, they can be influenced by a grain boundary (Figure 4.2). To incorporate the interaction of the grain boundary with the dislocations, Eq. (4.1.3) is solved considering the dislocation density function to be unbounded at the plastic tip [69]. This adds an additional term to Eq. (4.1.4), and

the final equation becomes

$$B(x) = -\frac{2\alpha\sqrt{c^2-x^2}}{\pi G}\int_{-c}^{c}\frac{\tau(x')}{(x-x')\sqrt{c^2-x'^2}}dx' - \frac{2\alpha}{\pi G}\frac{x}{\sqrt{c^2-x^2}}\int_{-c}^{c}\frac{\tau(x')}{\sqrt{c^2-x'^2}}dx'$$
$$, -c < x < c \tag{4.1.7}$$

Here,

$$\tau(x') = -\tau_A, \quad |x'| < a$$
$$\tau(x') = \tau_f(x') - \tau_A, \quad a < |x'| < c$$

The additional term in Eq. (4.1.7) is a delta-type function; a repulsive stress field, rising suddenly from zero to infinity, locks the leading dislocation. The integrand is the same as in the existence condition, Eq. (4.1.5), while the coefficient $\frac{x}{\sqrt{c^2-x^2}}$ makes the dislocation density infinite at the grain boundary, $x = \pm c$. The length of the plastic zone is calculated from the grain size.

A stress ($S(r_0)$) at a point that is at a distance r_0 away from the grain boundary on the grain 2 slip plane (Figure 4.2) is given in [63] by

$$S(r_0) = \frac{Gb}{2\pi\alpha}\int_{-c}^{c}\frac{B(x)}{x'-x}dx + \tau_A, \quad x' = c + r_0, \ |x'| > c \tag{4.1.8}$$

where b is the burgers vector.

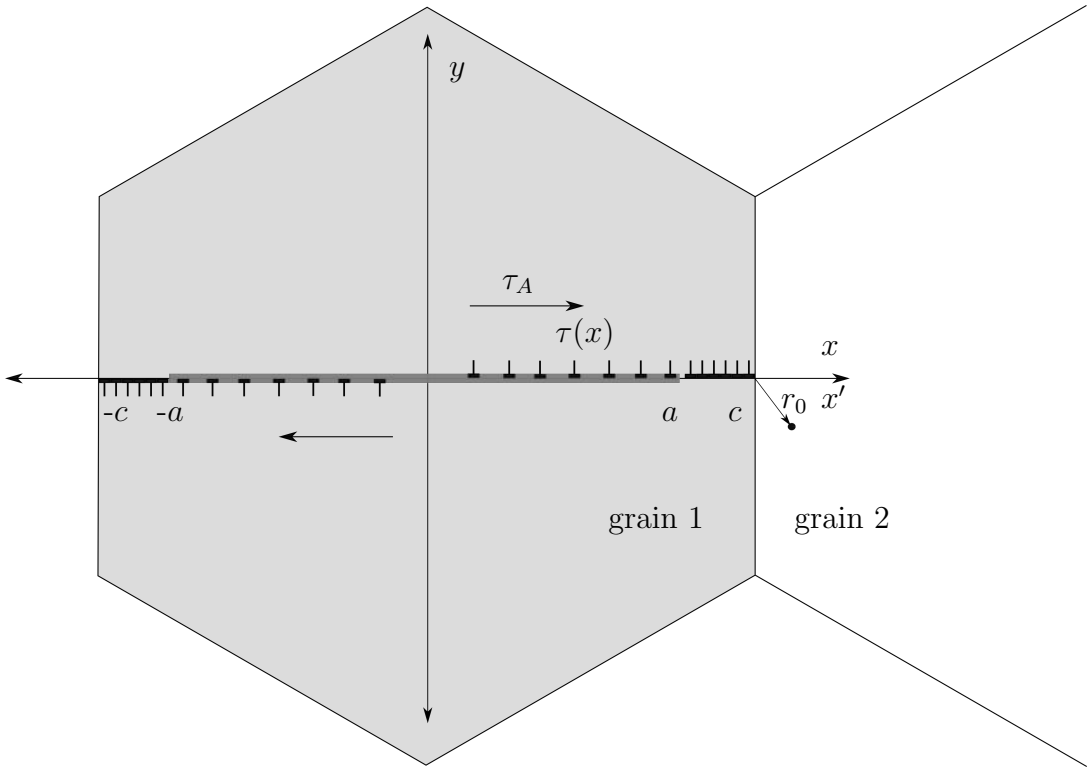

Figure 4.2: The tip of the crack and the associated plastic zone is at the grain boundary. r_0 is the distance from the grain boundary to a slip system in grain 2.

For both the models, the dislocation density $B(x)$ is related to the crack sliding displacement $D(x)$ by

$$B(x) = -\frac{dD(x)}{dx} \tag{4.1.9}$$

4.2 Dislocation-based cohesive model (Cohesive-BCS model)

4.2.1 Cohesive model

The central theme of the cohesive theory of fracture is the representation of the fracture process as a gradual separation of the fracture surfaces. This is achieved through the use of numerous functional relationships between the fracture surface traction and the surface displacement. These relationships are called traction-separation laws. In literature, most of the traction-separation laws that have been developed are phenomenological [67]. In this chapter, we also utilize an exponential relationship

(Figure 4.3) between the surface traction and the crack surface displacement [73].

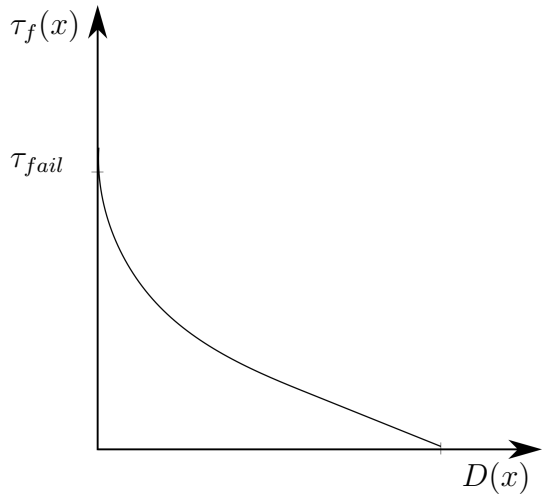

Figure 4.3: Shear exponential traction-separation law

$$\tau_f(x) = \tau_{fail} \exp(-h_s|D(x)|),\ h_s > 0 \tag{4.2.1}$$

h_s in the above equation is a fitting parameter with units of L^{-1}. For monotonic failure, τ_{fail} is the slip system critical resolved shear stress. For fatigue failure, the value of τ_{fail} is lower than the critical resolved shear stress value, and this value is calibrated from experiments. Thus, the area under this curve (Figure 4.3) represents the fracture energy of the slip system.

Putting Eq. (4.2.1) into Eq. (4.1.9) and integrating both sides from c to x gives

$$\ln(\tau_{fail}) - \ln(\tau_f(x)) = h_s \int_x^c B(x)dx,\ a < |x| < c \tag{4.2.2}$$

The assumption used in the above equation is that the value of the stress at the plastic tip is equal to the critical resolved shear stress τ_{fail} of that slip system.

4.2.2 Bounded solution with a cohesive zone

The bounded solution of Eq. (4.1.4) is modified using Eq. (4.2.2), resulting in

$$\ln(\tau_{fail}) - \ln(\tau_f(x)) = h_s \int_x^c \left(-\frac{2\alpha\sqrt{c^2-x^2}}{\pi G} \int_{-c}^{c} \frac{\tau(x')}{(x-x')\sqrt{c^2-x'^2}} dx' \right) dx, \quad a < |x| < c \tag{4.2.3}$$

This equation is a nonlinear Fredholm integro-differential equation of the second kind with a weakly singular kernel. The above expression is simplified using Eqs. (4.1.5) and (4.1.6). The procedure is described in detail in A. The final forms of Eq. (4.2.3) and Eq. (4.1.5) are shown below:

$$\ln(\tau_f(x)) = \frac{2h_s\alpha}{\pi G} \left(\int_a^c \tau_f(x') I_b dx' \right) + \ln(\tau_{fail}),\ a < |x| < c \tag{4.2.4}$$

$$\int_a^c \frac{\tau_f(x)}{\sqrt{c^2-x^2}} dx = \frac{\pi\tau_A}{2} \tag{4.2.5}$$

Here,

$$I_b = \ln\left| \frac{x\sqrt{c^2-x'^2} + x'\sqrt{c^2-x^2}}{x\sqrt{c^2-x'^2} - x'\sqrt{c^2-x^2}} \right| + \ln\left| \frac{\sqrt{c^2-x'^2} + \sqrt{c^2-x^2}}{\sqrt{c^2-x'^2} - \sqrt{c^2-x^2}} \right| - 2\frac{\sqrt{c^2-x^2}}{\sqrt{c^2-x'^2}}$$

These coupled equations (Eqs. (4.2.4) and (4.2.5)) are numerically solved for $\tau_f(x)$ and c using the Newton-Raphson scheme with a piecewise polynomial collocation method [101]. The latter method is described in detail in C.

4.2.3 Unbounded solution with a cohesive zone

Putting Eq. (4.1.7) into Eq. (4.2.2) again gives a nonlinear Fredholm integro-differential equation of the second kind. This expression is simplified using the sym-

metry of the stress function ($\tau(x)$). The final expression becomes

$$\ln(\tau_f(x)) = \frac{2h_s\alpha}{\pi G}\left(\int_a^c \tau_f(x')I_u dx'\right) - \frac{2h_s\alpha\tau_A}{G}\sqrt{c^2-x^2} + \ln(\tau_{fail}), \qquad a < |x| < c \tag{4.2.6}$$

Here, I_u is given by

$$I_u = \ln\left|\frac{x\sqrt{c^2-x'^2}+x'\sqrt{c^2-x^2}}{x\sqrt{c^2-x'^2}-x'\sqrt{c^2-x^2}}\right| + \ln\left|\frac{\sqrt{c^2-x'^2}+\sqrt{c^2-x^2}}{\sqrt{c^2-x'^2}-\sqrt{c^2-x^2}}\right| - 2\left(\frac{\pi}{2} - \arcsin\frac{x}{c}\right)\frac{x'}{\sqrt{c^2-x'^2}}$$

The details of the above simplification is given in B.

There is no analytical method for calculating $\tau_f(x)$ from Eq. (4.2.6) or $S(r_0)$ from Eq. (4.1.8). Thus, we again employ a set of numerical schemes to solve these equations. These numerical schemes are described in C. Once $\tau_f(x)$ is found, the crack sliding displacement $D(x)$ is calculated from Eq. (4.2.1) and $S(r_0)$ is calculated from Eq. (4.1.8). The crack sliding displacement at the crack tip is the crack tip sliding displacement $D(a)$.

4.3 Fatigue crack growth

Under cyclic loading, the applied resolved shear stress τ_A varies between a maximum value τ_{max} and a minimum value τ_{min}. Assuming there is no crack extension between each complete cycle and no crack closure, the monotonic quantities in Eqs.(4.2.4), (4.2.5), and (4.2.6) are converted to cyclic quantities through the following transposition [56, 68, 70]:

$$\begin{aligned} &\tau_A \rightarrow \Delta\tau_A = \tau_{max} - \tau_{min} = (1-R)\tau_{max} \\ &\tau_f(x) \rightarrow 2\tau_f(x) \end{aligned} \tag{4.3.1}$$

Here, R is the load ratio. For a polycrystalline specimen under a far field unaxial cyclic stress $\Delta\sigma$ (shown in Figure 4.4) , the local resolved cyclic shear stress $\Delta\tau_A^i$ on a slip plane i with the Schmid factor m_i is calculated using the Schmid single slip model to be

$$\Delta\tau_A^i = m_i\Delta\sigma = m_i(1-R)\sigma_{max} \tag{4.3.2}$$

where m_i is the local Schmid factor of an active slip system and σ_{max} is the maximum value of the applied stress. The crack growth rate is calculated by assuming that it is proportional to the crack tip sliding displacement. Thus, an equation similar to the Paris law is obtained.

$$\frac{da}{dN} = \lambda D(a)^n \tag{4.3.3}$$

This assumption has been used in numerous analytical fatigue crack growth models [57, 61, 60, 68, 70]. The parameter λ is interpreted as a slip irreversibility factor with values between 0 (completely reversible) and 1 (completely irreversible). The parameter n describes the contributions from different crack displacement modes (I, II, III) on the crack tip sliding displacement $D(a)$.

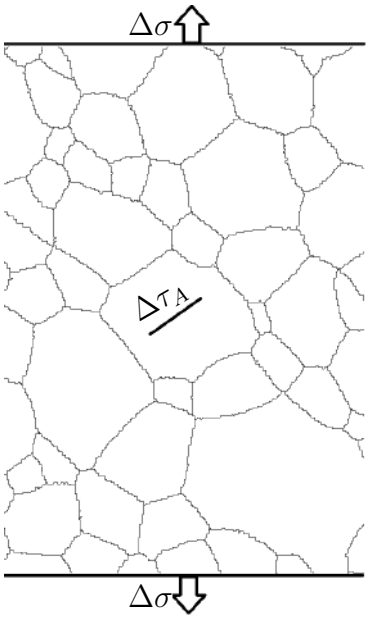

Figure 4.4: Applied cyclic stress $\Delta\sigma$ resolved to a single slip shear stress $\Delta\tau_A$

4.4 Discussion

In this section, we highlight the differences between our Cohesive-BCS model and the BCS and Taira-Tanaka-Nakai models. The first part of the discussion section shows the effect of the cohesive parameter h_s on the dislocation stress and the crack sliding displacement. In the second part of the discussion section, we calibrate our model with data from experiments on Ni-based CMSX-4 alloy. This calibrated model is then used to predict microstructurally short fatigue crack growth across multiple grains in this alloy.

4.4.1 Comparison of the Cohesive-BCS model with the BCS and Taira-Tanaka-Nakai models

In this subsection, we study the impact of the cohesive parameter h_s on the dislocation stress and the crack sliding displacement. Using the values mentioned in Table 4.1, we solve for both the bounded and unbounded solutions of the Cohesive-BCS model (Section 4.2) for different values of parameter h_s. The BCS and Taira-Tanaka-Nakai solutions are also plotted in each figure to highlight the differences.

Variable	Values	Units
$\frac{G}{2\pi(1-\nu)}$	3776	GPa
σ	85	GPa
τ_{fail}	55	GPa
m_s	0.45	

Table 4.1: Material properties for a sensitivity study

In Figure 4.5, we plot the normalized dislocation stress ($\tau(x)/\tau_{fail}$) inside of and in front of the plastic zone. The dislocation stress at the tip of the crack ($x/a = 1$) reduces as we increase h_s. This is expected, as increasing h_s reduces the area under

the traction-separation curve (Figure 4.3), which reduces the fracture energy required to create a crack. This causes a higher number of dislocations to be emitted by the crack tip. Therefore, increasing h_s reduces the dislocation stress. The friction stress at the crack tip ($\tau_f(a)$) reduces as h_s increases, which results in the increased mobility of the dislocations. This increased dislocation mobility causes the length of the plastic zone (c-a) to increase. In Figure 4.5, the half length of the crack and the associated plastic zone c is shown to increase from $2.17a$ for $h_s = 1 \times 10^2\ mm^{-1}$ to $2.53a$ for $h_s = 12 \times 10^2\ mm^{-1}$. As we reduce h_s, the solution given by our model eventually converges to the BCS solution, since the exponential term in Eq. (4.2.1) goes to zero.

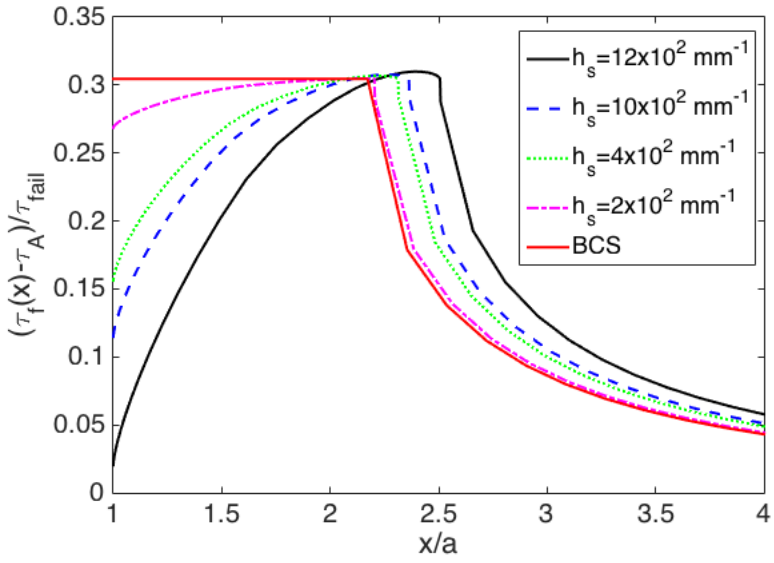

Figure 4.5: The effect of h_s on the dislocation stress when the crack and the associated plastic zone are inside a grain.

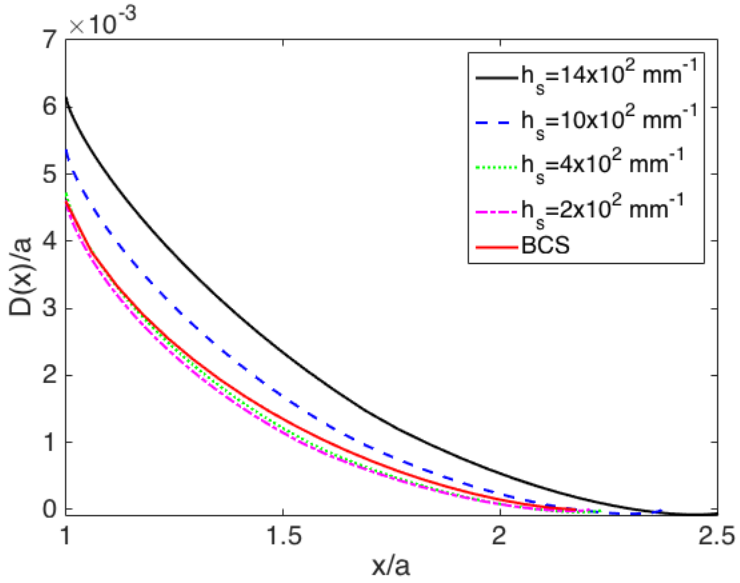

Figure 4.6: The effect of h_s on the crack sliding displacement when the crack and the associated plastic zone are inside a grain.

In Figure 4.6, we plot the normalized crack sliding displacement against the distance from the crack tip ($x = a$) to the plastic tip ($x = c$). As previously stated, increasing h_s increases the number of dislocations that are emitted by the crack tip. This increased dislocation density at the crack tip increases the crack tip sliding displacement ($D(a)$). However, the increase in the number of dislocations also increases the length of the plastic zone ($c-a$). The overall effect of increasing h_s is distributed between the crack sliding displacement and the plastic zone length; therefore, the change in each of these quantities appears less significant than the increase in h_s.

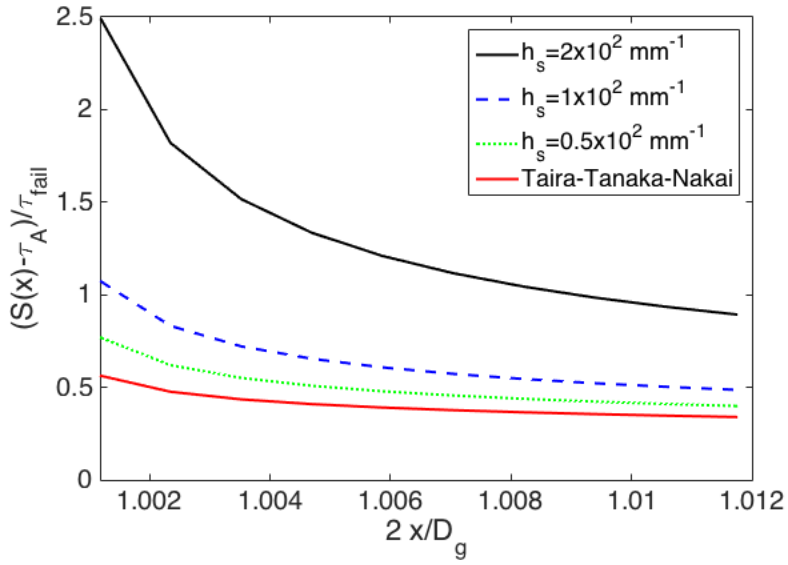

Figure 4.7: The effect of h_s on the dislocation stress when the tip of the crack and the associated plastic zone is at the grain boundary. D_g is the grain size.

In Figure 4.7, the normalized dislocation stress $(S(x) - \tau_A)$ at the grain boundary $(x = c = \frac{D_g}{2})$ is plotted against the distance from the grain boundary in the adjacent grain (see Figure 4.2). The dislocation stress increases as h_s increases. This is due to the increase in the number of dislocations emitted by the crack tip. These increased dislocations pile up at the grain boundary, causing the stress at the grain boundary to increase. Therefore, through the cohesive parameter h_s, we can also control the interaction between the crack plane and the grain boundary.

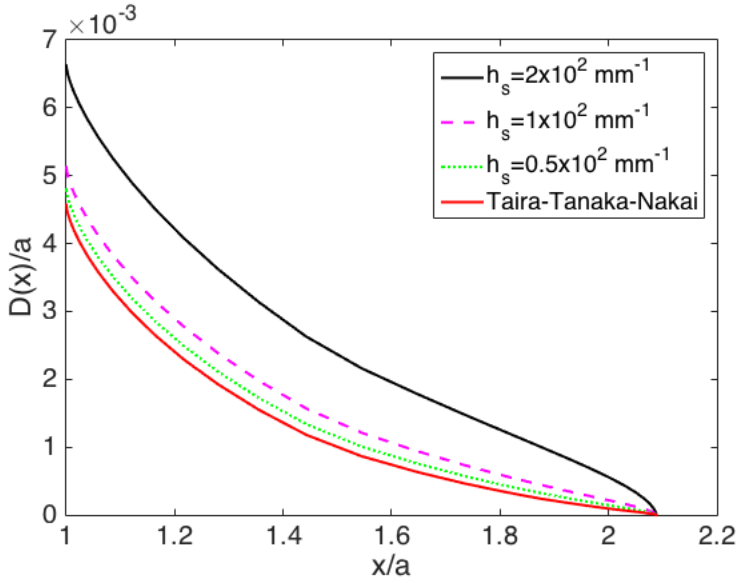

Figure 4.8: The effect of h_s on the crack sliding displacement when the tip of the crack and the associated plastic zone is at the grain boundary

In Figure 4.8, the value of c is constant and is equal to half of the grain size ($\frac{D_g}{2}$). As previously stated, increasing h_s increases the number of dislocations emitted by the crack tip. However, as compared to the case of the plastic zone being within the grain, the impact of increasing h_s is more prominent on the crack sliding displacement.

4.4.2 Microstructurally short fatigue cracks in a Ni-based CMSX-4 alloy

In this subsection, we utilize our Cohesive-BCS model to predict the growth of microstructurally short fatigue cracks in a Ni-based CMSX-4 alloy. To achieve this, we use the experiments performed by Marx et al. [121, 76] and the equations described in Sections 4.2 and 4.3.

Marx et at. performed experiments on a single crystal and polycrystalline modification of a Ni-based CMSX-4 alloy [121]. The material properties of this alloy are given in Table 4.2.

Variable	Value	Unit	Reference
G	72.27	GPa	[123]
ν	0.39		
α	$1-\nu$		
τ_{crss}	363	MPa	[123]
σ_{max}	545	MPa	[121]
R	-0.1		[121]

Table 4.2: Ni-based CMSX-4 alloy material properties

To predict the microstructurally short fatigue crack growth behavior of this alloy, we calibrate the unknown slip system parameters (τ_{fail} and h_s) and the crack growth rate parameter (n) with the experiments. The main difference between our new Cohesive-BCS model (described in Section 4.2) and the BCS model utilized in Marx et al. [76] is the elimination of the slip irreversibility parameter λ. The value of this parameter determines the reversibility of the dislocation emission process at the crack tip [76]. By embedding a cohesive zone in front of the crack tip we can control how many dislocations are emitted from the crack tip. The result of this procedure can be seen in Figures 4.6 and 4.8; at the crack tip ($x/a = 1$), the value of the normalized crack tip sliding displacement ($D(a)/a$) changes with different values of the cohesive parameter h_s.

To calibrate the slip system parameters τ_{fail} and h_s to the experimental results, we use the plastic zone lengths measured from the Marx et al. experiments [121]. The preferred slip system for this FCC alloy is $\{111\} < 110 >$.

In Figure 4.9, the crack and the associated plastic zone lengths were measured for cracks that were sufficiently far from the grain boundary. Here, we utilize Eqs. (4.2.4), (4.2.5), (4.3.1), and (4.3.2) and the material properties mentioned in Table 4.2

to calculate the values of c corresponding to various crack lengths (a). We minimize the error between the experimentally calculated values and the numerically calculated values of c to calibrate the cohesive parameters. Thus, the calibrated values are

$$\tau_{fail} = 261.4\ MPa$$

$$h_s = 10\ mm^{-1}$$

The τ_{fail} value is similar to the BCS model τ_f value (263 MPa) mentioned in Marx et al. [76].

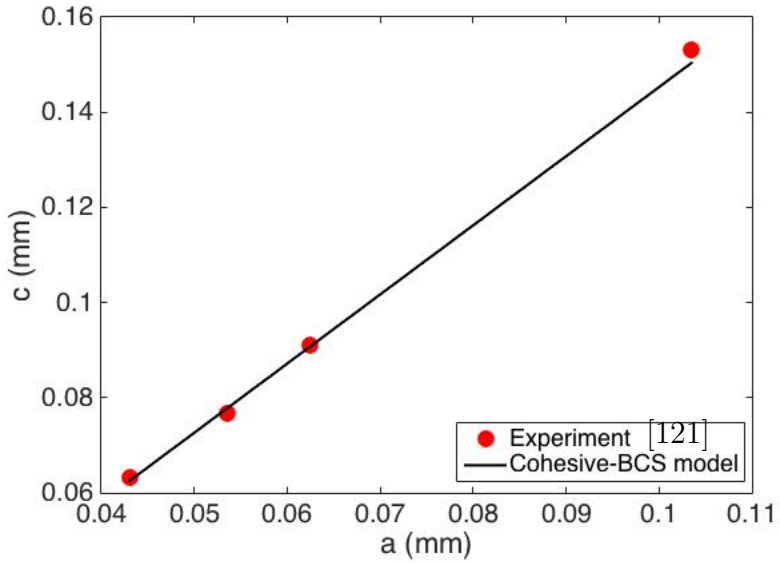

Figure 4.9: Calibration of the cohesive parameters τ_{fail} and h_s from the experiments [121].

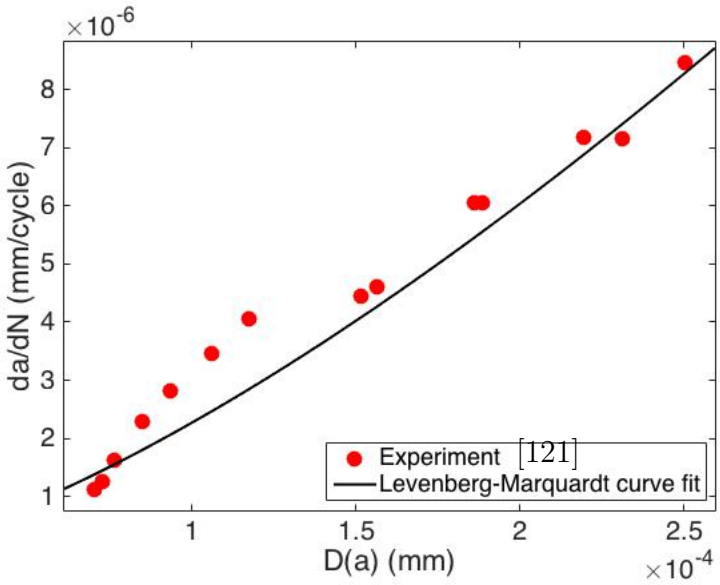

Figure 4.10: Determining the relationship between the crack growth rate and the crack tip sliding displacement ($D(a)$).

The next step in the calibration process is to determine the microstructurally short fatigue crack growth parameter n. This parameter is used to determine the relationship between the crack growth rate and the crack tip sliding displacement. We again solve the equations discussed in Sections 4.2.2 and 4.3 to determine the values of the crack tip sliding displacement ($D(x = a)$) corresponding to each crack length (a). In Figure 4.10, the experimental crack growth rates are plotted against the numerically determined crack tip sliding displacements. The nonlinear least square function in MATLAB [124] is then used to determine the value of the parameter n; $n = 1.411$ is the value that gives the best fit.

All the parameters, τ_{fail}, h_s, and n, have now been determined. We now utilize these parameters to predict the microstructurally short fatigue crack growth rates across multiple grains. The effect of a grain boundary on the crack has to be taken into account in order to understand the crack growth across multiple grains. The presence of a grain boundary can have a significant effect on crack growth. For example, the grain boundary can cause the crack growth rate to reduce or the crack growth to

stop, depending on its features. However, in this chapter, we have not modeled all the features of the grain boundary. As in [121], we use just one parameter, called the grain boundary critical stress intensity factor (ΔK_{gb}), the value of which is mentioned in Table 4.3, to model the effect of the grain boundary. This critical stress intensity factor is the minimum value that the stress in front of the plastic tip has to reach in order to initiate a crack in the adjacent grain.

According to Marx et al. [121], there is only one class of slip system that is active in this FCC alloy ($\{111\} < 110 >$). Thus, the friction stress (τ_{fail}) should be constant for this class of slip system. The applied stress changes from one slip system to another depending on the Schmid factor values. However, as in [121], instead of changing the applied stress across the grains, we use a stress transformation (Eq. (4.4.1)) to change the friction stress value from one grain to another.

$$\tau_{fail}^2 = \frac{1}{2}\sigma(1-R)\big(m_1 - m_2\big) + \tau_{fail} \tag{4.4.1}$$

Here, τ_{fail}^2 is the friction stress in the second grain, which is adjacent to the notched grain.

Variable	Value	Unit	Reference
m_1	0.485		[76]
m_2	0.031		[76]
ΔK_{gb}	3.4	$MPa\sqrt{m}$	[76]

Table 4.3: Schmid factors of the slip planes in the first and second grains for experimental dataset 1.

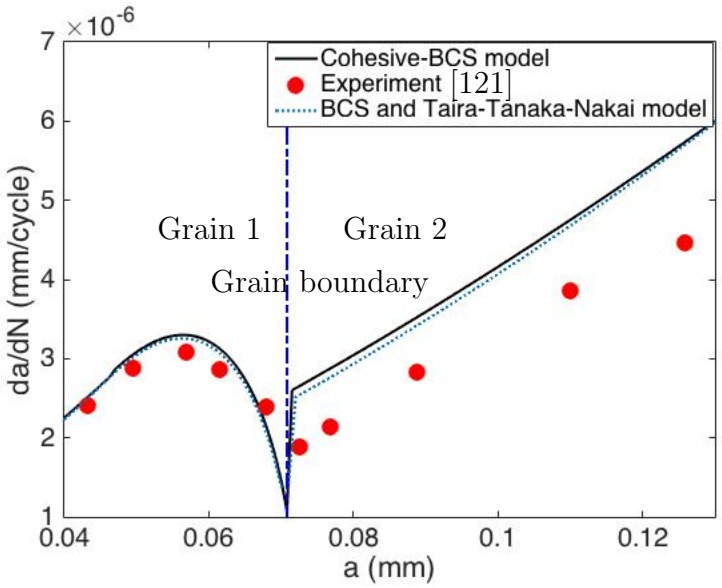

Figure 4.11: Microstructurally short fatigue crack growth across a grain boundary for dataset 1 slip planes as listed in Table 4.3.

In Figure 4.11, we use the calibrated parameters (τ_{fail}, h_s, and n) and the equations mentioned in Sections 4.2 and 4.3 to predict the microstructurally short fatigue crack growth across two grains. The crack initiates at a notch that is 30 μm from the grain boundary. Initially, in Grain 1, the equations derived in Section 4.2.2 are solved to calculate the crack tip sliding displacement. When the plastic zone in front of the crack tip reaches the grain boundary, we use the equations derived in Section 4.2.3 to calculate the crack tip sliding displacement. In Grain 1, when the crack growth rate is at a maximum, the plastic zone has reached the grain boundary. At this point, the crack stress at the plastic tip is lower than the critical stress required to cross the grain boundary. This causes the crack tip sliding displacement to reduce. This is shown in Figure 4.11 by the decline in the crack growth rate as the crack approaches the grain boundary. As the crack tip approaches the grain boundary, the crack stress in front of the plastic tip is increasing due to the increase in the number of the dislocations that are piling up; at some point, it becomes greater than the value of the critical stress determined from the grain boundary critical stress intensity factor (ΔK_{gb}).

This causes the most favorable slip system in Grain 2 to activate and the plastic zone to spread within the grain. In Figure 4.11, we have plotted the results from both the BCS and Taira-Tanaka-Nakai models as well as our Cohesive-BCS model. The values of the parameters used in the BCS and Taira-Tanaka-Nakai models (τ_f, λ, and n) are mentioned in Marx et al. [121].

Variable	Value	Unit	Reference
m_1	0.5		[76]
m_2	0.11		[76]
ΔK_{gb}	3.4	$MPa\sqrt{m}$	[76]

Table 4.4: Schmid factors of the slip planes in the first and second grains for experimental dataset 2.

To show that our model is predictive, we use another set of single crystal Ni-based CMSX-4 alloy experimental data (Table 4.4). We use the same values of the calibrated Cohesive-BCS model parameters (τ_{fail}, h_s, and n). As shown in Figure 4.12, the prediction from our Cohesive-BCS model compares well with the experiments.

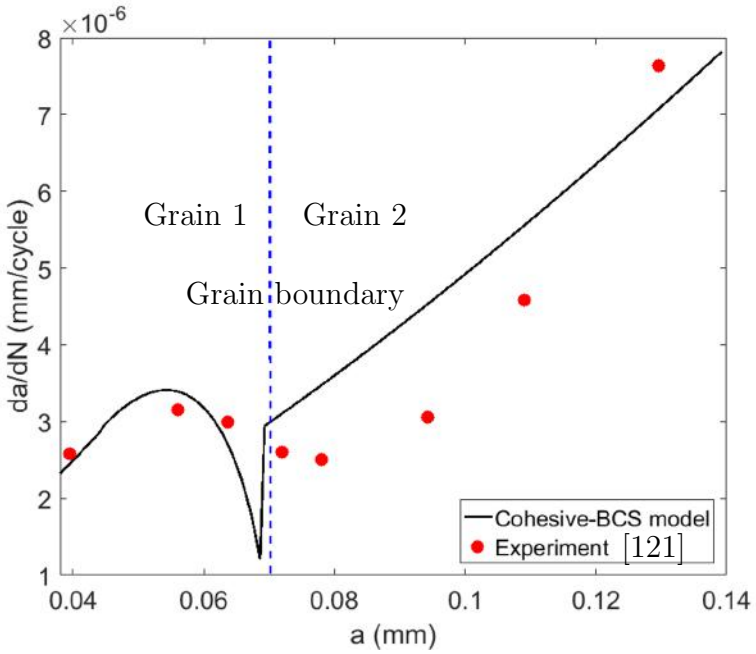

Figure 4.12: Microstructurally short fatigue crack growth across a grain boundary for dataset 2 slip planes as listed in Table 4.4.

Thus, as seen in Figures 4.11 and 4.12, we have replaced the slip irreversibility parameter λ associated with the BCS and Taira-Tanaka-Nakai models with our Cohesive-BCS model parameter h_s and produced similar results for the microstructurally short fatigue crack growth across two grains. The parameter λ (Eq. (4.3.3)) cannot be determined from a lower scale simulation; rather, it is fitted to experimental data obtained from prior works [76]. However, the cohesive parameter h_s can be found from a lower scale simulation. Thus, it can be used to replace the fitting parameter λ from the formulation (Figures 4.11 and 4.12). We would like to emphasize that the exponential cohesive law (Figure 4.3) used in the present model is fully reversible; however, our formulation can also be used in conjunction with irreversible cohesive laws [125, 37]. The addition of the variable λ would improve our fit, but it is not pursued in order to emphasize the effect of the cohesive parameter h_s.

4.5 Conclusion

This chapter outlines the main features of a new dislocation theory-based cohesive model. We have combined the original Bilby-Cottrell-Swinden theory with cohesive theory to simulate microstructurally short fatigue crack growth. The key contribution of this chapter is the ability to incorporate cohesive parameters that are obtainable from lower scale simulations (such as MD) into a higher length scale model based on dislocation interaction with microstructural features. To test the accuracy of our new formulation, we have compared our model with the original formulation and shown that our formulation reduces to the original formulation under a certain condition. We have also utilized our new formulation to predict microstructurally short fatigue crack growth across two grains in a Ni-based CMSX-4 alloy. The advantage of our method over the original formulation is that we have replaced one of the fatigue calibration parameters used in the original formulation with an energy-based cohesive parameter. The computational results show good correlation between the CMSX-4 experimental data and our model. We have also compared the Bilby-Cottrell-Swinden theory results with those of our formulation. Combining the Cohesive-BCS formulation with the variational multiscale method developed in Chapter III should be one of the main priorities for future work in this area.

CHAPTER V

A Phenomenological Crack - Grain Boundary Interaction Model

In this chapter, we present a phenomenological model for simulating the effect of a grain boundary on crack growth along crystallographic planes. This model combines various geometrical features of the interaction between the crack plane and the grain boundary plane. The coupling between the tilt and twist misorientations (which are located between the crack plane and a favorable plane in the next grain, calculated at a grain boundary), the Schmid factor, and the critical crack transmission stress, which is a form of a microscopic stress intensity factor, are incorporated into this model. In Figure 5.1, the loading axis is along the global X direction and the crack grows from slip plane 1 to slip plane 2 across a grain boundary. As shown in the figure, two parameters define the misorientations between the slip plane 1 and slip plane 2. The first parameter is called the tilt misorientation, which is the acute angle between the traces of the slip planes on the sample surface. The second parameter is the twist misorientation, which is the angle between the traces of the slip planes on the GB plane. Thus, the twist misorientation is also dependent on the GB orientation (its tilt and rotation). This model is combined with the Navarro-De Los Rios (N-R) [58] model to predict the crack growth retardation or arrest when the plastic zone is impinging on a grain boundary, while the BCS model [55] is used to predict

crack growth when the plastic zone in front of the crack tip is completely inside a grain. An experimental technique [96] that introduces short fatigue cracks oriented on basal planes in grains with GB misorientations of interest is used to compare the short crack growth rate retardation and arrest predictions from the proposed GB interaction model to the observed experimental data.

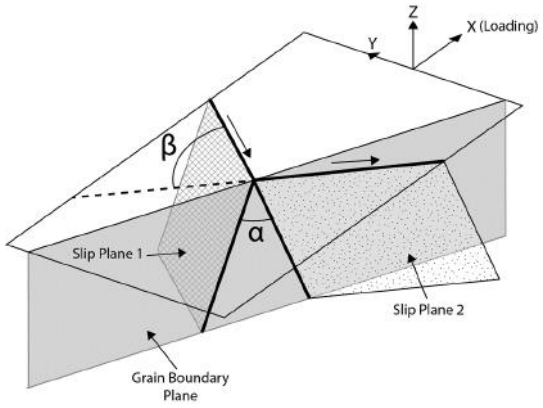

Figure 5.1: Crystallographic mechanism for crack growth from Slip Plane 1 to Slip Plane 2

5.1 Review of existing grain boundary interaction models

Zhai et al. [81] (Figure 5.1) conducted micro-scale experiments to show the effects of the tilt (β) and twist (α) misorientations between the crack plane (Slip Plane 1) and the adjacent grain slip plane (Slip Plane 2) on short fatigue crack growth. They found that the microstructurally short crack growth rate appeared to be influenced by tilt misorientation, twist misorientation, Schmid factors, and other GBs that are interacting with the crack. Wen and Zhai [126] introduced a model that assumes that the resistance offered by the GB due to the twist misorientation is in the form of a Weibull-type function.

Luster and Morris [127] investigated slip transfer across GBs using a geometric

compatibility factor m', defined as

$$m' = \cos\kappa \cos\phi \tag{5.1.1}$$

where κ is defined as the angle between the slip vectors of two adjacent grains and ϕ is the angle between the slip plane normal to those grains. A low value of m' indicates an increased difficulty of slip transfer. The geometric compatibility factor allows for quick investigation of the resistance of the GB; however, it fails to take into account the effect of the GB orientation on the GB barrier strength.

Wilkinson's model [70, 71] incorporates the effects of the adjacent grain orientation and the twist misorientation. The adjacent grain orientation effect is considered using the ratio of the Sachs factor of Slip Plane 1 ($m_{current}$) to the Sachs factor of Slip Plane 2 (m_{next}). The critical stress, $S(r_0)$, is the stress required for a crack to cross a GB. To prevent stress singularities, it is determined at a distance r_0 from the GB in the adjacent grain. It is given by

$$S(r_0) = \frac{m_{next}}{m_{current}}\left[1 + \frac{\alpha}{\alpha_0}\right]\frac{S_{ct}(r_0)}{2} \tag{5.1.2}$$

where S_{ct} is the critical stress required for crack transmission (ct) across a grain boundary without a change in the direction of the crack path, and α_0 is a calibration parameter.

5.2 Proposed combined GB interaction model

Our proposed combined GB interaction model consists of some features of existing GB interaction models with modifications that help us to accurately predict short crack growth retardation and arrest at a GB. Experiments [81] reveal that both the tilt and twist misorientations play a role in slip transmission; thus, we incorporate

features of both the Wilkinson Model (Eq. (5.1.2)) and the Wen and Zhai Model [126]. We assume that the ratio of the Schmid factor of the current grain and that of the next grain, the tilt and twist misorientations, and the critical crack transmission stress directly affect the short crack growth rates. Thus, the critical stress S (the stress required for a crack to cross a GB) at a distance r_0 from the GB is given by,

$$S(r_0) \geqslant f(M)f(\alpha,\beta)f(S_{ct}) \tag{5.2.1}$$

where $f(M) = M_{current}/M_{next}$ and M is the Schmid factor. The form of the tilt and twist misorientation function is more involved since the twist misorientation has a larger effect on crack growth than the tilt misorientation. This effect can be simulated with an exponential distribution as shown:

$$f(\alpha,\beta) = \left[\frac{1-\exp\left(-\left(\frac{1-\cos\beta}{\alpha_1}+\frac{\sin\alpha}{\sin\alpha_2}\right)\right)}{1-\exp\left(-\left(\frac{1}{\alpha_1}\right)\right)}\right] \tag{5.2.2}$$

The numerator of this function is similar to Wen and Zhai Model [126], except that the tilt and twist misorientations are now coupled and a weighting parameter α_1 is applied to scale the effect of twist misorientation in relation to tilt misorientation. The normalization of this function is based on half the maximum value of the tilt misorientation (90°) and the minimum value of the twist misorientation (0°). This is the case for a crack path that is changing from intergranular to transgranular. Krupp et al. [80] have shown a way to calculate the value of $f(S_{ct})$:

$$f(S_{ct}) = \frac{k_l}{M_{current}\sqrt{r_0}} \tag{5.2.3}$$

Here, k_l is a locking parameter from the Hall-Petch relationship for tensile yield strength. The term r_0 is included to prevent a stress singularity, and value between

0.1 and 1 μm is typically used [128]. Thus, Eq. (5.2.1) becomes:

$$S(r_0) \geqslant \frac{k_l}{M_{next}\sqrt{r_0}}\left[\frac{1-\exp\left(-\left(\frac{1-\cos\beta}{\alpha_1}+\frac{\sin\alpha}{\sin\alpha_2}\right)\right)}{1-\exp\left(-\left(\frac{1}{\alpha_1}\right)\right)}\right] \tag{5.2.4}$$

Eq. (5.2.4) is combined with the BCS [55] and the N-R [58] models to predict short crack growth. In these models, the crack growth rate is assumed to be proportional to the crack tip sliding displacement ($\Phi(a)$).

$$\frac{da}{dN} = \lambda\Phi(a)^m \tag{5.2.5}$$

This assumption has been used in numerous analytical short fatigue crack growth models [129, 57, 70, 80]. In our combined GB interaction model, for simplicity, $m = 1$ and λ is calibrated for each material condition. The value of the parameter λ lies between zero and one, which correspond to completely reversible slip and completely irreversible slip, respectively. No attempt has been made to model the crack growth itself; rather, the effectiveness of the proposed combined GB interaction model in capturing crack growth retardation and crack arrest at a GB is presented.

5.3 Details on the experimental procedure

Adams et al. [96] used a wrought rare-earth-containing magnesium alloy, WE43, for the fatigue crack growth experiments. They machined micro-notches that were 100 μm wide and 40 μm deep parallel to basal planes in selected grains to produce crack growth along known crystallographic planes, and to allow for the calculation of tilt and twist misorientations. They selected the locations of micro-notches based on a variety of microstructural factors characterized using EBSD maps of the specimen gage flats. They performed crack growth tests at a frequency of 20 kHz and at a stress ratio of $R = -1$ at room temperature in laboratory air, with a constant

maximum stress of 85 MPa. Dog-bone-shaped thin foil specimens with a nominal thickness of 300 μm were fabricated from underaged WE43 in order to reduce the effect of subsurface microstructure on the interaction between the short fatigue crack growth and the GB. The foil specimens were flat coupons 30.5 mm in total length with a 1.6 mm long and 2 mm wide gage section. An edge notch perpendicular to the tensile axis was produced at the longitudinal center of the gage section of each fatigue specimen by FIB machining. In the foil specimens, the effect of GBs on the crack growth rate was investigated through characterization of both the surface and subsurface microstructures. Further details regarding the experimental techniques can be found in [96, 130].

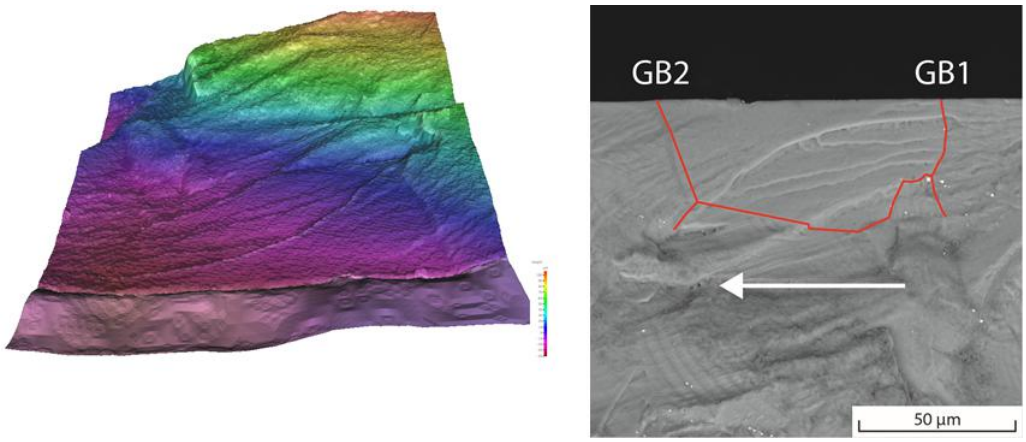

Figure 5.2: Twist misorientation from 3D quantitative fractography [97]

For some GBs, a combination of quantitative fractography and free-surface observation enabled the identification of GB orientation in three dimensions (Figure 5.2). However, in Figure 5.3(b), only surface observation techniques were used to calculate the twist misorientations. In this calculation, rudimentary assumption of GB plane perpendicular to the specimen free surface is used. The accuracy of this assumption is dependent on microstructural features that vary with material, but it is necessary when using a two-dimensional characterization of a three-dimensional process. In Figure 5.4(a), using three-dimensional GB orientation, Adams et al. [96]

calculated twist misorientations, and they found them to be minimally different than those calculated using the perpendicular boundary assumption. Details on two specific cases of fatigue crack growth in cylindrical and thin foil specimens, along with a discussion of the efficacy of the proposed model in describing the observed behavior, are discussed further in the results and discussion section.

5.4 Results and discussion

In this section, the three crack-GB interaction models, described in the previous sections, are compared using the experimental fatigue crack growth rates determined from testing of cylindrical and thin foil specimens. In both types of specimens, the crack growth was predominantly crystallographic in nature. The most significant difference between the thin foil specimens and the cylindrical specimens was a significant reduction in noncrystallographic transgranular crack growth in the thin foil specimens. In the next few paragraphs, the fatigue crack growth rates of two cylindrical specimens are shown along with the combined GB model and Wilkinson's model. Only the experimental crack growth along the basal slip system is selected for the comparison due to large variations in the values of the critical resolved shear stresses for different slip systems in magnesium. In order to make a fair comparison between the three crack-GB interaction models, we use a retardation factor in the last part of this section to show the effect of GBs on the crack growth rate. The retardation factor is evaluated by dividing the lowest crack growth rate observed as the crack approaches the GB (da/dN_{GB}) by the approximate steady state crack growth rate in the grain (da/dN_{ss}). The value of this retardation factor ranges from 0 to 1, with 0 indicating permanent crack arrest and 1 indicating no observed effect of the GB on the crack growth rate.

The material properties and model parameters of WE43 alloy used in this section are shown in Table 5.1

μ	ν	b	α_2 (basal)	λ	r_0	k_l	τ_f (basal)
GPa		($\AA$)	($^\circ$)	$cycle^{-1}$	μm	$MPa\sqrt{mm}$	MPa
17.32	0.27	3.21	45 [126]	0.004	0.1	6.96 [131]	55 [132]

Table 5.1: Magnesium alloy WE43 properties and interaction model parameters

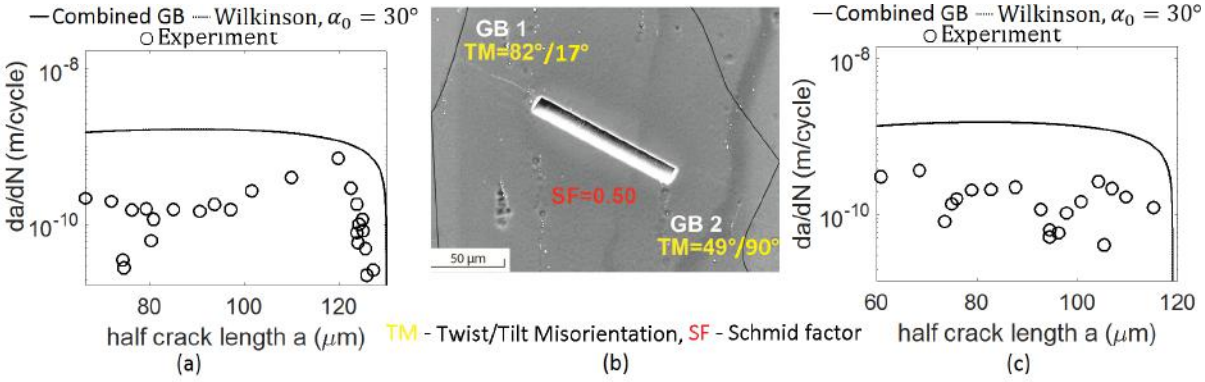

Figure 5.3: GB interaction models (Eqs. (5.1.2), and (5.2.4)) and experimental [96, 130] fatigue crack growth data for an arresting crack on both sides of the notch. (a) Calibration curves representing the crack growth to the left of the notch. (b) SEM image of notch and fatigue crack with tilt (β), twist (α) misorientations, and Schmid factor (SF) values. The grain boundaries are assumed perpendicular to the surface (c) Prediction curves of different GB interaction models representing the crack growth arrest to the right of the notch

In Figure 5.3(b), the notch was placed in a grain with a basal Schmid factor of 0.5. The left end of the notch was located 64 μm, measured along the surface basal trace, from GB 1. The right end of the notch was located 59 μm, measured along the surface basal trace, from GB 2. In Figure 5.3(a), crack growth arrests at GB 1 due to the large twist misorientation, while, in Figure 5.3(c), both the tilt and twist misorientations cause the crack growth to arrest. In Figure 5.3(a), the combined GB interaction model is calibrated by varying α_1 to get the desired fit, resulting in a value of 1.41. This is the minimum value of α_1 that produces crack arrest. The same figure is used to calibrate Wilkinson's model by varying α_0 to get the best fit value of 30°. In Figure 5.3(c), using these calibrated parameters, the combined GB interaction model

(Eq. (5.2.4)) and Wilkinson's model (Eq. (5.1.2)) predict the crack growth arrest event.

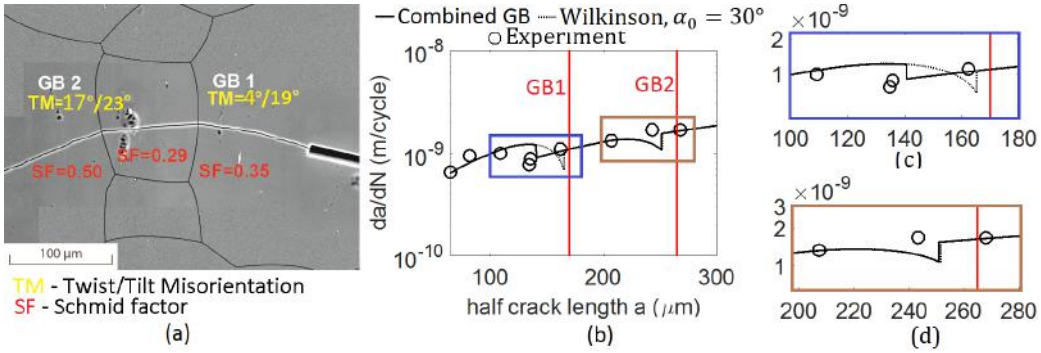

Figure 5.4: Crack growth retardation predictions. (a) SEM image showing crack passing through two GBs with tilt (β), twist (α) misorientations, and Schmid factor (SF) values. The grain boundary angles are calculated by 3D quantitative fractography (Figure 5.2) (b) Crack growth rate predictions with crack deaccelerating at GB 1 and GB 2. (c) Zoomed-in view of crack deacceleration near GB 1. (d) Zoomed-in view near GB 2

In Figure 5.4(a), the notch was placed in a grain with a basal Schmid factor of 0.35. The left edge of the notch was located 111 μm, measured along the surface basal trace, from GB 1. GB 2 was located 95 μm from GB 1. The right edge of the notch was located near a series of finer grains not characterized for misorientation. At GB 1, the crack growth rate slows due to the 19° tilt misorientation, as shown in Figure 5.4(b). The current GB interaction model includes this tilt misorientation and it closely captures the location of this deacceleration, as shown in Figure 5.4(c). Wilkinson's model over-predicts this location.

In Table 5.2, the retardation factors for the cylindrical experiments [130], RF (Exp), are compared with the retardation factors for the combined GB model, RF (Combined GB), and for Wilkinson's model, RF (Wilkinson).

No.	Tilt (°)	Twist (°)	SF1	SF2	D1 (μm)	D2 (μm)	m'	RF (C-GB)	RF (W)	RF (E)
1	17	82	0.5	0.48	260	120	0.12	0	0	0
1	90	49	0.5	0.42	260	80	0.04	0	0	0
2	19	4	0.35	0.29	340	95	0.88	0.82	0.8	0.78
2	23	17	0.35	0.5	95	200	0.85	0.9	0.81	1

Table 5.2: Comparison between the different crack-GB interaction models using cylindrical specimens

In Table 5.3, the retardation factors from the thin foil experiments are compared with those determined from the combined GB model and Wilkinson's model. Looking at Table 5.2, the RF values from the three crack-GB models (the combined GB model, Wilkinson's model, and the m' model) predict the general crack growth retardation trend observed in the experiments. This general crack growth retardation trend is also consistent with the trend of the twist misorientation, with higher twist corresponding to a lower crack growth rate. However, when we look at the thin foil data in Table 5.3, the difference in the crack growth retardation predictions from the three models become clear. If we consider the tilt and twist misorientations separately, their individual effect on crack growth retardation is not clear; however, as compared to the tilt misorientaton, the twist misorientation does has a greater effect on the crack growth retardation. Thus, we might consider the prospect of some unequal coupling between the tilt and twist misorientations. This unequal coupling is representation by our combined GB model. As shown in both tables, there does not appear to be a clear link between the m' parameter and the crack growth retardation. Further, if we consider the unequal coupling between the tilt and twist misorientations, then the m' parameter becomes an inaccurate predictor of the crack retardation and arrest.

No.	Tilt (°)	Twist (°)	SF1	SF2	D1 (μm)	D2 (μm)	m'	RF (C-GB)	RF (W)	RF (E)
1	86	36	0.5	0.49	191	108	0	0.55	0.46	0.67
1	54	51	0.49	0.15	108	359	0.53	0.00	0.00	0.15
2	78	46	0.5	0.28	181	100	0.02	0.10	0.00	0.47

Table 5.3: Comparison between the different crack-GB interaction models using thin foil specimens

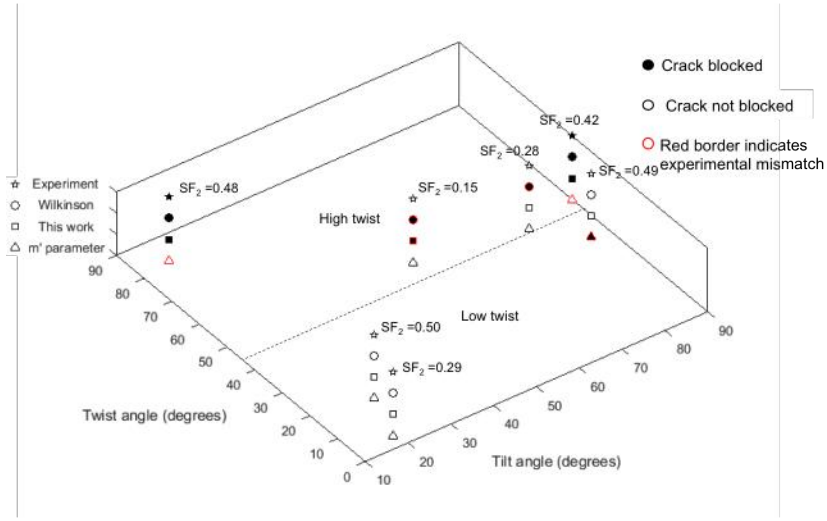

Figure 5.5: Comparison between the different crack-GB interaction models using cylindrical and thin foil specimens

In Figure 5.5, all of the data presented in this paper are plotted with respect to tilt and twist misorientations. Solid points in the figure indicate that the crack growth was blocked at the GB and empty points indicate that the crack growth was either retarded or unaffected by the presence of the GB. The points highlighted in red show the mismatch between the models' prediction and the experiments. The Schmid factors of the second grain for each of the data shown in the tables are also plotted. Few points to be made here are: (1) all models work at low twist and tilt misorientations, where crack is transmitted, (2) m' parameter fails at high twist

misorientation where we expect the crack to get blocked, (3) Wilkinson's model fails at one of the high tilt misorientation cases, and (4) both Wilkinson's model and the present model failed at a midway point of moderate tilt misorientation and moderate twist misorientation where we think the models requires more refinement.

The assumption employed in most of the crack-GB interaction phenomenological models is that all the grains experience the same state of stress. Hence, we restricted our analysis to the use of the Schmid factor to describe the local stress state. Also, we have not taken into account the contributions from the neighboring grains. These neighboring grains may have a strong influence on the local stress state in the cracked grain. In addition, due to the single slip description of our model, we have only compared the basal crack growth retardation and arrest in each of the three models. These are some limitations of our model. However, the main point we would like to convey is that there is a complex coupling between the different crack-GB interaction parameters and that they should all be considered in the prediction of crack growth retardation and arrest.

5.5 Conclusion

In summary, we present a phenomenological model for simulating short fatigue crack growth retardation and arrest at grain boundaries. Unique features of this model include the incorporation of the combined effect of the tilt and twist misorientations into a single exponential function, the use of a Schmid factor to account for loading in the neighboring grain, and the effect of the crack transmission stress. Parameters are calibrated through micro-scale fatigue crack growth experiments from notched samples.

Crack growth experiments in WE43 magnesium exhibit a strong interaction between fatigue cracks and grain boundaries. At grain boundaries with lower values of tilt and twist misorientations, fatigue crack growth rates measured on the sur-

face undergo slight retardation or remain unaffected, while, at grain boundaries with higher twist misorientations, fatigue cracks were arrested. These retardations and arrests can be accounted for using this combined GB interaction model and provide a reasonable basis for extension to 3D crack - grain boundary interactions. These 3D crack - grain boundary interactions are addressed in Chapter VI for a crack front approaching a grain boundary and for a crack front growing through multiple grains.

CHAPTER VI

Dislocation Theory-Based Three-Dimensional Microstructurally Short Fatigue Crack Growth Model

This chapter utilizes the distributed dislocation technique developed by Hills et al. [86] for investigating microstructurally short fatigue crack growth in a magnesium WE43 alloy using micro-beach marks [96]. This technique is based on the concept of equivalent eigenstrains [87] or transformation strains [88]. In general, the three-dimensional (3D) crack problem is converted to a set of two-dimensional (2D) hyper-singular integral equations and solved for either the crack displacements or the strains.

Using ultrasonic fatigue and scanning electron microscopy (UF-SEM) [95], Adams et al. [96] have performed experiments on a magnesium WE43 alloy to allow *in situ* observation of damage accumulation and fatigue crack growth on the microstructural scale. Fractographic investigation of the crack surfaces to examine micro-beach marks on the fracture surfaces has provided greater insights into crack initiation and microstructurally short fatigue crack growth in this alloy. In this chapter, the micro-beach marks on the magnesium WE43 alloy's fracture surfaces are first converted into crack geometries and then approximated by a many-sided polygon with a triangular mesh. The resulting finite domain problem is solved for crack displacements and

stress intensity factors.

This chapter is divided into the following sections. Section 6.1 gives background on representing the crack surface using infinitesimal dislocation loops. In this section, the equations for a planar crack in a half-space and two non-planar cracks in a half-space are developed. In Section 6.2, a numerical scheme to solve the resulting hyper-singular integrals is shown. Section 6.3 provides validation of the model using numerical and analytical results available in literature. Finally, in Section 6.4, we use this method to model two cases of microstructurally short fatigue crack-grain boundary interactions in a magnesium WE43 alloy: the interaction of a crack front growing towards a grain boundary with the grain boundary and the interaction of a crack front spanning across multiple grains with the grain boundary it crosses.

6.1 Background on the distributed dislocation technique

Most of the mechanism-based models described in Chapters 3 and 4 and in [68, 56, 59, 75, 76, 74] are derived from the continuum theory of dislocations by Bilby et al. [55]. Although these 2D models give a good approximation of the microstructurally short crack growth mechanism, most cracks in engineering materials are 3D in character. Thus, in this chapter, we use the distributed dislocation technique developed by Hills et al. [86] based on the concept of strain nuclei to model these cracks. In 3D, this strain nuclei is an infinitesimal dislocation loop containing either a Volterra dislocation [133] or a Somigliana dislocation [134]. As per Eshelby [135], a Volterra dislocation in an elastic body can be constructed as follows [1]: "make a cut over a surface S, which is surrounded by an open or closed curve C (Figure 6.1), and give the upper and lower faces of the cut (S^+ and S^-) a small constant slip or relative displacement, removing material where there would be interpenetration. Fill

[1]Taken from David Anthony Hills, PA Kelly, DN Dai, and AM Korsunsky. *Solution of crack problems: the distributed dislocation technique*, volume 44. Springer Science & Business Media, 2013

in any gaps between the two faces and weld the material together again. The relative displacement vector $\vec{b}$ across the surface S is called Burgers vector and the curve C is the dislocation line. If the Burgers vector is not constant, but varies with position on the surface, a Somigliana dislocation is obtained. If the curve C is an infinite straight line then the 2D models based on Bilby et al. continuum theory of dislocations are obtained. The closed curve C forms a dislocation loop and when the area of this loop becomes infinitely small then it becomes infinitesimal dislocation loop".

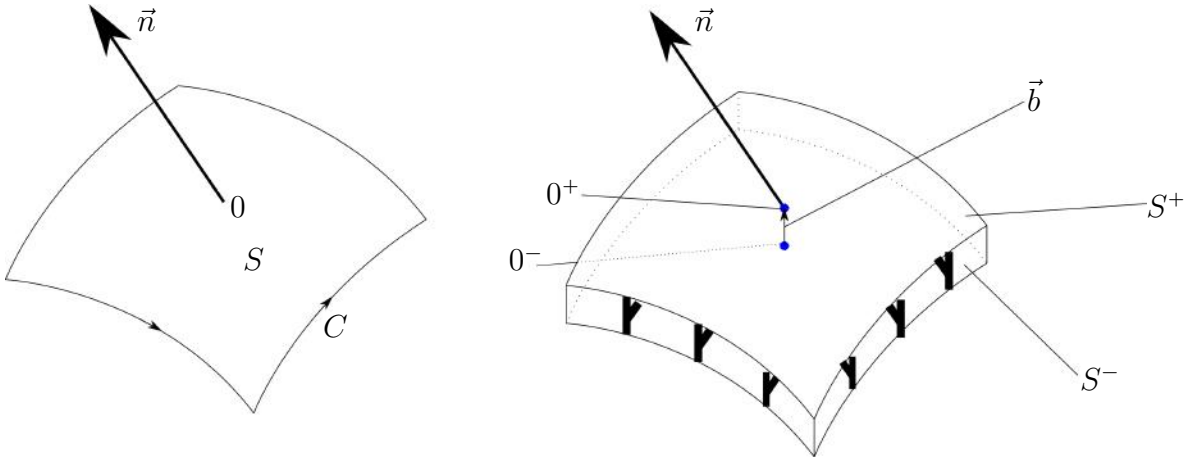

Figure 6.1: A geometrical description of a Volterra dislocation [86]

6.1.1 The distributed dislocation technique applied to a planar crack

As shown in Figure 6.2, the displacement field $u_i(\mathbf{x})$ due to an infinitesimal dislocation loop of area δS with a Burgers vector $\mathbf{b} = (b_1, b_2, b_3)$ on a plane with a normal $\mathbf{n} = (0, 0, 1)$ at a point (x_1, x_2, x_3) is

$$u_i(\mathbf{x}) = D_{ij}(\mathbf{x}, \mathbf{y}) b_j(\mathbf{y}) \delta S, \text{ where } i, j = 1, 2, 3 \tag{6.1.1}$$

The matrix $D_{ij}(\mathbf{x}, \mathbf{y})$ is a tensor function, and, for an infinite domain with a crack in the $X - Y$ plane, it is

$$D_{ij}(\mathbf{x}, \mathbf{y}) = \frac{1}{8\pi(1-\nu)r^3}\left((1-2\nu)(\delta_{ij}r_3 + \delta_{3i}r_j - \delta_{3j}r_i) + 3\frac{r_i r_j r_3}{r^2}\right)$$

where $r_i = x_i - y_i$, $r^2 = r_i r_i$ is the distance from the field point $\mathbf{x}$ to the center $\mathbf{y}$ of the dislocation loop, and δ_{ij} is the Kronecker delta.

For an isotropic material, the stress field is determined by differentiating Eq. (6.1.1) to get the strain field and applying Hooke's law as shown below:

$$\begin{aligned}\sigma_{ij}(\mathbf{x}) &= \mathbb{C}_{ijkl}\frac{\partial u_k(\mathbf{x})}{\partial x_l} \\ &= \mathbb{C}_{ijkl}\frac{\partial D_{km}(\mathbf{x},\mathbf{y})}{\partial x_l} b_m(\mathbf{y})\delta S\end{aligned}$$

where $\mathbb{C}$ is the 4th order elastic tensor.

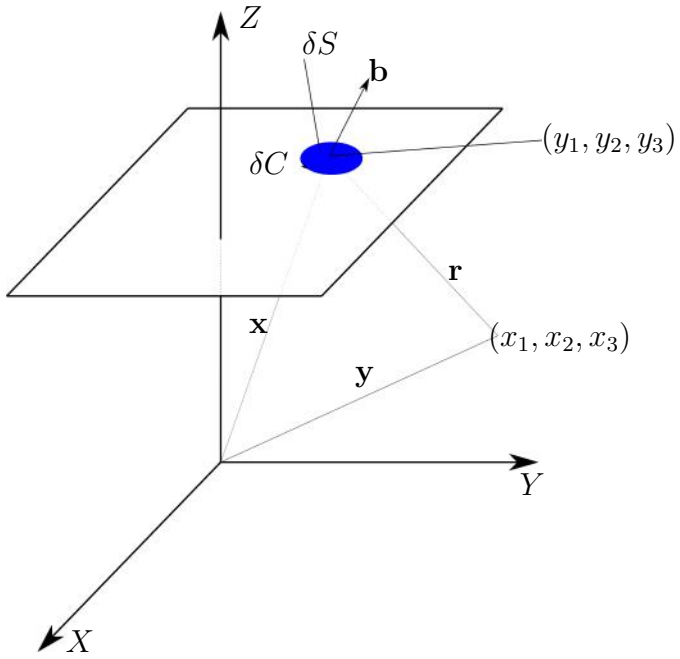

Figure 6.2: An infinitesimal dislocation loop with an arbitrary Burgers vector [86]

The crack plane shown in Figure 6.2 is along the $X - Y$ plane; thus, $r_3 = 0$ and $\sigma_{3i}(\mathbf{x})$ are the only stress components on this crack plane. The stress equation becomes

$$\sigma_{3i}(\mathbf{x}) = K^s_{ij}(\mathbf{x},\mathbf{y}) b_j(\mathbf{y})\delta S \tag{6.1.2}$$

where $K^s_{ij}(\mathbf{x},\mathbf{y})$ is a kernel function that physically represents the tractions induced on the crack plane in an infinite domain due to an infinitesimal dislocation loop of

unit strength and is called fundamental dislocation solution. For an arbitrary oriented plane, the stress equation becomes

$$\sigma_{ij}(\mathbf{x}) = K^s_{ijk}(\mathbf{x}, \mathbf{y}) b_k(\mathbf{y}) \delta S \tag{6.1.3}$$

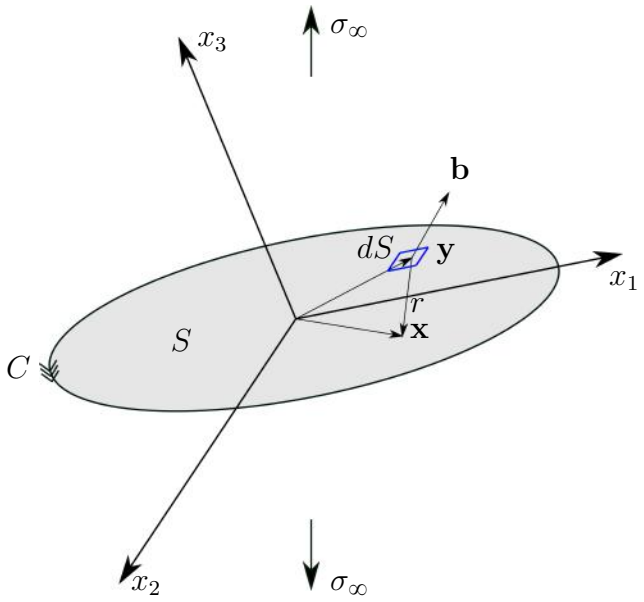

Figure 6.3: A planar crack S modeled by a continuous distribution of infinitesimal dislocation loops with arbitrary Burgers vectors $\mathbf{b}$ [86, 94]

In Figure 6.3, an arbitrarily oriented crack plane S is represented by a continuous distribution of infinitesimal dislocation loops, each of area dS and Burgers vector $\mathbf{b} = (b_1, b_2, b_3)$, to model the three relative displacements of the crack faces. The stress at a point $\mathbf{x}$ on the crack surface due to the dislocation distribution is obtained by integrating Eq. (6.1.3) over the crack faces and applying the far field stress σ^∞ as shown below:

$$\sigma_{ij}(\mathbf{x}) = \sigma^{S,\ dis}_{ij}(\mathbf{x}) + \sigma^\infty_{ij}, \tag{6.1.4}$$

where

$$\sigma^{S,\ dis}_{ij}(\mathbf{x}) = \int_S K^s_{ijk}(\mathbf{x}, \mathbf{y}) b_k(\mathbf{y}) dS$$

and σ^∞_{ij} is the applied stress σ^∞ resolved on the crack surface. For a freely slipping

crack, the boundary condition on the crack surface S becomes

$$\sigma_{3j}(\mathbf{x}) = 0 \ \forall \ \mathbf{x} \in S \tag{6.1.5}$$

In the presence of a plastically yielded region S_p in the front of the crack tip, the above boundary condition changes to

$$\sigma_{3j}(\mathbf{x}) = 0 \ \forall \ \mathbf{x} \in S \tag{6.1.6}$$

$$\sigma_{3j}(\mathbf{x}) = \sigma_y \ \forall \ \mathbf{x} \in S_p \tag{6.1.7}$$

where σ_y is the local yield stress of the material.

Generally, the kernel function is obtained by solving either the governing equations of elasticity theory with the appropriate boundary conditions or the corresponding Green's function. The solution from the Green's function is shown below:

$$K^s_{ijk}(\mathbf{x},\mathbf{y}) = \mathbb{C}_{ijpl}\mathbb{C}_{3kmn}\frac{\partial^2 G_{mp}(\mathbf{x},\mathbf{y})}{\partial x_l \partial y_n} = \mathbb{C}_{3kmn}\frac{\partial T_{ijm}(\mathbf{x},\mathbf{y})}{\partial y_n} \tag{6.1.8}$$

where $G_{mp}(\mathbf{x},\mathbf{y})$ is the Green's function for the geometry under consideration, representing the displacement in the k direction at a point $\mathbf{x}$ due to a unit force in the m direction at a point $\mathbf{y}$, and $T_{ijm}(\mathbf{x},\mathbf{y})$ is the associated stress tensor. For an isotropic material, Eq. (6.1.8) becomes

$$K^s_{ijk}(\mathbf{x},\mathbf{y}) = \mu\left[\frac{\partial T_{ijk}(\mathbf{x},\mathbf{y})}{\partial y_3} + \frac{\partial T_{ij3}(\mathbf{x},\mathbf{y})}{\partial y_k} + \frac{2\nu}{1-2\nu}\frac{\partial T_{ijm}(\mathbf{x},\mathbf{y})}{\partial y_m}\delta_{3k}\right] \tag{6.1.9}$$

where μ is the shear modulus. To account for the presence of finite boundaries, an additional term $K^c_{ijk}(\mathbf{x},\mathbf{y})$ is added, and the kernel function becomes

$$K_{ijk}(\mathbf{x},\mathbf{y}) = K^s_{ijk}(\mathbf{x},\mathbf{y}) + K^c_{ijk}(\mathbf{x},\mathbf{y}) \tag{6.1.10}$$

In the above equation (Eq. (6.1.10)), $K^s_{ijk}(\mathbf{x}, \mathbf{y})$ is the infinite domain hyper-singular kernel obtained using the full-space Green's function in Eq. (6.1.8), and $K^c_{ijk}(\mathbf{x}, \mathbf{y})$ is the half-space correction kernel obtained using the half-space Green's function in Eq. (6.1.8). Explicit expressions for both kernels are given in Appendix D.

6.1.2 The distributed dislocation technique applied to a kinked crack

The problem of a microstructurally short crack crossing a grain boundary and propagating into an arbitrarily oriented slip plane is important. The orientation difference between the crack plane and the slip plane in the next grain can be represented with two misorientations, tilt and twist [81]. The tilt and twist misorientations are calculated at the grain boundary between the crack plane and the favorable slip plane in the next grain. In the previous subsection, the problem of a planar crack was described. In this subsection, we extend the method to model a kinked crack in 3D, therefore only modeling the tilt misorientation.

In Figure 6.4, a crack extending over two surfaces, S_1 and S_2, inclined at an angle to each other, is shown, along with the local coordinate system of the two surfaces.

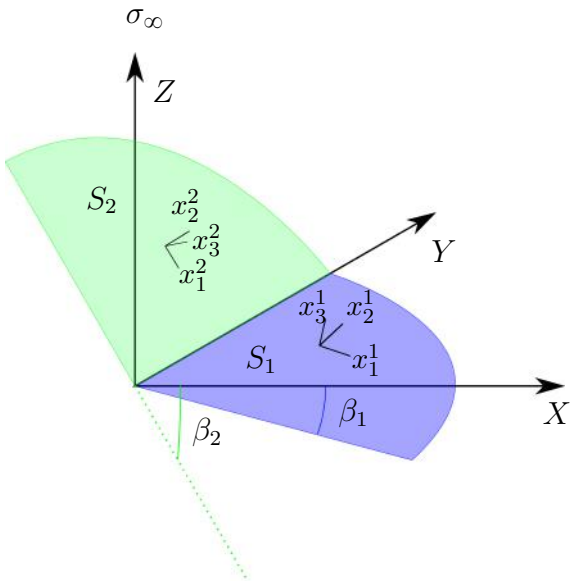

Figure 6.4: A crack extending over two planes inclined with respect to the global X-axis. The free surface is located on the $X-Z$ plane and the Y-axis is pointing inward toward the half-space [94].

The boundary conditions for the two surfaces, S_1 and S_2, in their local coordinate system, are

$$\sigma_{3j}^{(1)}(\mathbf{x}) = 0 \ \forall \ \mathbf{x} \in S_1 \tag{6.1.11}$$

$$\sigma_{3j}^{(2)}(\mathbf{x}) = 0 \ \forall \ \mathbf{x} \in S_2 \tag{6.1.12}$$

Now, consider a point $\mathbf{x}$ on S_1. The total stress at this point consists of the contributions from the dislocation stress in S_1, the dislocation stress in S_2, and the external stress σ_∞. Thus,

$$\sigma_{3j}^{(1)}(\mathbf{x}) = \sigma_{3j}^{(1),\ dis}(\mathbf{x}) + a_{3i}^{(2,1)} a_{jk}^{(2,1)} \sigma_{ik}^{(2),\ dis}(\mathbf{x}) + \sigma_{3j}^{(1),\ \infty}(\mathbf{x}) \tag{6.1.13}$$

where $\sigma_{3j}^{(1),\ dis}(\mathbf{x})$ is the dislocation stress described in Eq. (6.1.4), $a_{jk}^{(2,1)}$ is the 3D transformation matrix that rotates the stress from S_2 to S_1, and $\sigma_{3j}^{(1),\ \infty}(\mathbf{x})$ is the external stress resolved on S_1. A similar equation can be written for the total stress

at a point on S_2. Putting Eq. (6.1.4) into Eq. (6.1.13), we get

$$\sigma_{3j}^{(1)}(\mathbf{x}) = \int_{S_1} K_{3jk}^{(1)}(\mathbf{x},\mathbf{y}) b_k^{(1)}(\mathbf{y}) dS_1 + a_{3i}^{(2,1)} a_{jk}^{(2,1)} \int_{S_2} K_{ikl}^{(2)}(\mathbf{x},\mathbf{y}) b_l^{(2)}(\mathbf{y}) dS_2 + \sigma_{3j}^{(1),\,\infty}(\mathbf{x}) \tag{6.1.14}$$

$$\sigma_{3j}^{(2)}(\mathbf{x}) = \int_{S_2} K_{3jk}^{(2)}(\mathbf{x},\mathbf{y}) b_k^{(2)}(\mathbf{y}) dS_2 + a_{3i}^{(1,2)} a_{jk}^{(1,2)} \int_{S_1} K_{ikl}^{(1)}(\mathbf{x},\mathbf{y}) b_l^{(1)}(\mathbf{y}) dS_1 + \sigma_{3j}^{(2),\,\infty}(\mathbf{x}) \tag{6.1.15}$$

The above equations are coupled and are solved for unknown displacement vectors $\mathbf{b^{(1)}}$ and $\mathbf{b^{(2)}}$, which are in their local coordinate system, by applying the boundary conditions (Eq. (6.1.12)) on S_1 and S_2.

6.1.3 Analytical expressions for the hyper-singular kernel K^s

The kernel function K^s described in the previous subsection is singular with r^{-3} singularity, and the integral exists in Hadamard's finite part (*F.P.*) sense [136]. Dai et al. [137] have provided expressions for solving these integrals by writing the integral in Eq. (6.1.4) as

$$\begin{aligned}\int_S K_{3jk}^s(\mathbf{x},\mathbf{y}) b_k(\mathbf{y}) dS = &\int_S K_{3jk}^s(\mathbf{x},\mathbf{y}) \big[b_k(\mathbf{y}) - b_k(\mathbf{x}) - b_{k,\gamma}(\mathbf{x})(y_\gamma - x_\gamma)\big] dS \\ &+ b_k(\mathbf{x}) \int_S K_{3jk}^s(\mathbf{x},\mathbf{y}) dS + b_{k,\gamma}(\mathbf{x}) \int_S K_{3jk}^s(\mathbf{x},\mathbf{y})(y_\gamma - x_\gamma) dS\end{aligned} \tag{6.1.16}$$

If the relative displacement components b_j at a singular point $\mathbf{x}$ are $C^{1,\alpha}$ ($0 < \alpha \leqslant 1$), then the first integral on the right side of Eq. (6.1.16) is at most weakly singular. This singularity is removable, and the integral is evaluated using Gaussian quadrature. The second integral has the same hyper-singular character as the original integral but with unit displacements, and the third integral has a singularity of order r^{-2}. For an isotropic material, using *F.P.*, the second and third integrals are converted

into regular contour integrals [137] as shown below:

$$F.P.\int_S K^s_{3jk}(\mathbf{x},\mathbf{y})dS = \frac{\mu}{4\pi(1-\nu)}\Big\{[(1-2\nu)\delta_{jk}+2\nu\delta_{3j}\delta_{3k}]L+3\nu\delta_{j\alpha}\delta_{k\beta}L_{\alpha\beta}\Big\} \quad (6.1.17)$$

and

$$F.P.\int_S K^s_{3jk}(\mathbf{x},\mathbf{y})(y_\gamma-x_\gamma)dS = \frac{\mu}{4\pi(1-\nu)}\Big\{[(1-2\nu)\delta_{jk}+2\nu\delta_{3j}\delta_{3k}]M_\gamma+3\nu\delta_{j\alpha}\delta_{k\beta}M_{\alpha\beta\gamma}\Big\} \quad (6.1.18)$$

where L, $L_{\alpha\beta}$, M_γ, and $M_{\alpha\beta\gamma}$ are regular integrals defined over the boundary C of the integration domain S such that

$$L = -\int_0^{2\pi}\frac{1}{r(\theta)}d\theta \quad (6.1.19)$$

$$L_{\alpha\beta} = -\int_0^{2\pi}\frac{\psi_\alpha\psi_\beta}{r(\theta)}d\theta \quad (6.1.20)$$

$$M_\gamma = \int_0^{2\pi}\psi_\gamma \ln r \; d\theta \quad (6.1.21)$$

$$M_{\alpha\beta\gamma} = \int_0^{2\pi}\psi_\alpha\psi_\beta\psi_\gamma \ln r \; d\theta \quad (6.1.22)$$

Here, $\psi_\alpha = (y_\alpha - x_\alpha)/r$ and r is the distance from the singular point (x_1, x_2) to the boundary C of the domain S.

Eqs. (6.1.17) and (6.1.18) hold true for any subdomain of S as long as the singular point $\mathbf{x}$ is located within the subdomain rather than on its boundary. The closed form expressions for Eqs. (6.1.19) – (6.1.22) are given in Appendix E.

6.2 Numerical scheme for solving hyper-singular integral equations

The numerical scheme shown in this section is reproduced from Hills et al. [86]. A non-conforming element is used to represent the discretized domain due to the

following requirements: (1) the derivatives of the relative displacements b_j are continuous at the collocation points (Figure 6.5), and (2) the collocation points are located within the element rather than on the sides so that Eqs. (6.1.17) and (6.1.18) can be employed at the elemental level. We use a piecewise linear approximation to represent the displacements $b(x, y)$ within each element.

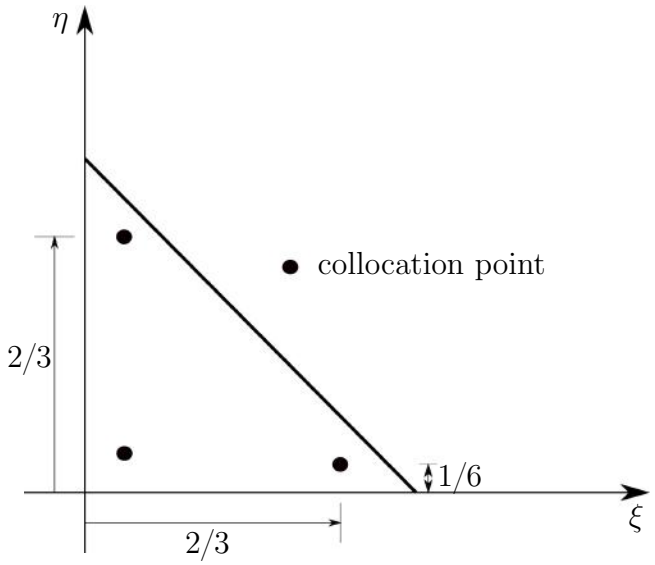

Figure 6.5: A non-conformal triangular element [86]

The crack plane is divided into triangular elements, and the coordinates of an arbitrary point within each element are represented by

$$\begin{aligned} x_1 &= \sum_{q=1}^{n_d} L_q(\xi, \eta) x_1^q \\ x_2 &= \sum_{q=1}^{n_d} L_q(\xi, \eta) x_2^q \end{aligned} \tag{6.2.1}$$

where n_d is the number of nodes associated with an element, $(x_1^q,\ x_2^q)$ are the coordinates of the qth node of the element, and L_q is the shape function defined in the

$\xi - \eta$ coordinate system as

$$L_1(\xi, \eta) = 1 - \xi - \eta$$
$$L_2(\xi, \eta) = \xi$$
$$L_3(\xi, \eta) = \eta$$

where $0 \leqslant \xi \leqslant 1$ and $0 \leqslant \eta \leqslant 1$. The displacement $b(x_1, x_2)$ within each element is represented by a linear interpolation of the shape functions as shown below:

$$b(x_1, x_2) = \sum_{q=1}^{n_c} N_q(\xi, \eta) b_q^e \tag{6.2.2}$$

where $n_c = 3$ is the number of collocation points within the triangular element, b_q^e is the values of the displacement at these collocation points, and $N_q(\xi, \eta)$ is

$$N_1(\xi, \eta) = \frac{1}{3}(5 - 6\xi - 6\eta)$$
$$N_2(\xi, \eta) = \frac{1}{3}(6\xi - 1)$$
$$N_3(\xi, \eta) = \frac{1}{3}(6\eta - 1)$$

As shown in Figure 6.5, the collocation points are located within the triangular element. Thus, the displacement field can be discontinuous across the elemental interfaces. In order to capture the $r^{-0.5}$ singularity of the stress field near the crack front, we use a general form of the crack displacement weight function [138] for elements adjacent to the crack front. The general form of this function is

$$w(x_1, x_2) = \sqrt{2a_0 d(x_1, x_2) - d^2(x_1, x_2)} \tag{6.2.3}$$

where a_0 is a characteristic crack length, which is equal to half the largest distance between any two points on the crack front, and $d(x_1, x_2)$ is the minimum distance from a general integration point (x_1, x_2) to the crack front.

Using Eqs. (6.2.1), (6.2.2), and (6.1.5), we can replace the integral in Eq. (6.1.4) with the following discretized set of equations:

$$\sum_{n=1}^{n_e}\sum_{q=1}^{n_c}\int_{S_n} K_{3ij}(\mathbf{x},\mathbf{y})\ N_q(\mathbf{y})\ dS_n\ b_j^{t(n,q)} = -\sigma_{3i}^{\infty}(\mathbf{x}) \tag{6.2.4}$$

where n_e is the total number of elements, $t = t(n,q)$ is the global point number of the qth collocation point within the nth element, b^t is the value of the displacement at the associated collocation point, and, depending on the problem, K_{3ij} is the full-space or half-space kernel function. Thus, by enforcing Eq. (6.2.4) at the collocation points instead of the whole domain, the discretized set of equations becomes

$$\sum_{t=1}^{n_t} K_{3ij}^{st}\ b_j^t = -\sigma_{3i}^{\infty}(\mathbf{x}^s),\ (s,t = 1,2,...,n_t),\ (i,j = 1,2,3) \tag{6.2.5}$$

where n_t is the total number of collocation points in the domain, $s = s(m,p)$ is the global point number of the pth collocation point within the mth element, $\sigma_{3i}^{\infty}(\mathbf{x}^s)$ is the value of the bulk stress at the collocation point $\mathbf{x}^s$, and K_{3ij}^{st} is given by

$$K_{3ij}^{st} = \int_{S_n} K_{3ij}(\mathbf{x}^s,\mathbf{y})\ N_q(\mathbf{y})\ dS_n \tag{6.2.6}$$

Depending on whether the location of the collocation point $\mathbf{x}^s$ is inside or outside the element under consideration, the matrix elements in Eq. (6.2.6) are calculated using one of two cases. These two cases are addressed in the following subsections.

6.2.1 Case of $m \neq n$

In this case, the integral in Eq. (6.2.6) is regular, as the collocation point $\mathbf{x}^s$ is outside the element under consideration. Thus, we can use 2D Gaussian quadrature

to evaluate the integral as shown below:

$$K_{ij}^{st} = \Delta_n \sum_{k=1}^{n_g} K_{ij}(\mathbf{x}^s, \mathbf{y}^k)\ W_k N_q(\mathbf{y}^k) \tag{6.2.7}$$

where Δ_n is the area of the triangular element S_n, n_g is the total number of Gaussian points, $\mathbf{y}^k$ is the triangular coordinate corresponding to the kth Gaussian point, and W_k is the associated Gaussian weighting factor. For the numerical results to converge fast, the distance between $\mathbf{x}^s$ collocation point and the element S_n center must be larger than $\beta\sqrt{\Delta_n}$, where $\beta = 5$ [138]. If this condition is not met, then the triangle S_n is subdivided into four subtriangles and Eq. (6.2.7) is applied to each one. The sum of the results from each subtriangle gives the K matrix for element S_n.

6.2.2 Case of $m = n$

In this case, the kernel K^s in Eq. (6.2.6) is hyper-singular, as the collocation point $\mathbf{x}^s$ is inside the element under consideration. When applied to a half-space, Eq. (6.1.10) is used in Eq. (6.2.6). Kernel K^c in the resulting equation is a regular function and is evaluated using Gaussian quadrature as described in Subsection 6.2.1. Using Eq. (6.1.16), the hyper-singular integral K^s in Eq. (6.2.6) is split into two parts as shown below:

$$K_{ij}^{st} = K_{ij}^{st,1} + K_{ij}^{st,2} \tag{6.2.8}$$

Comparing Eq. (6.1.16) with Eq. (6.2.8), the first part in Eq. (6.2.8) is

$$K_{ij}^{st,1} = \int_{S_n} K_{ij}^{s}(\mathbf{x}^s, \mathbf{y})\ N_q^1(\mathbf{y})\ dS_n \tag{6.2.9}$$

where

$$N_q^1(\mathbf{y}) = N_q(\mathbf{y}) - N_q(\mathbf{x}^s) - (y_\gamma - x_\gamma^s)\frac{\partial N_q}{\partial y_\gamma}\bigg|_{\mathbf{x}^s} \tag{6.2.10}$$

and the second part in Eq. (6.2.8) is

$$\begin{aligned} K_{ij}^{st,2} =& N_q(\mathbf{x}^s)\ F.P.\int_{S_n} K_{ij}^s(\mathbf{x}^s,\mathbf{y})\ dS_n + \\ &+ \left.\frac{\partial N_q}{\partial y_\gamma}\right|_{\mathbf{x}^s} F.P.\int_{S_n} K_{ij}^s(\mathbf{x}^s,\mathbf{y})(y_\gamma - x_\gamma^s)dS_n \end{aligned} \tag{6.2.11}$$

As shown in Section 6.1.3, the integrals in Eq. (6.2.11) have closed form expressions, and these expressions are given in Appendix E. $N_q(\mathbf{x}^s)$ in the above equations is the value of the shape function at the collocation point $\mathbf{x}^s$.

The integral in Eq. (6.2.9) is weakly singular, and this singularity is removable using a coordinate transformation. Two kinds of coordinate transformation can be employed: a polar coordinate transform or a degenerate coordinate transform. In this chapter, we have used a polar coordinate transformation, because it can produce accurate results even when the shape of the triangular element is distorted such that the collocation point is very close to the side of the element. Thus, we introduce a polar coordinate system with the origin at the collocation point $\mathbf{x}^s$. Eq. (6.2.9) then becomes

$$K_{ij}^{st,1} = \int_0^{2\pi}\int_0^{R(\theta)} K_{ij}^s(\mathbf{x}^s,\mathbf{y})\ \bar{N}_q^1(r,\theta)\ r(\theta)\ dr\ d\theta \tag{6.2.12}$$

where

$$\begin{aligned} \bar{N}_q^1(r,\theta) &= N_q^1(y_1,y_2) \\ y_1 &= x_1^s + r\cos\theta \\ y_2 &= x_2^s + r\sin\theta \end{aligned}$$

and $R(\theta)$ is the distance from the origin to the boundary of the element. The radial integral in the above equation is calculated using one-dimensional Gaussian quadrature, and the circumferential integral is calculated using a simple trapezoidal formula.

Thus, Eq. (6.2.12) becomes

$$K_{ij}^{st,1} = \frac{2\pi}{m_r} \sum_{k=0}^{m_r-1} \sum_{l=1}^{n_{g1}} W_l R(\theta_k) K_{ij}^{s}(\mathbf{x}^s, \mathbf{y}) \; \bar{N}_q^1(\xi_l, \theta_k) r(\xi_l, \theta_k) \tag{6.2.13}$$

where m_r is the number of integration points for the circumferential integral, $\theta_k = 2\pi k/m_r$ is the angular coordinate of the kth integration point, n_{g1} is the number of Gaussian integration points, (ξ_l, θ_k) and W_l are the coordinates of the Gaussian point and its associated weighting factor, respectively, and $r(\xi_l, \theta_k)$ is the distance from the origin to the integration point ξ_l in the direction of angle θ_k.

6.2.3 Determination of relative displacements and stress intensity factors

The relative crack displacements b_i within each crack front element are given by

$$b_i = \frac{4\pi(1-\nu)}{\mu} w(x,y) \sum_{q=1}^{n_c} N_q(\xi,\eta) \bar{b}_i^q \tag{6.2.14}$$

where $\bar{b}_i^q$ are the relative displacements, normalized with respect to the material constant $\mu/4\pi(1-\nu)$, found from Eq. (6.2.4), and $w(x,y)$ is the crack front weight factor from Eq. (6.2.3). The stress intensity factors corresponding to mode I, mode II, and mode III are

$$\begin{aligned}
\frac{K_I}{\sigma^0\sqrt{\pi a_0}} &= 2\pi \sum_{q=1}^{n_c} N_q(\xi,1) \bar{b}_z^q \\
\frac{K_{II}}{\tau^0\sqrt{\pi a_0}} &= 2\pi \sum_{q=1}^{n_c} N_q(\xi,1) (\bar{b}_x^q \cos\theta + \bar{b}_y^q \sin\theta) \\
\frac{K_{III}}{\tau^0\sqrt{\pi a_0}} &= 2\pi(1-\nu) \sum_{q=1}^{n_c} N_q(\xi,1) (-\bar{b}_x^q \sin\theta + \bar{b}_y^q \cos\theta)
\end{aligned} \tag{6.2.15}$$

respectively, where $\cos\theta$ and $\sin\theta$ are the components of the crack front in-plane normal vector on the side of the element where $\eta = 1$, and σ^0 and τ^0 are the normal and shear stresses, respectively, acting on the crack plane.

6.3 Validation of the numerical method

In this section, we validate the numerical method with results from literature. In Table 6.1, we list the values of the numerical parameters that are used to generate the results for this section.

Variable	m	n_{g1}	n_g	β	n_c
Value	100	4	5	5	3

Table 6.1: Numerical parameters

We first present a mesh convergence analysis of a penny-shaped crack in an infinite elastic body subjected to a uniform stress σ_0 perpendicular to the crack plane. Four different meshes used for this analysis are shown in Figure 6.6.

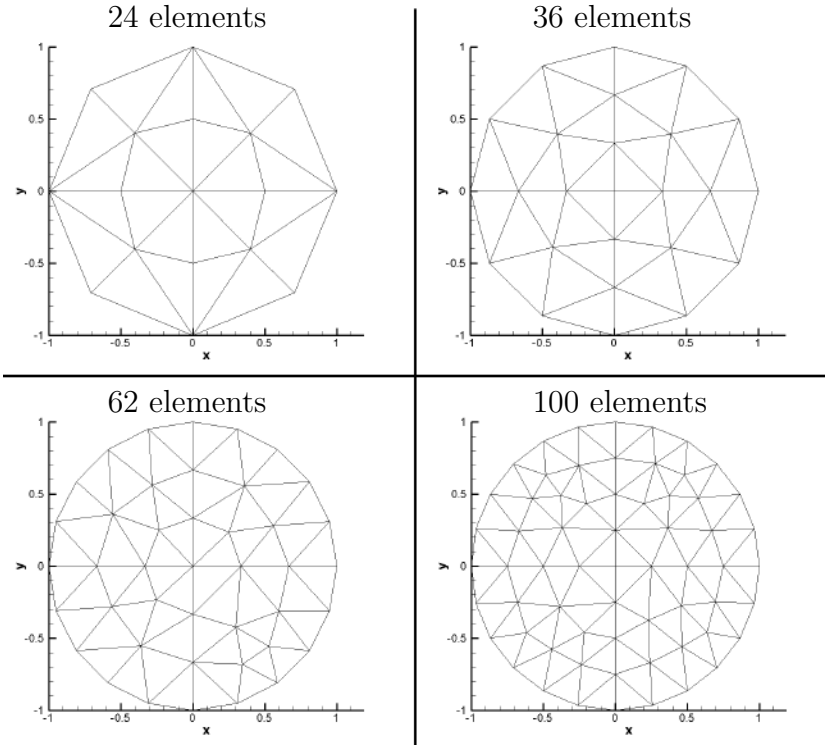

Figure 6.6: Four different meshes for a penny-shaped crack

In Table 6.2, we show the average non-dimensionalized values of mode I stress intensity factors corresponding to each mesh size and the exact analytical value. It can

be seen in this table that the numerical value approaches the exact value as the mesh is refined. For a mesh with 62 elements, the results match accurately with the exact value due to the accurate representation of the displacement field (Eq. (6.2.3)) and the utilization of the closed-form expressions for some of the hyper-singular integrals.

Elements	24	36	62	100	Exact
$K_I/(\sigma^0\sqrt{\pi a_0})$	0.5927	0.6226	0.6319	0.6360	0.6366

Table 6.2: Non-dimensionalized values of mode I stress intensity factor

In the second example, we consider an elliptical crack in an infinite body subjected to a remote uniform tensile stress σ_0 normal to the crack plane and a uniform shear stress τ_0 parallel to the minor axis. This problem has a known analytical solution [139]. In Table 6.3, we show the values of the stress intensity factors for all three modes at the semi-major axis (a) and semi-minor axis (b) of the elliptical crack. These values match closely with the analytical solution.

location	$K_I/(\sigma^0\sqrt{\pi b})$		$K_{II}/(\tau^0\sqrt{\pi b})$		$K_{III}/(\tau^0\sqrt{\pi b})$	
	Present	[139]	Present	[139]	Present	[139]
a	0.622	0.618	0	0	0.457	0.476
b	0.763	0.756	0.876	0.869	0	0

Table 6.3: Stress intensity factors for an elliptical crack ($a/b = 1.5$) in an infinite elastic domain

For our third example, we consider a semi-circular crack in an semi-infinite domain inclined at an angle β to the X_3 axis and subjected to a uniform tensile loading along the X_2 axis (Figure 6.7). This problem has been addressed by many researchers and results are available for different values of inclination angle β. For our case, we use the results published by Murakami et. al. [140] using the body-force method and

Hills et al. [86] using the distributed dislocation technique. In Table 6.4, we show the results for the non-dimensional stress intensity factors at the deepest point on the crack front ($\theta = 90^\circ$) produced by our simulations and those from literature. As can be seen in the table, the results are in agreement with the literature results for $\beta = 0^\circ, 15^\circ, 30^\circ$, and 45°.

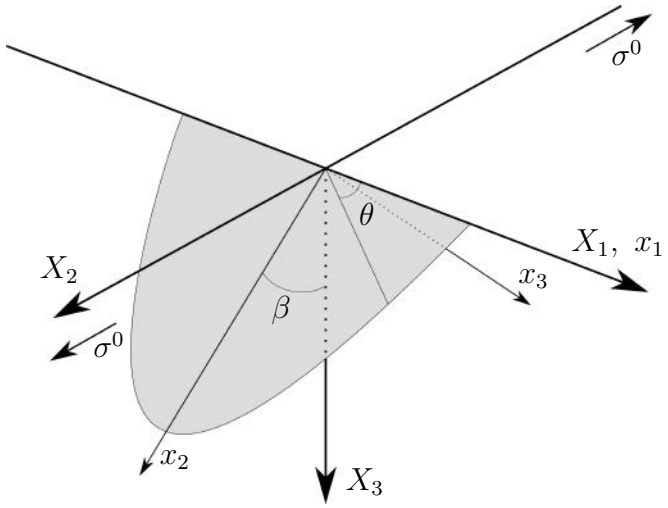

Figure 6.7: An inclined crack plane in an semi-infinite domain ($X_3 > 0$)

$\beta(^\circ)$	$K_I(\theta)/(\sigma^0\sqrt{\pi a_0})$			$K_{II}(\theta)/(\tau^0\sqrt{\pi a_0})$		
	Present	[140]	[86]	Present	[140]	[86]
0	0.653	0.666	0.665	0	0	0
15	0.617	0.626	0.631	0.141	0.147	0.145
30	0.527	0.533	0.537	0.247	0.259	0.255
45	0.400	0.406	0.407	0.294	0.311	0.302

Table 6.4: Stress intensity factors for an inclined semi-circular crack in an elastic half-space ($\theta = 90^\circ$)

Thus, we have successfully validated our model using analytical and numerical results available in literature. In the next section, we will apply our model to understand the effect of grain boundaries on microstructurally short fatigue crack growth.

6.4 Modeling microstructurally short fatigue cracks in magnesium WE43 alloys from micro-beach marks

In this section, we use our numerical method to understand the effect of grain boundaries (GBs) on microstructurally short fatigue crack growth in magnesium WE43 alloys. To aid us in this process, we use the experiments performed by Adams et al. [97]. Adams et al. [96] used different heat treatments on wrought magnesium WE43 alloys to produce three different representative microstructures (T5, T6, and underaged). During their ultrasonic fatigue experiments, they found that, for tests conducted in air, regions of the fatigue fracture surfaces were often marked with microscopic indicators of crack advancement that they termed micro-beach marks. These micro-beach marks correlated directly with the cyclic loading history of the tests, where the distance between markings was proportional to the number of cycles in a given block of the load history. Thus, the local crack growth rates can be calculated based on the assumption that each ultrasonic pulse (4000 cycles) directly corresponds to one micro-beach mark. Additional details on micro-beach marks and representative microstructures are given in [96].

We use the experimental results from T6 specimens (average grain size of $112 \pm 55\ \mu m$) and underaged specimens (average grain size of $114 \pm 58\ \mu m$) for our model. The material properties and the loading condition used in this section are given in Table 6.5.

Variable	μ	ν	σ_{max}	σ_y (basal)	$R = \frac{\sigma_{min}}{\sigma_{max}}$
Value	17 GPa	0.27	85 MPa	55 MPa	-1

Table 6.5: Material properties of magnesium WE43 alloys [132] and ultrasonic fatigue loading condition [96]

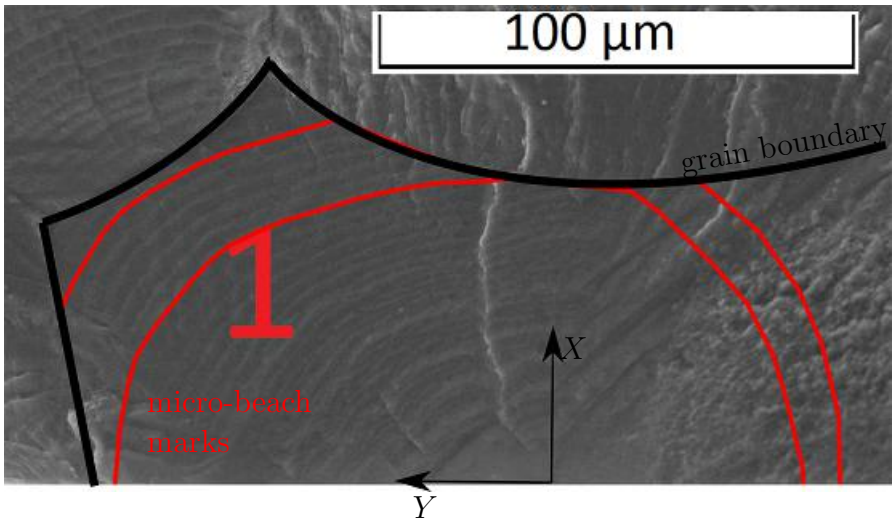

Figure 6.8: Microscopic progression marks (micro-beach marks) on T6 fracture facet 1 as a result of ultrasonic fatigue loading [97]

Figure 6.8 shows a scanning electron micrograph containing a natural crack initiation site on T6 fracture facet 1. The micro-beach marks emanating from this site to the grain boundary (black curve) can also be seen. The local crack growth rates on this facet are obtained from the micro-beach marks. For our study, we extract all the micro-beach marks between and including the two red marks. We used these micro-beach marks to construct the crack plane geometries using NIH's ImageJ [116] code. In some places, these micro-beach marks were not visible and an extrapolation method was used to connect the missing region of the curve. The crack geometries extracted from this code are rotated to get the correct crack plane orientation with respect to the experimental frame ($X,\ Y,\ Z$).

In Table 6.6, the orientation of fracture facet 1's normal and the angle that the normal makes with the basal slip plane are shown.

Facet	n_X	n_Y	n_Z	Angle with basal slip plane
1	0.3107	0.2013	0.9289	12.2°

Table 6.6: Orientation of fracture facet 1 on a T6 specimen [97]

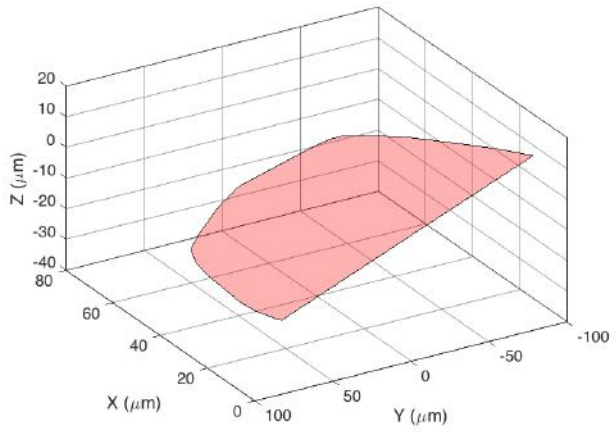

Figure 6.9: Crack plane extracted from one of the micro-beach marks and rotated to represent the correct plane orientation with respect to the experimental frame

In Figure 6.9, a crack geometry extracted from one of the micro-beach marks is shown with the correct orientation with respect to the specimen axes. The loading on the crack surface is along the Z-axis. Thus, in our analysis, we consider both mode I and mode II fatigue failure modes. For all the plots presented next, each crack front increment, which represents 4000 loading cycles, is represented by a set of 60 points, and the color distribution of these points represents the value of that parameter in that increment.

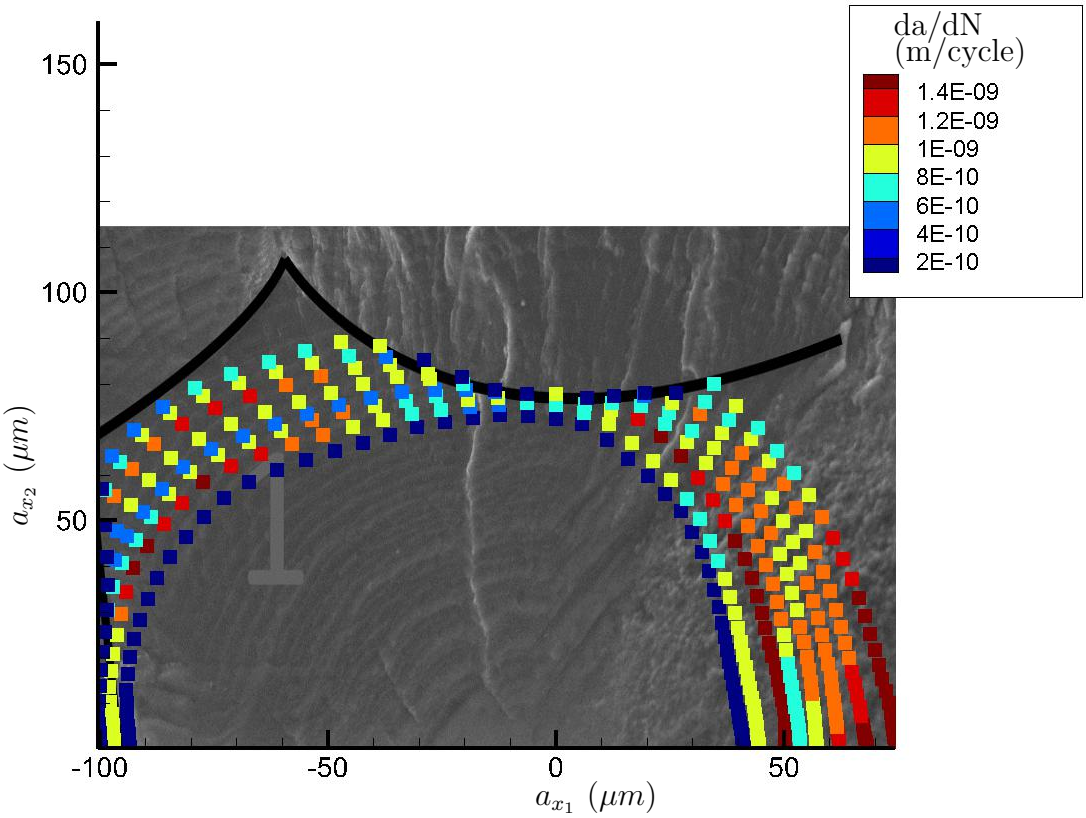

Figure 6.10: Crack growth rates along the crack front as it moves toward the grain boundary

In Figure 6.10, the in-plane crack growth rates are plotted as a function of the crack length a. In the figure, a_{x_1} and a_{x_2} are the components of a in the local coordinate system (x_1, x_2, x_3) of the crack. The micrograph of the specimen is underlaid to show the location of the grain boundary, and it is not a correct representation of the orientation of the fracture facet. The crack growth rates are shown with respect to the first crack front increment. As expected, initially, the crack growth rate increases for the entirety of the crack front increment; then, it slows down for the points that are nearing the grain boundary, while it keeps increasing for the points located further away from the grain boundary. To quantify this trend, we first use the analytical expression of the macro-scale mode I stress intensity factor.

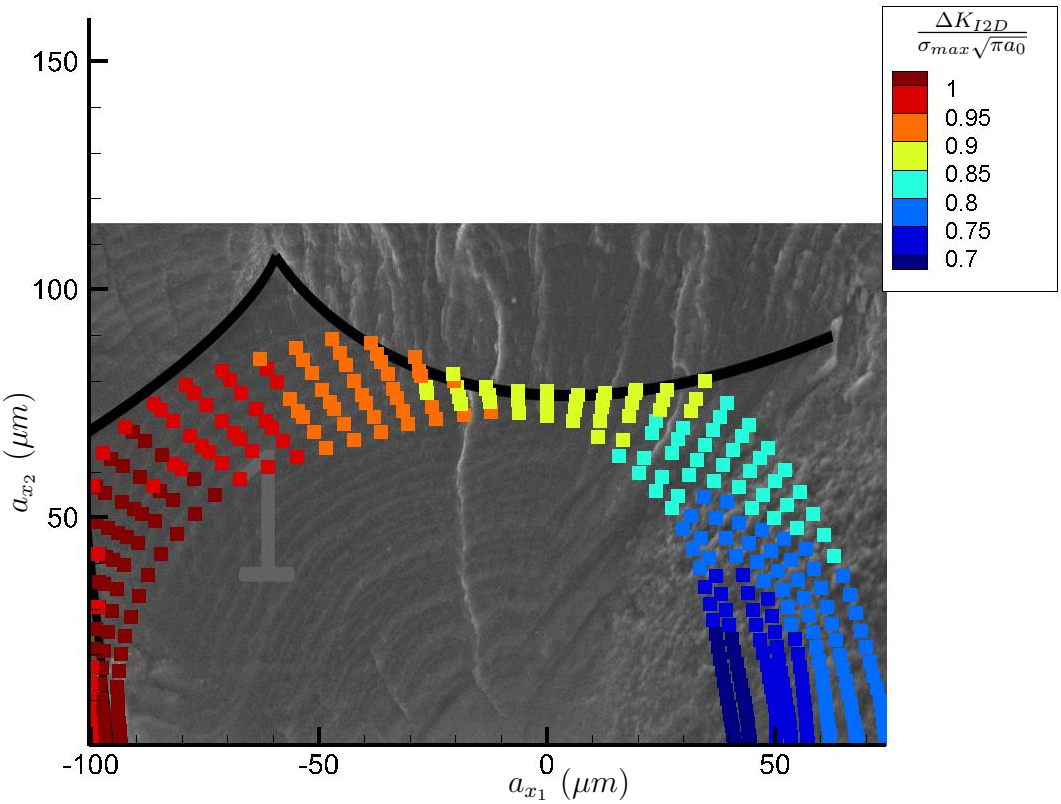

Figure 6.11: Range of the mode I stress intensity factors (ΔK_{I2D}) along the crack front as it moves toward the grain boundary

In Figure 6.11, we show the distribution of the range of the macro-scale mode I stress intensity factor along the crack front as it grows toward the grain boundary. The stress intensity factor values are non-dimensionalized by the mode I stress intensity factor for the infinite plate ($\sigma_{max}\sqrt{\pi a_0}$). For each crack front increment, the infinite plate stress intensity factor has a characteristic crack length a_0, and this length is equal to half the largest distance between any two points on that increment. As shown in the figure, the stress intensity factor increases with an increase in the crack length. However, as shown in Figure 6.10, the crack growth rate trend is much more complex due to the presence of the grain boundary.

For a microstructurally short crack, the local microstructure plays an important role in the fatigue behavior of the material. Thus, for the correct representation of the mechanisms happening at the crack front, microstructural barriers, such as grain

boundaries and precipitates, have to be taken into consideration. In the rest of this section, we show two approaches to model the effect of the grain boundary on the fatigue crack growth rates.

In the first approach, the crack tip displacement is used to quantify the trend of the crack growth rate. Before implementing the model, we make the following assumptions: (1) all the grains in the microstructure experience the same state of stress, (2) for all the extracted crack front increments, the plastic zone extends to the grain boundary, (3) the local yield stress of the material in this plane is the same as that of the basal slip plane, and (4) all three failure modes experience the same local yield stress. Utilizing the first assumption, we determine the external stress acting on the crack plane by a simple stress transformation. Using the second assumption, we model the profile of the plastic zone in front of the crack tip using the grain geometry (shown with a black outline in Figure 6.8). The third and fourth assumptions allow us to use Eq. (6.1.4) with boundary conditions described by Eq. (6.1.7) to determine the crack displacements (the crack tip opening displacement and the crack tip sliding displacement).

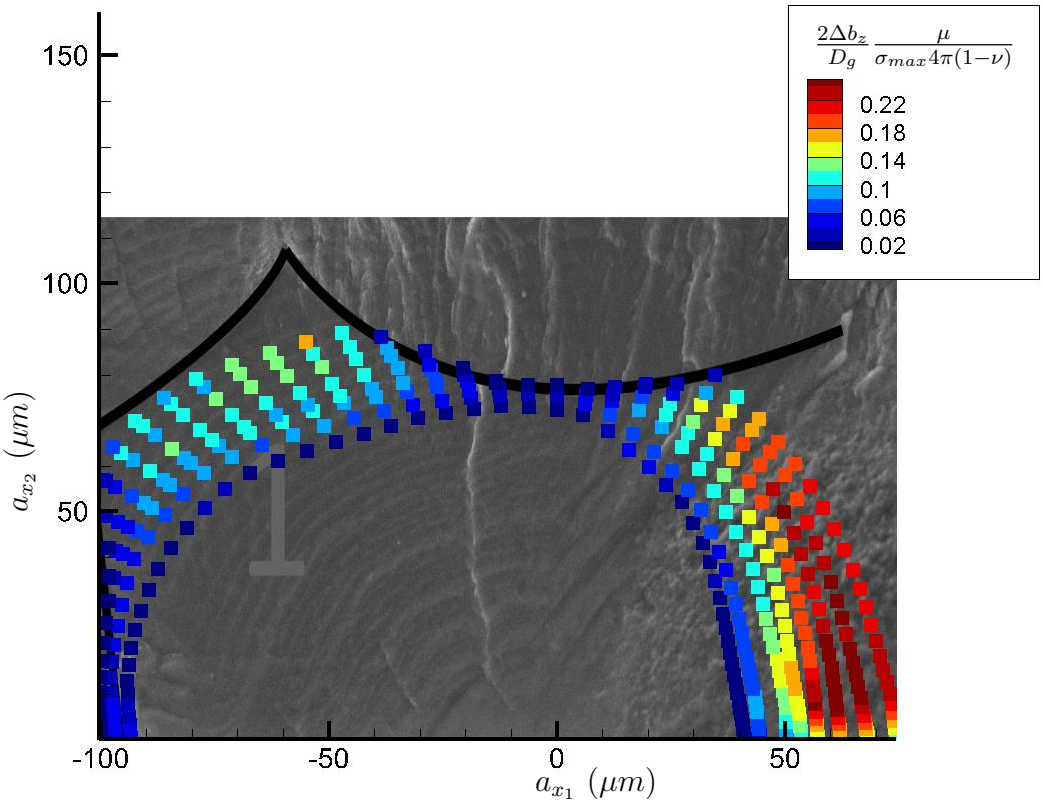

Figure 6.12: Range of the crack tip opening displacements (Δb_z) along the crack front as it moves toward the grain boundary

In Figure 6.12, we show the range of the crack tip opening displacement along the crack front as it moves toward the grain boundary. The displacement values are normalized by the material constant $\mu/(4\pi(1-\nu))$ and non-dimensionalized by half of the value of the grain size D_g. For each of the crack front increments, the plastic zone in the front of the crack tip extends to the grain boundary. Thus, we are able to capture the effect of the grain boundary on the crack tip opening displacement. Initially, when the crack front grows, the value of the crack tip opening displacement increases for all the points along the crack front. However, after the third crack front increment, the crack tip opening displacements of the points closer to the grain boundary starts to reduce. For the points farther away from the grain boundary, the crack tip opening displacements show an increasing trend as the crack front grows.

This trend is consistent with the general trend of the crack growth rates from Figure 6.10. A similar trend is seen in a plot of the range of the crack tip sliding displacement (Figure 6.13).

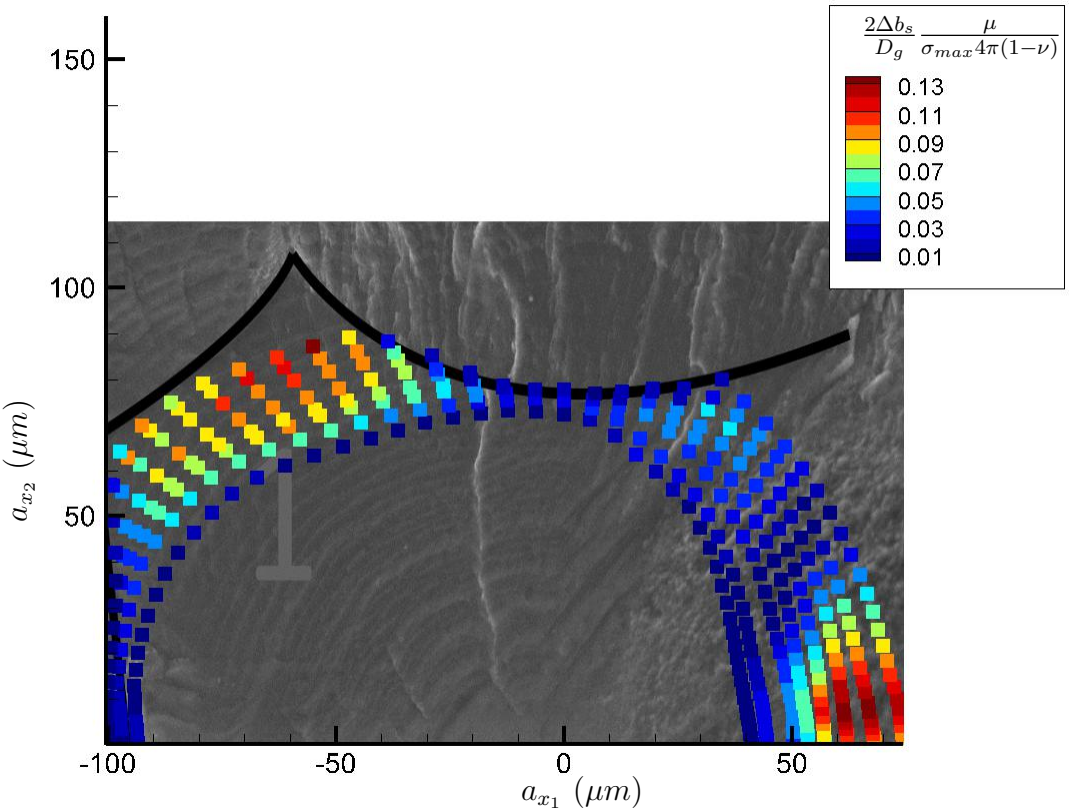

Figure 6.13: Range of the crack tip sliding displacements (Δb_s) along the crack front as it moves toward the grain boundary

For the second approach, we use the micro-beach marks from the scanning electron micrograph of an underaged specimen [97]. As shown in Figure 6.14, these micro-beach marks span across two fracture facets (labeled 1 and 2 in the figure) that are arbitrarily oriented in the microstructure. For our simulation, we use all the micro-beach marks between and including the two red marks shown in the figure.

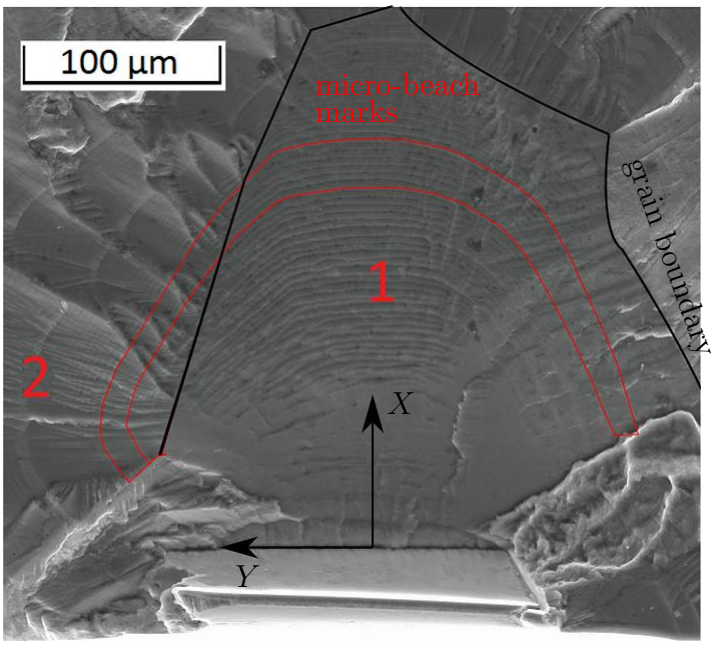

Figure 6.14: Microscopic progression marks (micro-beach marks) on two fracture facets (1 and 2) as a result of ultrasonic fatigue loading on an underaged specimen [97]

In Table 6.7, the orientations of these two fracture facets are shown. Looking at the table, these facets have very similar values of n_X. Thus, we can assume that only a tilt misorientation exists between the two facets at the grain boundary. This allows us to use the equations described in Subsection 6.1.2 for modeling the growth of the kinked crack across a grain boundary.

Facet	n_X	n_Y	n_Z
1	−0.2533	−0.0685	0.9650
2	−0.2468	−0.1490	0.9575

Table 6.7: Orientations of the two fracture facets on an underaged specimen [97]

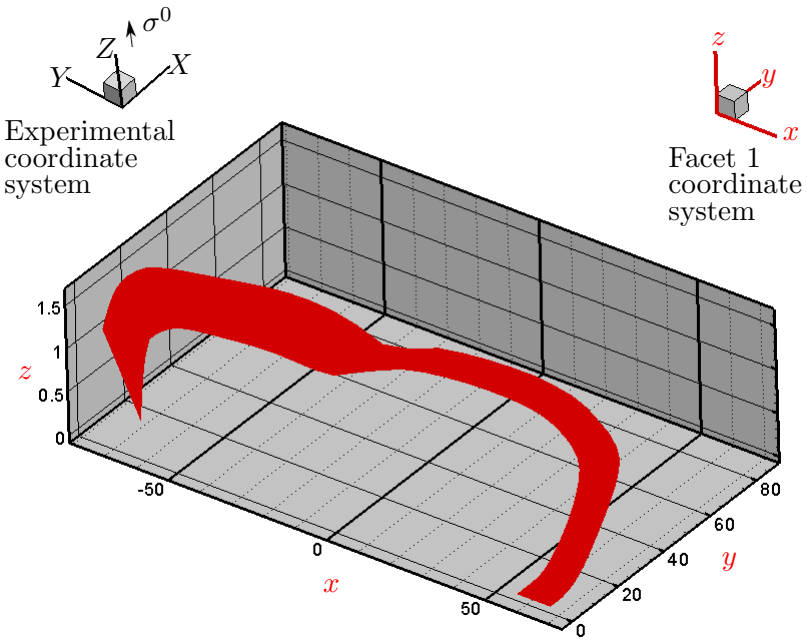

Figure 6.15: Facets 1 and 2 are plotted with respect to the coordinate system of facet 1 (x, y, z). The experimental coordinate system (X, Y, Z) is also shown with the loading σ^0 applied along the Z-axis.

In Figure 6.15, we plot the two facets with respect to the facet 1 local coordinate system to show the orientation of the facets with respect to each other. Also visible in the same plot is the experimental coordinate system (X, Y, Z). The loading σ^0 is applied along the experimental Z-axis. Thus, the facets will experience all three failure modes.

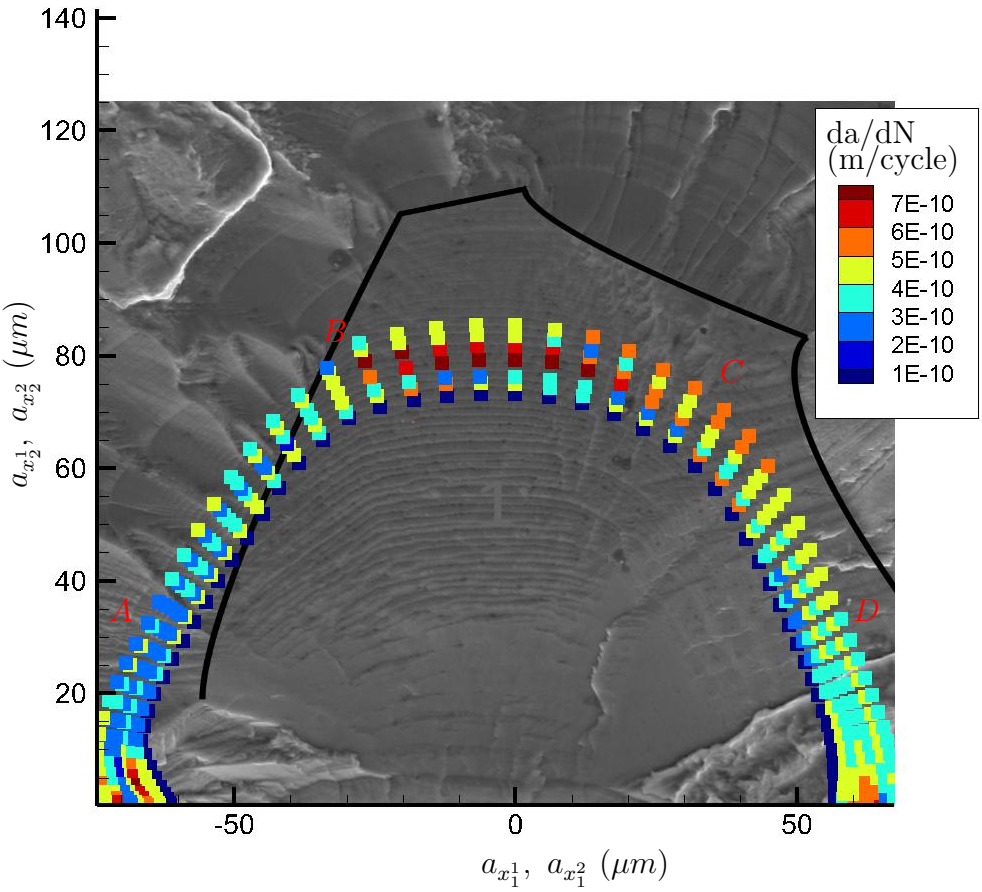

Figure 6.16: Crack growth rates along the crack front increments calculated from micro-beach marks in an underaged specimen

In Figure 6.16, we plot the in-plane crack growth rates across the two facets. Thus, the crack growth rates on facet 1 are plotted as a function of the crack length along the first facet, and the crack growth rates on facet 2 are plotted as a function of the crack length along the second facet. In the figure, $a_{x_1^1}$ and $a_{x_2^1}$ are the components of the crack length in the facet 1 local coordinate system, and $a_{x_1^2}$ and $a_{x_2^2}$ are the components of the crack length in the facet 2 local coordinate system. Both of the local coordinate systems have the same origin. Again, we underlay the micrograph to show the location of the grain boundary. We select four locations labelled A, B, C, and D on the micrograph to compare trends in the crack growth rates and other parameters introduced later. These locations are shown in Figure 6.16. Near location

A, the crack growth rate reduces as the crack front grows towards this location. This retardation may be due to the proximity of the crack front to the grain boundary; the crack front increments at this location are within 10 μm of the grain boundary. Near location B, we can clearly see the retardation in the crack growth rates as the crack front crosses the grain boundary. Near location C, the average crack growth rate over the entire portion of the crack front appears to increase as the crack front advances toward the grain boundary, and, near location D, the crack growth rates over the last three crack front increments are either constant or decreasing.

To incorporate the effect of the grain boundary into our model, we use a function f_g as shown below:

$$f_g(\mathbf{x}) = 1 - P_{gb1} \exp(-\frac{d(\mathbf{x})}{P_{gb2}}) \tag{6.4.1}$$

where P_{gb1} and P_{gb2} are the calibration parameters ,and $d(\mathbf{x})$ is the minimum distance of the point $\mathbf{x}$ from the nearest grain boundary. The applied stresses in Eqs. (6.1.14) and (6.1.15) are multiplied by this function to simulate the retardation effect of the grain boundary on the microstructurally short fatigue crack growth. The parameters P_{gb1} and P_{gb2} are chosen as 0.8 and 10 μm, respectively. The first parameter allows us to model the retardation effect of the grain boundary; therefore, when the crack front reaches the grain boundary, the applied stress reduces to 20% of its value. The second parameter identifies a region of 10 μm on both sides of the grain boundary in which the grain boundary retardation effect is strong.

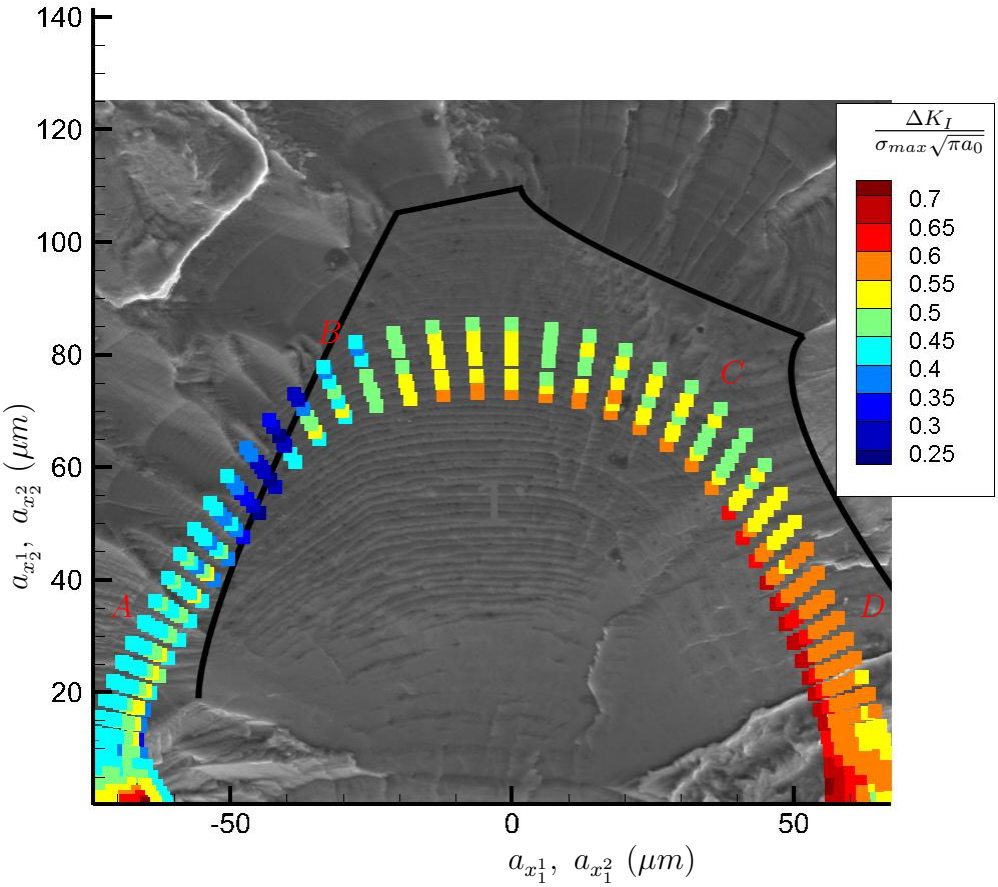

Figure 6.17: Range of the mode I stress intensity factors (ΔK_I) along the crack front increments

In Figure 6.17, we show the plot of the range of the mode I stress intensity factor along the crack front increments as the crack front grows on two facets. Again, the values are normalized by the mode I stress intensity factors of the infinite plate. The mode I stress intensity factor values near location A show a general decreasing trend, similar to the one seen in the crack growth rates (Figure 6.16). Near location B, we can clearly see the grain boundary retardation effect as the crack front crosses the grain boundary. Thus, assuming the Paris Law is applicable, the function described in Eq. (6.4.1) is able to model the retardation effect of the grain boundary on the crack growth rate. However, near location C, the values of the stress intensity factor over the crack front increments show a complex trend that may or may not match the crack growth rate trend. Near location D, we can see the retardation effect of the

grain boundary, similar to the trend seen in the crack growth rate plot.

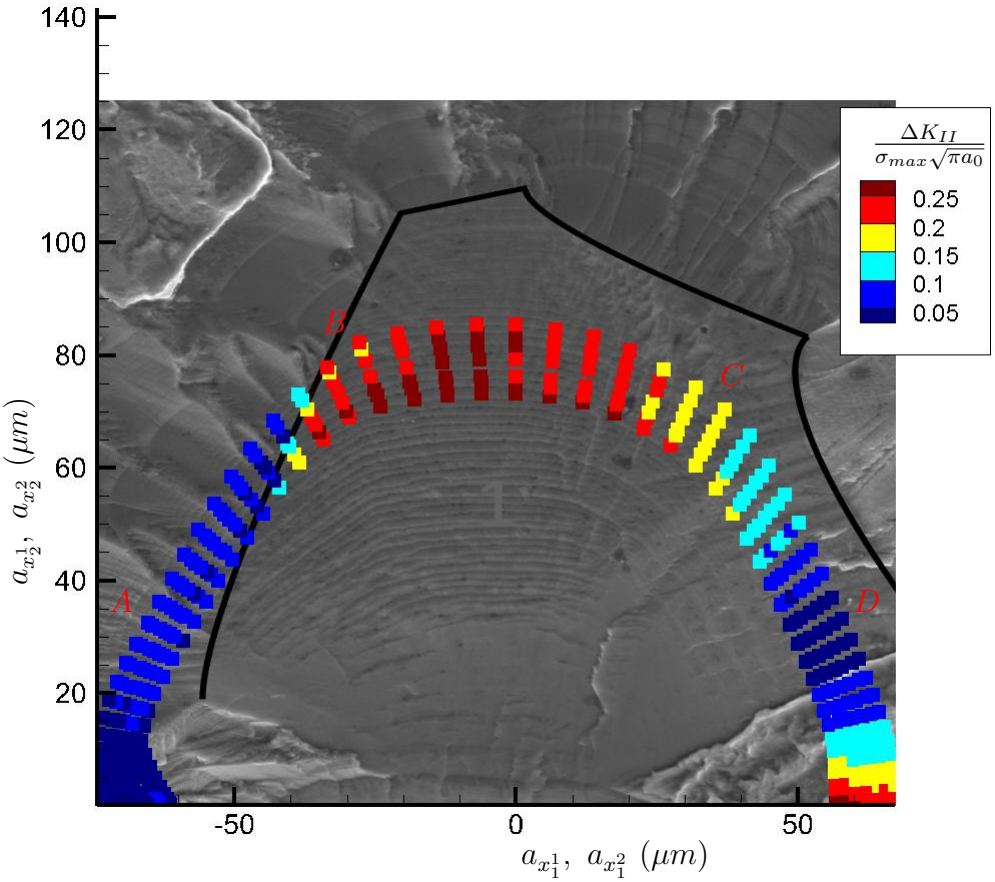

Figure 6.18: Range of the mode II stress intensity factors along the crack front increments when the crack front crosses the grain boundary

We can see a similar trend in the mode II stress intensity factor plot to that in the plot of the mode I stress intensity factors. Thus, we are able to simulate the retardation effect of the grain boundary on the microstructurally short fatigue crack growth rates using a simple exponential function. The parameters of this function are chosen based on the observed trends of the crack growth rates near the grain boundary. Thus, these parameters have to be studied in detail in order to use the range of the stress intensity factors as a parameter to predict the microstructurally short fatigue crack growth rates.

6.5 Conclusion

This chapter presents the background of the distributed dislocation technique developed by Hills et al. [86]. Recently, this technique has been used to model microstructurally short fatigue crack growth across multiple grains. In this chapter, we first validated the model against known numerical and analytical results present in literature. We then showed two approaches to incorporate the effect of the grain boundary on the microstructurally short fatigue crack growth rates. Both approaches have some limitations; however, they are able to capture the general trends of the microstructurally short fatigue crack growth rates as the crack front crosses the grain boundary. The first approach utilizes the crack tip displacements to predict the trends in the microstructurally short fatigue crack growth rates. In literature, crack tip displacements have been used by various authors in elastic-plastic fracture mechanics as well as in the microstructurally short crack growth regime to quantify the fatigue crack growth rates. Thus, using the crack tip displacement, we are able to predict the trends in the microstructurally short fatigue crack growth rates inside a grain. In the second approach, we assume that the applied stress is a function of the minimum distance of each crack front increment from the nearest grain boundary. This allows us to artificially reduce the applied stress as the crack front approaches the grain boundary. We apply this approach to crack growth across two facets that are inclined at an angle to each other. We are able to show correlation between the mode I stress intensity factor produced by this approach and the microstructurally short fatigue crack growth rates. However, further experimental and numerical studies are required to investigate the nature of the crack front interactions with the grain boundaries when the crack front spans more than one grain.

CHAPTER VII

Conclusion and Future Research

7.1 Summary of key contributions of the dissertation

In Chapter II, we combine linear elastic fracture mechanics with an irreversible cohesive model [37], which represents the crack tip mechanics, to predict fatigue crack growth rates in metal alloys. The main feature of this cohesive model is the hysteresis between the reloading and unloading paths. This hysteresis represents the energy dissipation due to various physical phenomena. The LEFM-cohesive model is applied to aluminum 7075-T6 and steel 4340 alloys by calibrating the cohesive parameters against zero applied stress ratio experimental fatigue crack growth rate curves and predicting fatigue crack growth rates for positive applied stress ratios. This novel method provides a tool for the quick calibration of cohesive parameters from macro-scale experiments or from lower scale simulations.

Chapter III contains two main contributions to the field of multiscale modeling of fatigue. First, we combine a finite element-based novel variational multiscale method [47] with an irreversible cohesive model [37] to predict macro-scale fatigue failure. As opposed to traditional cohesive zone modeling approaches, this variational multiscale cohesive method (VMCM) does not require the use of any special interface elements. Thus, we have demonstrated that different Paris curves can be obtained for different cohesive parameters. This method, combined with the properly calibrated LEFM-

based cohesive model described in Chapter II, can predict the macro-scale fatigue response, thereby eliminating the need for a computationally expensive cohesive model calibration procedure. The second contribution of this chapter is the development of the VMCM applied to microstructurally short crack growth. This micro-scale VMCM accurately predicts microscopic crack paths and mixed-mode failure. The calibration of the cohesive parameters used in the micro-scale VMCM is addressed in the next chapter.

In Chapter IV, we develop a micro-mechanical interpretation of the irreversible cohesive model by combining continuum dislocation theory [55] with an exponential cohesive model. This model, called Cohesive-BCS, is a new contribution to the field of microstructurally short fatigue crack growth. The Cohesive-BCS model accurately predicts microstructurally short fatigue crack growth across multiple grains in a Ni CMSX-4 alloy microstructure.

In Chapter V, we address the mechanism of microstructurally short fatigue crack growth retardation and arrest at a grain boundary. We develop a phenomenological grain boundary model that incorporates the geometric features of the interaction between the crack plane, the slip plane in the next grain, and the grain boundary plane. The model contains the following terms: coupling between the tilt and twist misorientations (located between the crack plane and a favorable plane in the next grain and calculated at a grain boundary), the Schmid factor, and the critical crack transmission stress, which is a form of a microscopic stress intensity factor. The model provides greater insight into the effect of grain boundary retardation and blocking on a short crack.

In Chapter VI, we extend the modeling approach described in Chapter IV to three dimensions to model the sub-surface growth of a microstructurally short fatigue crack. The new contributions are as follows: a model of the interaction of the short crack plane with a grain boundary and a model of the short crack growth on two planes that

span across a grain boundary. The method predicts the grain boundary retardation effect on a crack front as it approaches and passes through a grain boundary. This is consistent with observations of experimental micro-beach marks. Thus, using this method, a full three-dimensional understanding of the microstructurally short fatigue crack growth across multiple grains can be accomplished.

7.2 Suggestions for future research

We have listed some areas for future research that will help in the completion of the multiscale modeling framework for fatigue response shown in Figure 7.1.

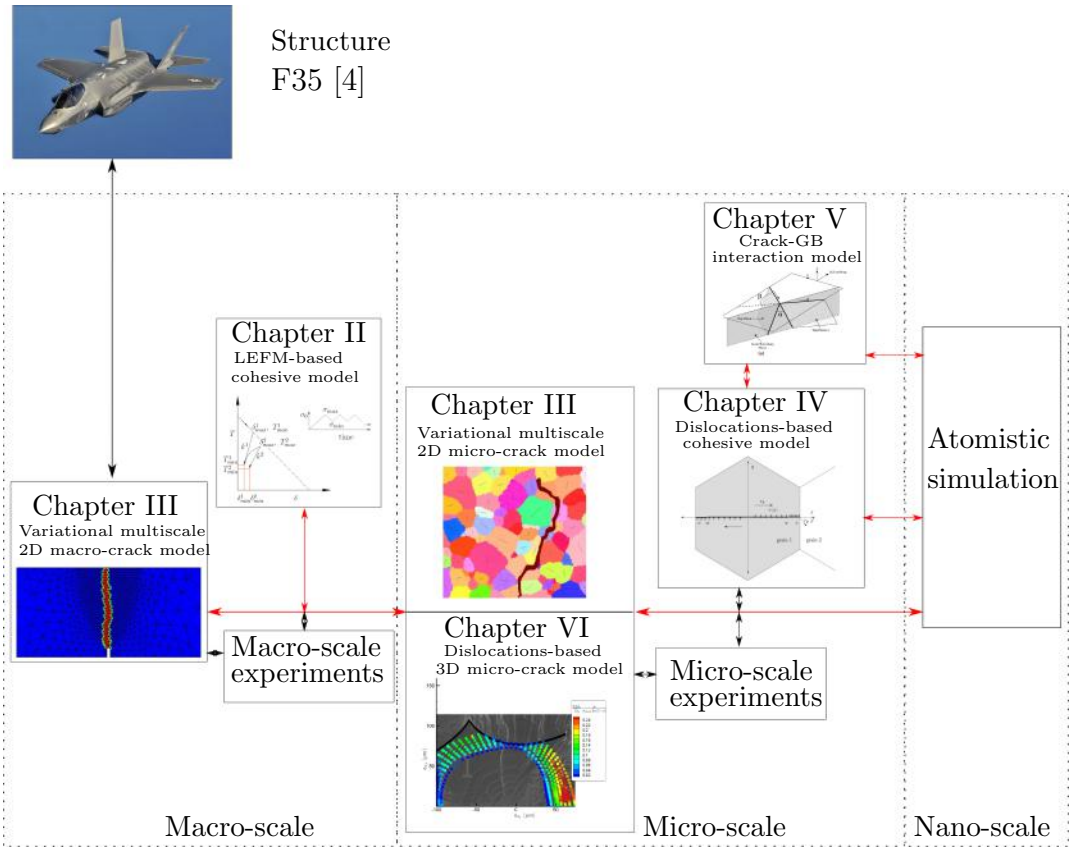

Figure 7.1: Multiscale modeling framework for fatigue response

In Figure 7.1, areas for future research are shown by red arrows. We now briefly describe some approaches to address them.

- The multiscale link between the VMM macro-crack and micro-crack models, described in Chapter III, has been accomplished by Shang et al. [111, 141] for monotonic failure. Thus, the extension to fatigue failure can be completed. The link between the LEFM-based irreversible cohesive model (Chapter II) and the VMM macro-crack model (Chapter III) is identified as a critical area for future research. Linking these two will provide fast calibration of the irreversible cohesive model parameters and macro-scale high cycle fatigue failure simulation.

- In the micro-scale, the incorporation of a wide variety of crystal plasticity methods developed in our research group [142, 143, 144, 145, 146, 147, 148, 149] in a variational multiscale cohesive framework will provide new simulation tools for the analysis of cracks and low cycle fatigue. Some work in this direction has been performed by Shang et al. [111, 141] for 2D problems. In three dimensions, Regueiro [150] has implemented the VMM to model strong discontinuities in rocks. Thus, this implementation can be combined with the irreversible cohesive model to model polycrystalline fatigue failure in three dimensions. Alternative 3D microstructure crack modeling methods such as smeared crack methods and graph cut based methods [151] could also be explored.

- In Chapter IV, we utilized a reversible exponential cohesive model with the theory of continuous distribution of dislocations developed by Bilby et al. [55] to predict microstructurally short fatigue crack growth. Future research in this area could utilize an irreversible cohesive model, such as the one described by Maiti and Geubelle [37], with the theory of continuous distribution of dislocations to capture the dissipation that occurs at the crack tip during cyclic loading.

- For the three-dimensional microstructurally short fatigue crack growth model described in Chapter VI, there are various areas for future research. The three-

dimensional fractographic information available from high-resolution X-ray tomography and 3D X-ray diffraction microscopy [77] can be used to model crack front increments spanning across multiple arbitrarily oriented grains. Thus, tilt and twist misorientations at each crack plane-grain boundary intersection can be explicitly incorporated by modeling the planes formed from these two misorientations (see [94]). Another area for future research could be the development of a numerical scheme for calculating the plastic zone size in front of the crack tip (see [93]). This would enable the model to incorporate the propagation of the plastic zone with the crack front. This will result in a more accurate representation of the plastic zone-grain boundary interaction when the plastic zone first touches the grain boundary. Another direction for future research could be the incorporation of an irreversible cohesive model to represent the local yield stress in the plastic zone as a function of the crack displacement. This will allow for the model to be calibrated from a lower-scale simulation.

- Life prediction is a critical step that will save costs by allowing less aggressive maintenance and replacement schedules of critical components. The ultimate objective of an integrated computational materials engineering (ICME) approach in fatigue analysis, however, is to custom design the fatigue behavior of advanced alloys using tailored microstructures. Future work should investigate optimization techniques that can be used to identify: (1) optimal microstructural features, such as crystallographic texture selection using optimization methods [152, 153] and statistical learning [154, 155, 156, 157, 158] and (2) microstructural design through carefully optimized thermomechanical processing sequences [159, 143, 160]) that can preferentially block cracks and enhance service lives of components.

- While this dissertation has provided a promising path towards a physics-based

prediction capability for fatigue crack propagation, one needs to recognize the inherently stochastic nature of cracking behavior. Random presence of manufacturing defects, material impurities, and environmental effects [161] can act as triggers for cracks, while intrinsic variability in the microstructure, such as grain sizes and grain neighborhoods [144, 162, 146]), can affect crack trajectories. Physics-based models cannot take into account all such underlying material variability. Thus, uncertainty quantification and probabilistic modeling is an essential tool for maintaining the robustness of numerical results and accounting for sensitivity to both extrinsic and intrinsic parameters [163, 164, 165, 166]. Such methods will be studied in the future in order to establish bounds for material parameters, such as cohesive strengths and energies.

The incorporation of these methods into the multiscale modeling framework for fatigue response will help in its completion. This framework will provide fast multiscale simulations for the fatigue response of advanced materials and help engineers fully utilize the capabilities of these materials in advanced applications.

APPENDICES

APPENDIX A

Bounded solution with a cohesive zone

[1]The cohesive zone equation is given by Eq. (4.2.2):

$$\ln(\tau_{fail}) - \ln(\tau_f(x)) = h_s \int_x^c B(x)dx,\ a < |x| < c \tag{A.1}$$

The dislocation density equation for the bounded case is

$$B(x) = -\frac{2\alpha\sqrt{c^2 - x^2}}{\pi G} \int_{-c}^{c} \frac{\tau(x')}{(x - x')\sqrt{c^2 - x'^2}} dx',\quad -c < x < c \tag{A.2}$$

where the plastic zone size is calculated from the bounded condition for the dislocation density, which is given by Eq. (4.1.5):

$$\int_{-c}^{c} \frac{\tau(x)}{\sqrt{c^2 - x^2}} dx = 0 \tag{A.3}$$

The second condition on c (Eq. (4.1.6)) is satisfied by the symmetry of the stress field, $\tau(x)$.

[1]Reproduced from Shardul Panwar and Veera Sundararaghavan. Dislocation theory-based cohesive model for microstructurally short fatigue crack growth. *Materials Science and Engineering: A*, 708:395–404, 2017

The stress function is

$$\tau(x) = \begin{cases} \tau_f(x) - \tau_A, & a < |x| < c \\ -\tau_A, & |x| < a \end{cases} \tag{A.4}$$

Putting the above stress function, $\tau(x)$, into Eq. (A.3) gives

$$\int_a^c \frac{\tau(x)}{\sqrt{c^2 - x^2}} dx = \frac{\pi \tau_A}{2} \tag{A.5}$$

Eq. (A.2) is put into the cohesive equation, Eq. (A.1), and the result is

$$\ln(\tau_f(x)) - \ln(\tau_{fail}) = \frac{2\alpha h_s}{\pi G} \int_{-c}^{c} \frac{\tau(x')}{\sqrt{c^2 - x'^2}} \underbrace{\left(\int_x^c \frac{\sqrt{c^2 - x^2}}{(x - x')} dx \right)}_{I_1(x,x')} dx', \quad a < |x| < c \tag{A.6}$$

$I_1(x, x')$ in the above equation can be simplified as

$$\begin{aligned} I_1(x, x') &= \int_x^c \frac{\sqrt{c^2 - x^2}}{(x - x')} dx \\ &= \int_x^c \frac{c^2 x' + c^2 x - x' x - x^3}{(x^2 - x'^2)\sqrt{c^2 - x^2}} dx \\ &= \frac{\sqrt{c^2 - x'^2}}{2} \ln \left| \frac{x\sqrt{c^2 - x'^2} + x'\sqrt{c^2 - x^2}}{x\sqrt{c^2 - x'^2} - x'\sqrt{c^2 - x^2}} \right| \\ &\quad + \frac{\sqrt{c^2 - x'^2}}{2} \ln \left| \frac{\sqrt{c^2 - x'^2} + \sqrt{c^2 - x^2}}{\sqrt{c^2 - x'^2} - \sqrt{c^2 - x^2}} \right| \\ &\quad - \sqrt{c^2 - x^2} - x' \left(\frac{\pi}{2} - \arcsin \frac{x}{c} \right) \end{aligned} \tag{A.7}$$

Putting the simplified expression back for $I_1(x, x')$ into Eq. (A.6) gives

$$\ln(\tau_f(x)) - \ln(\tau_{fail}) = \frac{2\alpha h_s}{\pi G} \int_{-c}^{c} \Bigg[\ln \left| \frac{x\sqrt{c^2 - x'^2} + x'\sqrt{c^2 - x^2}}{x\sqrt{c^2 - x'^2} - x'\sqrt{c^2 - x^2}} \right| + \frac{\sqrt{c^2 - x'^2}}{2} \ln \left| \frac{\sqrt{c^2 - x'^2} + \sqrt{c^2 - x^2}}{\sqrt{c^2 - x'^2} - \sqrt{c^2 - x^2}} \right| - \sqrt{c^2 - x^2} - x' \left(\frac{\pi}{2} - \arcsin \frac{x}{c} \right) \Bigg] \tau(x') dx' \tag{A.8}$$

Utilizing the symmetry of the stress field (Eq. (4.1.6)) and Eqs. (A.4) and (A.5) in the above equation simplifies the above expression to

$$\ln(\tau_f(x)) = \frac{2h_s\alpha}{\pi G} \left(\int_a^c \tau_f(x') I_b(x, x') dx' \right) + \ln(\tau_{fail}), \ a < |x| < c \tag{A.9}$$

Here,

$$I_b(x, x') = \ln \left| \frac{x\sqrt{c^2 - x'^2} + x'\sqrt{c^2 - x^2}}{x\sqrt{c^2 - x'^2} - x'\sqrt{c^2 - x^2}} \right| + \ln \left| \frac{\sqrt{c^2 - x'^2} + \sqrt{c^2 - x^2}}{\sqrt{c^2 - x'^2} - \sqrt{c^2 - x^2}} \right| - 2\frac{\sqrt{c^2 - x^2}}{\sqrt{c^2 - x'^2}}$$

APPENDIX B

Unbounded solution with a cohesive zone

[1]Again, the cohesive zone equation is given by Eq. (4.2.2):

$$\ln(\tau_{fail}) - \ln(\tau_f(x)) = h_s \int_x^c B(x)dx,\ a < |x| < c \tag{B.1}$$

The dislocation density equation for the unbounded case is

$$B(x) = -\frac{2\alpha\sqrt{c^2-x^2}}{\pi G}\int_{-c}^{c}\frac{\tau(x')}{(x-x')\sqrt{c^2-x'^2}}dx' - \frac{2\alpha}{\pi G}\frac{x}{\sqrt{c^2-x^2}}\int_{-c}^{c}\frac{\tau(x')}{\sqrt{c^2-x'^2}}dx'\ ,$$
$$-c < x < c \tag{B.2}$$

The stress function is

$$\tau(x) = \begin{cases} \tau_f(x) - \tau_A, & a < |x| < c \\ -\tau_A, & |x| < a \end{cases} \tag{B.3}$$

The dislocation density equation (Eq. (B.2)) is put into the cohesive zone equation

[1]Reproduced from Shardul Panwar and Veera Sundararaghavan. Dislocation theory-based cohesive model for microstructurally short fatigue crack growth. *Materials Science and Engineering: A*, 708:395–404, 2017

(Eq. (B.1)), resulting in

$$\begin{aligned}\ln(\tau_f(x)) - \ln(\tau_{fail}) =& \frac{2\alpha h_s}{\pi G}\int_{-c}^{c}\frac{\tau(x')}{\sqrt{c^2-x'^2}}\underbrace{\left(\int_x^c \frac{\sqrt{c^2-x^2}}{(x-x')}dx\right)}_{I_1(x,x')}dx' \\ &+ \frac{2\alpha h_s}{\pi G}\sqrt{c^2-x^2}\int_{-c}^{c}\frac{\tau(x')}{\sqrt{c^2-x'^2}}dx', \quad a<|x|<c\end{aligned} \tag{B.4}$$

We can use $I_1(x,x')$ (Eq. (A.7)) from Appendix A in Eq. (B.4) to get

$$\begin{aligned}\ln(\tau_f(x)) - \ln(\tau_{fail}) =& \frac{2\alpha h_s}{\pi G}\int_{-c}^{c}\tau(x')\Bigg[\ln\left|\frac{x\sqrt{c^2-x'^2}+x'\sqrt{c^2-x^2}}{x\sqrt{c^2-x'^2}-x'\sqrt{c^2-x^2}}\right| \\ &+ \ln\left|\frac{\sqrt{c^2-x'^2}+\sqrt{c^2-x^2}}{\sqrt{c^2-x'^2}-\sqrt{c^2-x^2}}\right|\Bigg]dx' \\ &- \frac{2\alpha h_s}{\pi G}\int_{-c}^{c}\left(\frac{\pi}{2}-\arcsin\frac{x}{c}\right)\frac{x'\tau(x')}{\sqrt{c^2-x'^2}}dx', \quad a<|x|<c\end{aligned} \tag{B.5}$$

Finally, we can use the stress function (Eq. (B.3)) in the above expression to get

$$\begin{aligned}\ln(\tau_f(x)) =& \frac{2h_s\alpha}{\pi G}\left(\int_a^c \tau_f(x')I_u(x,x')dx'\right) - \frac{2h_s\alpha\tau_A}{G}\sqrt{c^2-x^2} + \ln(\tau_{fail}) \ , \\ & a<|x|<c\end{aligned} \tag{B.6}$$

Here, $I_u(x,x')$ is given by

$$\begin{aligned}I_u(x,x') =& \ln\left|\frac{x\sqrt{c^2-x'^2}+x'\sqrt{c^2-x^2}}{x\sqrt{c^2-x'^2}-x'\sqrt{c^2-x^2}}\right| + \ln\left|\frac{\sqrt{c^2-x'^2}+\sqrt{c^2-x^2}}{\sqrt{c^2-x'^2}-\sqrt{c^2-x^2}}\right| \\ &- 2\left(\frac{\pi}{2}-\arcsin\frac{x}{c}\right)\frac{x'}{\sqrt{c^2-x'^2}}\end{aligned}$$

APPENDIX C

A piecewise polynomial collocation method

[1]The kernels of the integrands of Eqs. (A.6) and (B.6) are singular when $x = x'$ as well as at the domain boundaries ($x,\ x' = a, c$). Thus, to solve these types of weakly singular Fredholm equations, we make use of polynomial splines with a graded mesh [101].

Using the method described in Brunner et al. [101], we split our domain ($a < |x| < c$) in half. Let $a = x_0 < x_1 < .... < x_N = \frac{c+a}{2}$ be the partition points for the first half of the domain. The partition points for the second half of the domain $(x_{N+1}, ..., x_{2N})$ are obtained by reflecting the partition points of the first half about $x_N = \frac{c+a}{2}$. The mesh nodes for the first half of the domain are determined by

$$x_j = a + \left(\frac{j}{N}\right)^r \left(\frac{c-a}{2}\right),\ j = 0, 1, 2, ..., N$$

and the points of the second half are calculated by

$$x_{j+N} = c + a - x_{N-j},\ j = 1, 2, 3, ..., N$$

[1]Reproduced from Shardul Panwar and Veera Sundararaghavan. Dislocation theory-based cohesive model for microstructurally short fatigue crack growth. *Materials Science and Engineering: A*, 708:395–404, 2017

For every subinterval $([x_j, x_{j+1}],\ j = 1, 2, ..., 2N)$, we choose $m = 2$ collocation points, which are given by

$$\xi_{ji} = x_j + \frac{\eta_i + 1}{2}\big(x_{j+1} - x_j\big),\ i = 1, 2 \tag{C.1}$$

Here, η_1 and η_2 are the gauss quadrature points that satisfy the following condition:

$$-1 \leqslant \eta_1 \leqslant \eta_2 \leqslant +1$$

In this paper, we use $\eta_1 = -\frac{1}{\sqrt{3}}$ and $\eta_2 = \frac{1}{\sqrt{3}}$.

We assume that the piecewise polynomial interpolation $\tau_{fN} : [a, c]$ can be used instead of a continuous function τ_f in the weakly singular equations. On every subinterval $[x_{j-1}, x_j],\ (j = 1, ..., 2N)$, τ_{fN} is a polynomial of degree 1 and interpolates τ_f at the points ξ_{j1} and ξ_{j2}.

$$\tau_{fN}(\xi_{ji}) = \tau_f(\xi_{ji}),\ i = 1, 2;\ j = 1, ..., 2N$$

Thus, this interpolation function is independently defined on each subinterval $[x_{j-1}, x_j],\ (j = 1, ..., 2N)$ and may be discontinuous at the interior grid points $x = x_j,\ (j = 1, ..., 2N - 1)$. The interpolation function τ_{fN} in the interval $[x_{j-1}, x_j],\ (j = 1, ..., 2N)$ is represented as

$$\tau_{fN}(x) = \sum_{i=1}^{2} s_{ji}\phi_{ji}(x),\ x \in [x_{j-1}, x_j]$$

where $\phi_{ji}(x),\ x \in [x_{j-1}, x_j]$ is a polynomial of degree $m - 1$, such that

$$\phi_{ji}(\xi_{jk}) = \begin{cases} 1,\ if \quad k = i \\ 0,\ if \quad k \neq i \end{cases},\ k = 1, ..., m$$

In this paper, the approximate solution τ_{fN} within the interval $[x_{j-1}, x_j]$, $(j = 1, ..., 2N)$ is represented as

$$\tau_{fN}(x) = s_{j1}\frac{\xi_{j2} - x}{\xi_{j2} - \xi_{j1}} + s_{j2}\frac{x - \xi_{j1}}{\xi_{j2} - \xi_{j1}},\ x_{j-1} \leqslant x \leqslant x_j \tag{C.2}$$

Here, ξ_{j1} and ξ_{j2} are determined from Eq. (C.1), and the coefficients s_{j1} and s_{j2} are the unknown variables.

Thus, for the condition in which the crack and the associated plastic zone are completely inside a grain, Eqs. (A.5) and (A.9) are discretized as

$$\sum_{j=1}^{2N}\sum_{i=1}^{2}\left[\ln(s_{ji}) - \ln(\tau_{fail}) = \frac{2h_s\alpha}{\pi G}\left\{\sum_{l=1}^{2N}\int_{x_{l-1}}^{x_l}\left(s_{l1}\frac{\xi_{l2} - x'}{\xi_{l2} - \xi_{l1}} + s_{l2}\frac{x' - \xi_{l1}}{\xi_{l2} - \xi_{l1}}\right)I_b(x, x')dx'\right\}\right] \tag{C.3}$$

$$\sum_{l=1}^{2N}\int_{x'_{l-1}}^{x'_l}\left(s_{l1}\frac{\xi_{l2} - x'}{\xi_{l2} - \xi_{l1}} + s_{l2}\frac{x' - \xi_{l1}}{\xi_{l2} - \xi_{l1}}\right)\frac{1}{\sqrt{c^2 - x^2}}dx = \frac{\pi\tau_A}{2} \tag{C.4}$$

These are coupled nonlinear equations with unknown variables $s_{ji},\ j = 1, ..., 2N,\ i = 1, 2$ and c.

Similarly, for the condition in which the plastic zone in front of the crack tip has reached a grain boundary, Eq. (B.6) is discretized as

$$\sum_{j=1}^{2N}\sum_{i=1}^{2}\left[\ln(s_{ji}) - \ln(\tau_{fail}) + \frac{2h_s\alpha\tau_A}{G}\sqrt{c^2 - x^2} = \frac{2h_s\alpha}{\pi G}\left\{\sum_{l=1}^{2N}\int_{x_{l-1}}^{x_l}\left(s_{l1}\frac{\xi_{l2} - x'}{\xi_{l2} - \xi_{l1}} + s_{l2}\frac{x' - \xi_{l1}}{\xi_{l2} - \xi_{l1}}\right)I_u(x, x')dx'\right\}\right] \tag{C.5}$$

These equations (Eqs. (C.3) and (C.5)) are solved for the unknown variables using the Newton-Raphson numerical scheme.

After solving Eq. (C.5), the unbounded dislocation density is determined from Eq. (B.2). The unbounded dislocation density is then used in Eq. (4.1.8) to find the stress in the adjacent grain at a distance r_0 from the grain boundary ($S(r_0)$), which is produced by the dislocations piling up at the grain boundary.

APPENDIX D

Explicit expressions for kernel functions K^s_{ijk} and K^c_{ijk}

In this appendix, the expressions for the infinite space kernel functions K^s_{ijk} and K^c_{ijk} are taken from [167, 86]. The expression for K^s_{ijk} can be derived from Kelvin's solution [168] using Eq. (6.1.8). The final expression is

$$\begin{aligned} K^s_{ijk} =& \frac{\mu}{4\pi(1-\nu)r^3}\Bigg[-(1-4\nu)\delta_{ji}\delta_{k3} + (1-2\nu)(\delta_{jk}\delta_{i3}+\delta_{j3}\delta_{ik}) - 15\frac{r_i r_j r_k r_3}{r^4} \\ &+ 3\nu\frac{\delta_{jk}r_i r_3 + \delta_{j3}r_i r_k + \delta_{ik}r_j r_3 + \delta_{i3}r_j r_k}{r^2} + 3(1-2\nu)\frac{\delta_{ij}r_k r_3 + \delta_{k3}r_i r_j}{r^2}\Bigg] \end{aligned} \tag{D.1}$$

where μ is the shear modulus, $r_i = x_i - y_i$, and $r = \sqrt{r_i r_i}$.

The expression for the half-space kernel function K^c_{ijk} is derived from Mindlin's solution [169]. Mindlin's solution was expressed in a coordinate set $OX_1X_2X_3$, in which the X_3 axis is perpendicular to the free surface and is pointing towards the half-space. The coordinate system used for the crack plane is $ox_1x_2x_3$, in which the crack surface is in the $x_1 - x_2$ plane. Thus, K^c_{ijk} is found by a tensor transformation as shown below:

$$K^c_{ijk} = a_{ip}a_{jq}a_{3r}a_{ks}H_{pqrs}(\mathbf{X}(\mathbf{x}), \mathbf{Y}(\mathbf{y})) \tag{D.2}$$

where a is the transformation tensor from the coordinate system $OX_1X_2X_3$ to the crack surface coordinate system $ox_1x_2x_3$. H_{pqrs} is a 4th order tensor defined as

$$H_{pqrs} = \mu\left[\frac{\partial T^c_{pqr}(\mathbf{X},\mathbf{Y})}{\partial Y_s} + \frac{\partial T^c_{pqs}(\mathbf{X},\mathbf{Y})}{\partial Y_r} + \frac{2\nu}{1-2\nu}\frac{\partial T^c_{pqi}(\mathbf{X},\mathbf{Y})}{\partial Y_i}\delta_{rs}\right] \tag{D.3}$$

where T^c_{pqr} is Mindlin's non-singular stress influence function for a half-space.

H_{pqrs} tensor has only 36 independent components because of symmetry of stress and strain fields.

$$H_{pqrs} = H_{qprs} = H_{pqsr}$$

The remaining components on this tensor are derived from Eq. (D.3). [1]They are

$$\begin{aligned}
H_{\alpha\alpha\alpha\alpha} = K_h\Bigg\{ & -\frac{(1-2\nu)(5-4\nu)}{R^3}\left(1-3\frac{r_\alpha^2}{R^2}\right) + \frac{3(3-4\nu)r_\alpha^2}{R^5}\left(3-5\frac{r_\alpha^2}{R^2}\right) \\
& - \frac{12\nu Y_3 R_3}{R^5}\left(1-5\frac{r_\alpha^2}{R^2}\right) + \frac{6X_3Y_3}{R^5}\left(3-30\frac{r_\alpha^2}{R^2}+35\frac{r_\alpha^4}{R^4}\right) \\
& + \frac{12(1-\nu)(1-2\nu)}{R(R+R_3)^2}\left[1-2\frac{r_\alpha^2(3R+R_3)}{R^2(R+R_3)} + \frac{r_\alpha^4(5R^2+4RR_3+R_3^2)}{R^4(R+R_3)^2}\right] + h_\alpha\Bigg\} \\
H_{\beta\beta\alpha\alpha} = K_h\Bigg\{ & -\frac{(1-2\nu)(3-4\nu)}{R^3}\left(1-3\frac{r_\alpha^2}{R^2}\right) + \frac{3(3-4\nu)r_\beta^2}{R^5}\left(1-5\frac{r_\alpha^2}{R^2}\right) \\
& - \frac{12\nu Y_3 R_3}{R^5}\left(1-5\frac{r_\alpha^2}{R^2}\right) + \frac{6X_3Y_3}{R^5}\left(1-5\frac{r_\alpha^2+r_\beta^2}{R^2}+35\frac{r_\alpha^2 r_\beta^2}{R^4}\right) \\
& + \frac{4(1-\nu)(1-2\nu)}{R(R+R_3)^2}\left[1-\frac{(r_\alpha^2+r_\beta^2)(3R+R_3)}{R^2(R+R_3)} + 3\frac{r_\alpha^2 r_\beta^2(5R^2+4RR_3+R_3^2)}{R^4(R+R_3)^2}\right] \\
& + h_\beta\Bigg\} \quad (\alpha \neq \beta) \\
H_{12\alpha\alpha} = K_h\Bigg\{ & \frac{3(7-10\nu)}{R^5} - \frac{15(3-4\nu)r_\alpha^2}{R^7} - \frac{30X_3Y_3}{R^7}\left(3-7\frac{r_\alpha^2}{R^2}\right) \\
& - \frac{12(1-\nu)(1-2\nu)}{R^3(R+R_3)^2}\left[\frac{3R+R_3}{R+R_3} - \frac{r_\alpha^2(5R^2+4RR_3+R_3^2)}{R^2(R+R_3)^2}\right] + h_3\Bigg\} r_{3-\alpha}r_\alpha
\end{aligned}$$

[1]Taken with corrections from David Anthony Hills, PA Kelly, DN Dai, and AM Korsunsky. *Solution of crack problems: the distributed dislocation technique*, volume 44. Springer Science & Business Media, 2013

$$
\begin{aligned}
H_{3\alpha\alpha\alpha} &= K_h\Bigg\{3\frac{(3-4\nu)X_3+Y_3}{R^5}\left(3-5\frac{r_\alpha^2}{R^2}\right)-\frac{30X_3Y_3R_3}{R^7}\left(3-7\frac{r_\alpha^2}{R^2}\right)-\frac{6R_3}{R^5}\\
&\quad-\frac{12\nu X_3}{R^5}\left(1-5\frac{R_3^2}{R^2}\right)\Bigg\}r_\alpha\\
H_{3\beta\alpha\alpha} &= K_h\Bigg\{3\frac{(3-4\nu)X_3+Y_3}{R^5}\left(1-5\frac{r_\alpha^2}{R^2}\right)-\frac{30X_3Y_3R_3}{R^7}\left(1-7\frac{r_\alpha^2}{R^2}\right)-\frac{6\nu R_3}{R^5}\\
&\quad-\frac{12\nu X_3}{R^5}\left(1-5\frac{R_3^2}{R^2}\right)\Bigg\}r_\beta\quad(\alpha\neq\beta)\\
H_{33\alpha\alpha} &= K_h\Bigg\{\frac{(1-2\nu)}{R^3}\left(1-3\frac{r_\alpha^2}{R^2}\right)+3\frac{(3-4\nu)X_3R_3+Y_3r_3}{R^5}\left(1-5\frac{r_\alpha^2}{R^2}\right)\\
&\quad-\frac{30X_3Y_3R_3^2}{R^7}\left(1-7\frac{r_\alpha^2}{R^2}\right)-\frac{2\nu}{R^3}\left(1-3\frac{R_3^2}{R^2}\right)-\frac{12\nu X_3R_3}{R^5}\left(3-5\frac{R_3^2}{R^2}\right)\Bigg\}\\
H_{\alpha\alpha12} &= K_h\Bigg\{\frac{3(7-16\nu+8\nu^2)}{R^5}-15\frac{(3-4\nu)r_\alpha^2-4\nu Y_3R_3}{R^7}-\frac{30X_3Y_3}{R^7}\left(3-7\frac{r_\alpha^2}{R^2}\right)\\
&\quad-\frac{12(1-\nu)(1-2\nu)}{R^3(R+R_3)^2}\left[\frac{3R+R_3}{R+R_3}-\frac{r_\alpha^2(5R^2+4RR_3+R_3^2)}{R^2(R+R_3)^2}\right]\Bigg\}r_1r_2\\
H_{1212} &= K_h\Bigg\{-\frac{1-2\nu}{R^3}+\frac{3(2-3\nu)(r_1^2+r_2^2)}{R^5}-\frac{15(3-4\nu)r_1^2r_2^2}{R^7}\\
&\quad+\frac{6X_3Y_3}{R^5}\left(1-5\frac{r_1^2+r_2^2}{R^2}+35\frac{r_1^2r_2^2}{R^4}\right)\\
&\quad+\frac{4(1-\nu)(1-2\nu)}{R(R+R_3)^2}\left[1-\frac{(r_1^2+r_2^2)(3R+R_3)}{R^2(R+R_3)}+3\frac{r_1^2r_2^2(5R^2+4RR_3+R_3^2)}{R^4(R+R_3)^2}\right]\Bigg\}\\
H_{\alpha312} &= K_h\Bigg\{-\frac{3(1-\nu)R_3}{R^5}+3\frac{(3-4\nu)X_3+Y_3}{R^5}\left(1-5\frac{r_\alpha^2}{R^2}\right)\\
&\quad-\frac{30X_3Y_3R_3}{R^7}\left(1-7\frac{r_\alpha^2}{R^2}\right)\Bigg\}r_{3-\alpha}\\
H_{3312} &= K_h\Bigg\{-\frac{3(1-2\nu)}{R^5}-15\frac{(3-4\nu)X_3-Y_3}{R^7}R_3-\frac{30X_3Y_3}{R^7}\left(1-7\frac{R_3^2}{R^2}\right)\Bigg\}r_1r_2\\
H_{\alpha\alpha\alpha3} &= K_h\Bigg\{\frac{6R_3}{R^5}-3\frac{X_3+(3-4\nu)Y_3}{R^5}\left(3-5\frac{r_\alpha^2}{R^2}\right)+\frac{30X_3Y_3R_3}{R^7}\left(3-7\frac{r_\alpha^2}{R^2}\right)\\
&\quad+\frac{12\nu Y_3}{R^5}\left(1-5\frac{R_3^2}{R^2}\right)\Bigg\}r_\alpha\\
H_{\alpha\alpha\beta3} &= K_h\Bigg\{\frac{6\nu R_3}{R^5}-3\frac{X_3+(3-4\nu)Y_3}{R^5}\left(1-5\frac{r_\alpha^2}{R^2}\right)+\frac{30X_3Y_3R_3}{R^7}\left(1-7\frac{r_\alpha^2}{R^2}\right)\\
&\quad+\frac{12\nu Y_3}{R^5}\left(1-5\frac{R_3^2}{R^2}\right)\Bigg\}r_\beta\quad(\alpha\neq\beta)
\end{aligned}
$$

$$
\begin{aligned}
H_{12\alpha 3} &= K_h\Bigg\{\frac{3(1-\nu)R_3}{R^5} - 3\frac{X_3+(3-4\nu)Y_3}{R^5}\left(1-5\frac{r_\alpha^2}{R^2}\right) + \frac{30X_3Y_3R_3}{R^7}\left(1-7\frac{r_\alpha^2}{R^2}\right)\Bigg\}r_{3-\alpha}\\
H_{\alpha 3\alpha 3} &= K_h\Bigg\{-\frac{1}{R^3}\left[(1-2\nu)+3\nu\frac{r_\alpha^2+R_3^2}{R^2}-15\frac{r_\alpha^2R_3^2}{R^4}\right]\\
&\quad -\frac{6X_3Y_3}{R^5}\left[1-5\frac{r_\alpha^2+R_3^2}{R^2}+35\frac{r_\alpha^2R_3^2}{R^4}\right]\Bigg\}\\
H_{\alpha 3\beta 3} &= K_h\Bigg\{\frac{3(1-\nu)}{R^5} - \frac{3}{R^5}\left(1-5\frac{R_3^2}{R^2}\right) + \frac{30X_3Y_3}{R^7}\left(1-7\frac{R_3^2}{R^2}\right)\Bigg\}r_\alpha r_\beta \quad (\alpha\neq\beta)\\
H_{33\alpha 3} &= K_h\Bigg\{-\frac{3r_3}{R^5}\left(1-5\frac{R_3^2}{R^2}\right) + \frac{30X_3Y_3R_3}{R^7}\left(3-7\frac{R_3^2}{R^2}\right)\Bigg\}r_\alpha\\
H_{\alpha\alpha 33} &= K_h\Bigg\{-\frac{(1-2\nu)(3+4\nu)}{R^3}\left(1-3\frac{R_3^2}{R^2}\right) - \frac{12\nu Y_3R_3}{R^5}\left(3-5\frac{R_3^2}{R^2}\right)\\
&\quad +\frac{3(3-4\nu)r_\alpha^2}{R^5}\left(1-5\frac{R_3^2}{R^2}\right) - \frac{12(1-2\nu)X_3R_3}{R^5}\left(1-5\frac{r_\alpha^2}{R^2}\right)\\
&\quad +\frac{6X_3Y_3}{R^5}\left(1-5\frac{r_\alpha^2+R_3^2}{R^2}+35\frac{R_3^2r_\alpha^2}{R^4}\right)\\
&\quad +\frac{4(1-\nu)(1-2\nu)}{R^3}\left(1-3\frac{r_\alpha^2}{R^2}\right)+h_\alpha\Bigg\}\\
H_{1233} &= K_h\Bigg\{-\frac{12(1-\nu)(1-2\nu)}{R^5} + \frac{3(3-4\nu)}{R^5}\left(1-5\frac{R_3^2}{R^2}\right)\\
&\quad +\frac{60(1-2\nu)X_3R_3}{R^7} - \frac{30X_3Y_3}{R^7}\left(1-7\frac{R_3^2}{R^2}\right)+h_3\Bigg\}r_1r_2\\
H_{\alpha 333} &= K_h\Bigg\{-\frac{3r_3}{R^5}\left(1-5\frac{R_3^2}{R^2}\right) - \frac{30X_3Y_3R_3}{R^7}\left(3-7\frac{R_3^2}{R^2}\right)\Bigg\}r_\alpha\\
H_{3333} &= K_h\Bigg\{-\frac{1}{R^3}\left(1+6\frac{R_3^2}{R^2}-15\frac{R_3^4}{R^4}\right) + \frac{6X_3Y_3}{R^5}\left(3-30\frac{R_3^2}{R^2}+35\frac{R_3^4}{R^4}\right)\Bigg\}
\end{aligned}
$$

where $r_i = X_i - Y_i$, $R_3 = X_3 + Y_3$, $R^2 = r_\alpha r_\alpha + R_3^2$, $K_h = \mu/\big[4\pi(1-\nu)\big]$ is a material constant, and $\alpha,\ \beta = 1$ to 2 and no summation is implied by a repeated index.

h_α and h_3 are given by

$$
\begin{aligned}
h_\alpha = & \frac{2\nu}{R^3}\left[(1-2\nu)\left(1-3\frac{r_\alpha^2}{R^2}\right)-\frac{6X_3R_3}{R^2}\left(1-5\frac{r_\alpha^2}{R^2}\right)-4\nu\left(1-3\frac{R_3^2}{R^2}\right)\right] \\
& + \frac{4\nu(1-\nu)}{R(R+R_3)^2}\left[4-\frac{(7r_\alpha^2+r_{3-\alpha}^2)(3R+R_3)}{R^2(R+R_3)}+3\frac{r_\alpha^2(r_\alpha^2+r_{3-\alpha}^2)(5R^2+4RR_3+R_3^2)}{R^4(R+R_3)^2}\right] \\
h_3 = & -\frac{6\nu}{R^5}\left[(1-2\nu)-10\frac{X_3R_3}{R^2}\right] \\
& - \frac{12\nu(1-\nu)}{R^3(R+R_3)^2}\left[\frac{2(3R+R_3)}{R+R_3}-\frac{(r_1^2+r_2^2)(5R^2+4RR_3+R_3^2)}{R^2(R+R_3)^2}\right]
\end{aligned}
$$

APPENDIX E

Explicit expressions for regular contour integrals

$$L,\ L_{\alpha\beta},\ M_{\gamma},\ M_{\alpha\beta\gamma}$$

For linear triangular and linear quadrilateral elements, the closed form of contour integrals $L,\ L_{\alpha\beta},\ M_{\gamma},\ M_{\alpha\beta\gamma}$ are shown below [1]:

$$L = \sum_{i=1}^{n} \frac{1}{a_i}\big[\cos\theta_{i+1} - \cos\theta_i + k_i(\sin\theta_{i+1} - \sin\theta_i)\big] \tag{E.1}$$

$$L_{11} = \sum_{i=1}^{n} \frac{1}{3a_i}\big[\cos^3\theta_{i+1} - \cos^3\theta_i + k_i(3\sin\theta_{i+1} - 3\sin\theta_i - \sin^3\theta_{i+1} + \sin^3\theta_i)\big] \tag{E.2}$$

$$L_{12} = \sum_{i=1}^{n} \frac{1}{3a_i}\big[-\sin^3\theta_{i+1} + \sin^3\theta_i + k_i(-\cos^3\theta_{i+1} + \cos^3\theta_i)\big] \tag{E.3}$$

$$M_1 = \sum_{i=1}^{n} -\frac{k_i}{\sqrt{(1+k_i^2)}} I_i \tag{E.4}$$

$$M_2 = \sum_{i=1}^{n} \frac{1}{\sqrt{(1+k_i^2)}} I_i \tag{E.5}$$

[1] Taken with a correction from DN Dai, DA Hills, and D Nowell. Formulation and implementation of the eigenstrain method employing higher order elements. *International journal of solids and structures*, 33(3):331–342, 1996

$$M_{121} = \sum_{i=1}^{n} \frac{1}{3(1+k_i^2)} \Bigg[-\cos\theta_{i+1} + \cos\theta_i + k_i(\sin\theta_{i+1} - \sin\theta_i) + \frac{1}{\sqrt{(1+k_i^2)}} I_i \Bigg] \tag{E.6}$$

$$M_{122} = \sum_{i=1}^{n} \frac{k_i}{3(1+k_i^2)} \Bigg[-\cos\theta_{i+1} + \cos\theta_i + k_i(\sin\theta_{i+1} - \sin\theta_i) - \frac{k_i^2}{\sqrt{(1+k_i^2)}} I_i \Bigg] \tag{E.7}$$

$$L_{21} = L_{12}$$

$$M_{\alpha\beta\gamma} = M_{\beta\alpha\gamma} = M_{\gamma\alpha\beta}$$

$$L_{22} = L - L_{11}$$

$$M_{\alpha\alpha\alpha} = M_\alpha - M_{\alpha\beta\beta} \ (\alpha \neq \beta)$$

In the above equations, n is the number of sides of the element and $a_i,\ k_i,\ \theta_i$, and I_i are

$$\begin{aligned}
a_i &= x_2^i - x_2^0 - k_i(x_1^i - x_1^0) \\
k_i &= \frac{x_2^{i+1} - x_2^i}{x_1^{i+1} - x_1^i} \\
\theta_i &= \tan^{-1} \frac{x_2^i - x_2^0}{x_1^i - x_1^0} \\
I_i &= \ln \frac{(\cos\theta_{i+1} + k_i \sin\theta_{i+1} + \sqrt{(1+k_i^2)}\ )r_{i+1}}{(\cos\theta_i + k_i \sin\theta_i + \sqrt{(1+k_i^2)}\ )r_i}
\end{aligned}$$

where r_i is the distance from collocation point (x_1^0, x_2^0) to the ith node (x_1^i, x_2^i) and $x_\alpha^{n+1} = x_\alpha^1$.

BIBLIOGRAPHY

BIBLIOGRAPHY

[1] Rick Berman and Brannon Braga. *Star Trek: Enterprise*. United States: Paramount Television, 2001.

[2] Mark F Horstemeyer. *Integrated Computational Materials Engineering (ICME) for metals: using multiscale modeling to invigorate engineering design with science*. John Wiley & Sons, 2012.

[3] Krishna Rajan. Learning from systems biology: an "omics" approach to materials design. *JOM Journal of the Minerals, Metals and Materials Society*, 60(3):53–55, 2008.

[4] Master Sgt. Donald R. Allen. U.S. Air Force F-35A Lightning II Joint Strike Fighter, 2013.

[5] J Lankford and FN Kusenberger. Initiation of fatigue cracks in 4340 steel. *Metallurgical Transactions*, 4(2):553–559, 1973.

[6] J Lankford. The growth of small fatigue cracks in 7075–T6 aluminum. *Fatigue & Fracture of Engineering Materials & Structures*, 5(3):233–248, 1982.

[7] RO Ritchie and J Lankford. Small fatigue cracks: a statement of the problem and potential solutions. *Materials Science and Engineering*, 84:11–16, 1986.

[8] JC Newman, Edward P Phillips, and MH Swain. Fatigue-life prediction method-

ology using small-crack theory. *International Journal of Fatigue*, 21(2):109–119, 1999.

[9] Alan A Griffith. The phenomena of rupture and flow in solids. *Philosophical transactions of the royal society of London. Series A, containing papers of a mathematical or physical character*, 221:163–198, 1921.

[10] George R Irwin. Analysis of stresses and strains near the end of a crack traversing a plate. *Journal of applied mechanics*, 24(3):361–364, 1957.

[11] Paul C Paris, Mario P Gomez, and William E Anderson. A rational analytic theory of fatigue. *The trend in engineering*, 13(1):9–14, 1961.

[12] Paul Croce Paris and Fazil Erdogan. A critical analysis of crack propagation laws. ASME, 1963.

[13] Ted L Anderson. *Fracture mechanics: fundamentals and applications*. CRC press, 2017.

[14] Wolf Elber. The significance of fatigue crack closure. In *Damage tolerance in aircraft structures*. ASTM International, 1971.

[15] G Xu, AS Argon, and M Ortiz. Nucleation of dislocations from crack tips under mixed modes of loading: implications for brittle against ductile behaviour of crystals. *Philosophical Magazine A*, 72(2):415–451, 1995.

[16] MH El Haddad, TH Topper, and KN Smith. Prediction of non propagating cracks. *Engineering Fracture Mechanics*, 11(3):573–584, 1979.

[17] DS Dugdale. Yielding of steel sheets containing slits. *Journal of the Mechanics and Physics of Solids*, 8(2):100–104, 1960.

[18] Grigory Isaakovich Barenblatt. The mathematical theory of equilibrium cracks in brittle fracture. *Advances in applied mechanics*, 7(1):55–129, 1962.

[19] JR Willis. A comparison of the fracture criteria of griffith and barenblatt. *Journal of the Mechanics and Physics of Solids*, 15(3):151–162, 1967.

[20] Arne Hillerborg, Mats Modéer, and P-E Petersson. Analysis of crack formation and crack growth in concrete by means of fracture mechanics and finite elements. *Cement and concrete research*, 6(6):773–781, 1976.

[21] Alan Needleman. A continuum model for void nucleation by inclusion debonding. *Journal of applied mechanics*, 54(3):525–531, 1987.

[22] Viggo Tvergaard and John W Hutchinson. The relation between crack growth resistance and fracture process parameters in elastic-plastic solids. *Journal of the Mechanics and Physics of Solids*, 40(6):1377–1397, 1992.

[23] J Planas, M Elices, and GV Guinea. Cohesive cracks versus nonlocal models: Closing the gap. *International Journal of Fracture*, 63(2):173–187, 1993.

[24] G. T. Camacho and M. Ortiz. Computational modeling of impact damage in brittle materials. *International Journal of Solids and Structures*, 33(20-22):2899–2938, 1996.

[25] Zdeněk P Bažant and Yuan-Neng Li. Cohesive crack with rate-dependent opening and viscoelasticity: I. mathematical model and scaling. *International Journal of Fracture*, 86(3):247–265, 1997.

[26] Z-H Jin and CT Sun. Cohesive fracture model based on necking. *International Journal of Fracture*, 134(2):91–108, 2005.

[27] Bernard Budiansky, John C Amazigo, and Anthony G Evans. Small-scale crack bridging and the fracture toughness of particulate-reinforced ceramics. *Journal of the Mechanics and Physics of Solids*, 36(2):167–187, 1988.

[28] William W Gerberich and Eric Kurman. New contributions to the effective surface energy of cleavage. *Scripta metallurgica*, 19(3):295–298, 1985.

[29] BN Cox and DB Marshall. Concepts for bridged cracks in fracture and fatigue. *Acta Metallurgica et Materialia*, 42(2):341–363, 1994.

[30] A. de Andres, J.L. Perez, and M. Ortiz. Elastoplastic finite element analysis of three-dimensional fatigue crack growth in aluminum shafts subjected to axial loading. *International Journal of Solids and Structures*, 36:2175–2320, 1999.

[31] VS Deshpande, A Needleman, and E Van der Giessen. Discrete dislocation modeling of fatigue crack propagation. *Acta materialia*, 50(4):831–846, 2002.

[32] O Nguyen, EA Repetto, Michael Ortiz, and RA Radovitzky. A cohesive model of fatigue crack growth. *International Journal of Fracture*, 110(4):351–369, 2001.

[33] KL Roe and Th Siegmund. An irreversible cohesive zone model for interface fatigue crack growth simulation. *Engineering fracture mechanics*, 70(2):209–232, 2003.

[34] B. Yang, S. Mall, and K. Ravi-Chandar. A cohesive model for fatigue crack growth in quasibrittle materials. *International Journal of Solids and Structures*, 38:3927–3944, 2001.

[35] C Atkinson and MF Kanninen. A simple representation of crack tip plasticity: the inclined strip yield superdislocation model. *International Journal of Fracture*, 13(2):151–163, 1977.

[36] CJ Gilbert, RN Petrany, RO Ritchie, RH Dauskardt, and RW Steinbrech. Cyclic fatigue in monolithic alumina: mechanisms for crack advance promoted by

frictional wear of grain bridges. *Journal of Materials Science*, 30(3):643–654, 1995.

[37] Spandan Maiti and Philippe H Geubelle. A cohesive model for fatigue failure of polymers. *Engineering Fracture Mechanics*, 72(5):691–708, 2005.

[38] F. Armero and K. Garikipati. An analysis of strong discontinuities in multiplicative finite strain plasticity and their relation with the numerical simulation of strain localization in solids. *International Journal of Solids and Structures*, 33(20-22):2863–2885, 1996.

[39] Z. Bažant. Mechanics of distributed cracking. *Applied Mechanics Reviews*, 39:675–705, 1986.

[40] R. Larsson, K. Runesson, and N. S. Ottosen. Discontinuous displacement approximation for capturing plastic localization. *International Journal of Numerical Methods in Engineering*, 36:2087–2105, 1993.

[41] N. Ramakrishnan, H. Okada, and S. N. Atluri. On shear band formation: II. Simulation using finite element method. *International Journal of Plasticity*, 10(5):521–534, 1994.

[42] J. Oliver, A. E. Huespe., and P. J. Sanchez. A comparative study on finite elements for capturing strong discontinuities: E-FEM vs X-FEM. *Computer methods in applied mechanics and engineering*, 195:4732–4752, 2006.

[43] Sangmin Lee and Veera Sundararaghavan. Multi-scale homogenization of moving interface problems with flux jumps: application to solidification. *Computational Mechanics*, 44(3):297–307, Aug 2009.

[44] Sangmin Lee and Veera Sundararaghavan. Multi-scale modeling of moving interface problems with flux and field jumps: Application to oxidative degradation

of ceramic matrix composites. *International Journal for Numerical Methods in Engineering*, 85(6):784–804, 2011.

[45] Shang Sun, Ali Ramazani, and Veera Sundararaghavan. A hybrid multi-scale model of crystal plasticity for handling stress concentrations. *Metals*, 7(9):345, 2017.

[46] T. J. R. Hughes. Multiscale phenomena: Greens functions, the Dirichlet-to Neumann formulation, subgrid scale models, bubbles and the origins of stabilized methods. *Computer methods in applied mechanics and engineering*, 127:387–401, 1995.

[47] K. Garikipati. A variational multiscale method to embed micromechanical surface laws in the macromechanical continuum formulation. *Computer Modeling in Engineering and Sciences*, 3:175–184, 2002.

[48] S. Rudraraju, A. Salvi, K. Garikipati, and A. M. Waas. Predictions of crack propagation using a variational multiscale approach and its application to fracture in laminated fiber reinforced composites. *Composite Structures*, 94:3336–3346, 2012.

[49] C. Rocco, G. V. Guinea, J. Planas, and M. Elices. Review of the splitting-test standards from a fracture mechanics point of view. *Cement and Concrete Research*, 31:73–82, 2001.

[50] V. Yamakov, Saether, D.R. Phillips, and E.H. Glaessgen. Molecular-dynamics simulation-based cohesive zone representation of inter-granular fracture processes in aluminum. *J. Mech. Phys. Solids*, 54:1899–1928, 2006.

[51] Minghau He and Shaofan Li. An embedded atom hyperelastic constitutive model and multiscale cohesive finite element method. *Computational Mechanics*, 49(3):337–355, 2012.

[52] JC Newman Jr, Edward P Phillips, and RA Everett Jr. *Fatigue analyses under constant-and variable-amplitude loading using small-crack theory*. NASA TM 209329. 1999.

[53] H-J Christ, C-P Fritzen, and P Köster. Micromechanical modeling of short fatigue cracks. *Current Opinion in Solid State and Materials Science*, 18(4):205–211, 2014.

[54] PD Hobson. The formulation of a crack growth equation for short cracks. *Fatigue & Fracture of Engineering Materials & Structures*, 5(4):323–327, 1982.

[55] BA Bilby, AH Cottrell, and KH Swinden. The spread of plastic yield from a notch. *Proceedings of the Royal Society of London A: Mathematical, Physical and Engineering Sciences*, 272(1350):304–314, 1963.

[56] Shuji Taira, Keisuke Tanaka, and Yoshikazu Nakai. A model of crack-tip slip band blocked by grain boundary. *Mechanics Research Communications*, 5(6):375–381, 1978.

[57] K Tanaka, Y Akiniwa, Y Nakai, and RP Wei. Modelling of small fatigue crack growth interacting with grain boundary. *Engineering Fracture Mechanics*, 24(6):803–819, 1986.

[58] A Navarro and ER De Los Rios. An alternative model of the blocking of dislocations at grain boundaries. *Philosophical Magazine A*, 57(1):37–42, 1988.

[59] A Navarro and ER De Los Rios. Short and long fatigue crack growth: a unified model. *Philosophical Magazine A*, 57(1):15–36, 1988.

[60] A Navarro and ER Rios. A microstructurally-short fatigue crack growth equation. *Fatigue & Fracture of Engineering Materials & Structures*, 11(5):383–396, 1988.

[61] A Navarro and ERd Rios. A model for short fatigue crack propagation with an interpretation of the short-long crack transition. *Fatigue & Fracture of Engineering Materials & Structures*, 10(2):169–186, 1987.

[62] Christian Heinrich and Veera Sundararaghavan. A method to predict fatigue crack initiation in metals using dislocation dynamics. *Corrosion Reviews*, 35(4-5):325–341, 2017.

[63] AK Head and N Louat. The distribution of dislocations in linear arrays. *Australian Journal of Physics*, 8(1):1–7, 1955.

[64] WG Knauss. Time dependent fracture and cohesive zones. *Transactions-American Society of Mechanical Engineers Journal of Engineering Materials and Technology*, 115:262–262, 1993.

[65] David A Cendón, Filippo Berto, Paolo Lazzarin, and Manuel Elices Calafat. The cohesive crack model applied to notched pmma specimens obeying a non linear behaviour under torsion loading. In *Key Engineering Materials*, volume 577, pages 49–52. Trans Tech Publications, 2014.

[66] M Elices, GV Guinea, J Gomez, and J Planas. The cohesive zone model: advantages, limitations and challenges. *Engineering fracture mechanics*, 69(2):137–163, 2002.

[67] Alan Needleman. Some issues in cohesive surface modeling. *Procedia IUTAM*, 10:221–246, 2014.

[68] Johannes Weertman. Theory of fatigue crack growth based on a bcs crack theory with work hardening. *International Journal of Fracture*, 9(2):125–131, 1973.

[69] N Muskhelishvili and J Radok. *Singular Integral Equations: Boundary Problems of Functions Theory and Their Application to Mathematical Physics*. P. Noordhoff, Netherland, 1953.

[70] Angus J Wilkinson. Modelling the effects of texture on the statistics of stage i fatigue crack growth. *Philosophical Magazine A*, 81(4):841–855, 2001.

[71] Angus J Wilkinson. Modelling the effects of microstructure and microtexture on the statistics of short fatigue crack growth. In *ICF10, Honolulu (USA) 2001*, 2001.

[72] Edward H Glaessgen, Erik Saether, Dawn R Phillips, and Vesselin Yamakov. Multiscale modeling of grain-boundary fracture: cohesive zone models parameterized from atomistic simulations. In *Proceedings of the 47th AIAA/ASME/ASCE/AHS/ASC Structures, Structural Dynamics, and Materials Conference*, pages 1–4, 2006.

[73] Sangmin Lee and Veera Sundararaghavan. Calibration of nanocrystal grain boundary model based on polycrystal plasticity using molecular dynamics simulations. *International Journal for Multiscale Computational Engineering*, 8(5):509–522, 2010.

[74] Shardul Panwar and Veera Sundararaghavan. Dislocation theory-based cohesive model for microstructurally short fatigue crack growth. *Materials Science and Engineering: A*, 708:395–404, 2017.

[75] C Vallellano, J Vazquez, A Navarro, and J Dominguez. A micromechanical model for small fatigue crack growth: an approach based on two threshold conditions. *Fatigue & Fracture of Engineering Materials & Structures*, 32(6):515–524, 2009.

[76] W Schaef and M Marx. A numerical description of short fatigue cracks interacting with grain boundaries. *Acta Materialia*, 60(5):2425–2436, 2012.

[77] Ashley D Spear, Shiu Fai Li, Jonathan F Lind, Robert M Suter, and Anthony R Ingraffea. Three-dimensional characterization of microstructurally small fatigue-crack evolution using quantitative fractography combined with post-mortem x-ray tomography and high-energy x-ray diffraction microscopy. *Acta Materialia*, 76:413–424, 2014.

[78] Alexander Schick. *Ein neues Modell zur mechanismenorientierten Simulation der mikrostrukturbestimmten Kurzrissausbreitung*. VDI-Verlag, 2004.

[79] B Künkler, O Düber, P Köster, U Krupp, C-P Fritzen, and H-J Christ. Modelling of short crack propagation–transition from stage i to stage ii. *Engineering Fracture Mechanics*, 75(3):715–725, 2008.

[80] O Düber, B Künkler, U Krupp, H-J Christ, and C-P Fritzen. Experimental characterization and two-dimensional simulation of short-crack propagation in an austenitic–ferritic duplex steel. *International Journal of Fatigue*, 28(9):983–992, 2006.

[81] T Zhai, AJ Wilkinson, and JW Martin. A crystallographic mechanism for fatigue crack propagation through grain boundaries. *Acta materialia*, 48(20):4917–4927, 2000.

[82] T Zhai, XP Jiang, JX Li, MD Garratt, and GH Bray. The grain boundary geometry for optimum resistance to growth of short fatigue cracks in high strength al-alloys. *International journal of fatigue*, 27(10):1202–1209, 2005.

[83] C Holzapfel, W Schäf, M Marx, H Vehoff, and F Mücklich. Interaction of cracks with precipitates and grain boundaries: Understanding crack growth mecha-

nisms through focused ion beam tomography. *Scripta Materialia*, 56(8):697–700, 2007.

[84] W Schaef, M Marx, H Vehoff, A Heckl, and P Randelzhofer. A 3-d view on the mechanisms of short fatigue cracks interacting with grain boundaries. *Acta Materialia*, 59(5):1849–1861, 2011.

[85] P Köster, H Knobbe, CP Fritzen, HJ Christ, and U Krupp. A three-dimensional model for stage i-crack propagation. *Tech Mech*, 30:184–94, 2010.

[86] David Anthony Hills, PA Kelly, DN Dai, and AM Korsunsky. *Solution of crack problems: the distributed dislocation technique*, volume 44. Springer Science & Business Media, 2013.

[87] Toshio Mura. *Micromechanics of defects in solids*. Springer Science & Business Media, 2013.

[88] John D Eshelby. The determination of the elastic field of an ellipsoidal inclusion, and related problems. In *Proceedings of the Royal Society of London A: Mathematical, Physical and Engineering Sciences*, volume 241, pages 376–396. The Royal Society, 1957.

[89] Yukitaka Murakami and Sia Nemat-Nasser. Interacting dissimilar semi-elliptical surface flaws under tension and bending. *Engineering Fracture Mechanics*, 16(3):373–386, 1982.

[90] JC Lee and LM Keer. Study of a three-dimensional crack terminating at an interface. *ASME, Transactions, Journal of Applied Mechanics*, 53:311–316, 1986.

[91] DN Dai, D Nowell, and DA Hills. Partial closure and frictional slip of 3-d cracks. *International journal of fracture*, 63(1):89–99, 1993.

[92] LM Keer and CH Kuo. Cracking in a loaded, brittle elastic half-space. *International journal of solids and structures*, 29(14-15):1819–1826, 1992.

[93] PA Kelly and D Nowell. Three-dimensional cracks with dugdale-type plastic zones. *International journal of fracture*, 106(4):291–309, 2000.

[94] Philipp Köster. *Mechanismenorientierte Modellierung und Simulation der mikrostrukturbestimmten Kurzrissausbreitung unter Berücksichtigung ebener und räumlicher Aspekte*. PhD thesis, Institut fr Mechanik und Regelungstechnik - Mechatronik Universitt Siegen, 2015.

[95] J Geathers, CJ Torbet, JW Jones, and S Daly. Investigating environmental effects on small fatigue crack growth in ti–6242s using combined ultrasonic fatigue and scanning electron microscopy. *International Journal of Fatigue*, 70:154–162, 2015.

[96] Jacob F Adams, John E Allison, and J Wayne Jones. The effects of heat treatment on very high cycle fatigue behavior in hot-rolled WE43 magnesium. *International Journal of Fatigue*, 93:372–386, 2016.

[97] John Allison, Wayne Jones, and Jacob Adams. Personal Communication, 2016. Material Science and Engineering Department at University of Michigan, Ann Arbor.

[98] H Westergaard. Bearing pressures and cracks. *Journal of applied mechanics*, 18, 1939.

[99] Shardul Panwar, Shang Sun, and Veera Sundararaghavan. Modeling fatigue failure using the variational multiscale method. *Engineering Fracture Mechanics*, 162:290–308, 2016.

[100] M. Kanninen and C. Popelar. *Advanced Fracture Mechanics*. Oxford University Press, Oxford, 1985.

[101] Hermann Brunner, Arvet Pedas, and Gennadi Vainikko. The piecewise polynomial collocation method for nonlinear weakly singular volterra equations. *Mathematics of Computation of the American Mathematical Society*, 68(227):1079–1095, 1999.

[102] John T Wang. Investigating some technical issues on cohesive zone modeling of fracture. *Journal of Engineering Materials and Technology*, 135(1):011003, 2013.

[103] AH Noroozi, G Glinka, and S Lambert. A two parameter driving force for fatigue crack growth analysis. *International Journal of Fatigue*, 27(10):1277–1296, 2005.

[104] George R Irwin, Paul C Paris, and Hiroshi Tada. The stress analysis of cracks handbook. *American Society of Mechanical Engineers. Three–Park Avenue, New York, NY*, 10016, 2000.

[105] JC Newman Jr, XR Wu, SL Venneri, and CG Li. Small-crack effects in high-strength aluminum alloys. 1994.

[106] Kathleen R Dennis and Norman E Dowling. Fatigue crack growth of gun tube steel under spectrum loading. Technical report, Virginia Polytechnic Institute and State University, 1986.

[107] De Jong. *Critical stress intensity factors of an aluminum 7075 T651 alloy*. Delft University of Technology, 1977.

[108] R. Temam and G. Strang. Functions of bounded deformation. *Arch Ration Mech Analysis*, 75:7–21, 1980.

[109] J. C. Simo, J. Oliver, and F. Armero. An analysis of strong discontinuities induced by strain-softening in rate-independent inelastic solids. *Computational Mechanics*, 12:277–296, 1993.

[110] J. C. Simo and J. Oliver. A new approach to the analysis and simulation of strain softening in solids. pages 25–39, 1994.

[111] Veera Sundararaghavan and Shang Sun. *Modeling Crack Propagation in Polycrystalline Alloys using a Variational Multiscale Cohesive Method*, volume 36 of *2nd World Congress on Integrated Computational Materials and Engineering*. John Wiley and Sons, Inc, Hoboken, NJ, USA, 2013.

[112] J. R. Rice. A path independent integral and the approximate analysis of strain concentration by notches and cracks. *Journal of Applied Mechanics*, 35:379, 1968.

[113] Nestor Perez. *Fracture Mechanics*. Kluwer Academic Publisher, 2004.

[114] John Allison and J. Wayne Jones. Personal Communication, 2015. Material Science and Engineering Department at University of Michigan, Ann Arbor.

[115] S-H. Choi, D.H. Kim, S.S. Park, and B.S. You. Simulation of stress concentration in mg alloys using the crystal plasticity finite element method. *Acta Materialia*, 58(1):320–329, 2010.

[116] Caroline A Schneider, Wayne S Rasband, and Kevin W Eliceiri. NIH Image to ImageJ: 25 years of image analysis. *Nature methods*, 9(7):671–675, 2012.

[117] Stephen Langer, R. Edwin Garca, and Andrew Reid. Oof2, Nov 2007.

[118] F McBagonluri, E Akpan, C Mercer, W Shen, and WO Soboyejo. An investigation of the effects of microstructure on dwell fatigue crack growth in ti-6242. *Materials Science and Engineering: A*, 405(1):111–134, 2005.

[119] GP Marshall, LE Culver, and JG Williams. Fracture phenomena in polystyrene. *International Journal of Fracture*, 9(3):295–309, 1973.

[120] MD Skibo, RW Hertzberg, and JA Manson. Fatigue fracture processes in polystyrene. *Journal of Materials Science*, 11(3):479–490, 1976.

[121] M Marx, W Schaef, and MT Welsch. The microstructure as crack initiation point and barrier against fatigue damaging. *International Journal of Fatigue*, 41:57–63, 2012.

[122] Johannes Weertman. *Dislocation based fracture mechanics*. World Scientific Publishing Co Inc, 5 Toh Tuck Link, Singapore, 596224, 1996.

[123] A Sengupta, SK Putatunda, L Bartosiewicz, J Hangas, PJ Nailos, M Peputapeck, and FE Alberts. Tensile behavior of a new single-crystal nickel-based superalloy (cmsx-4) at room and elevated temperatures. *Journal of materials engineering and performance*, 3(1):73–81, 1994.

[124] MATLAB. *version 9.1.0.441655 (R2016b)*. The MathWorks Inc., Natick, Massachusetts, 2016.

[125] Ani Ural, Venkat R Krishnan, and Katerina D Papoulia. A cohesive zone model for fatigue crack growth allowing for crack retardation. *International Journal of Solids and Structures*, 46(11):2453–2462, 2009.

[126] Wei Wen and Tongguang Zhai. Quantification of resistance of grain boundaries to short-fatigue crack growth in three dimensions in high-strength al alloys. *Metallurgical and Materials Transactions A*, 43(8):2743–2752, 2012.

[127] J Luster and MA Morris. Compatibility of deformation in two-phase ti-al alloys: Dependence on microstructure and orientation relationships. *Metallurgical and Materials Transactions A*, 26(7):1745–1756, 1995.

[128] Ulrich Krupp. *Fatigue crack propagation in metals and alloys: microstructural aspects and modelling concepts*. John Wiley & Sons, 2007.

[129] ER De Los Rios, XJ Xin, and A Navarro. Modelling microstructurally sensitive fatigue short crack growth. In *Proceedings of the Royal Society of London A: Mathematical, Physical and Engineering Sciences*, volume 447, pages 111–134. The Royal Society, 1994.

[130] Jacob Adams. *Investigating microstructural effects on short crack growth and fatigue life behavior of WE43 Magnesium*. PhD thesis, University of Michigan, Ann Arbor, 2018.

[131] CH Caceres, Gemma E Mann, and JR Griffiths. Grain size hardening in mg and mg-zn solid solutions. *Metallurgical and Materials Transactions A*, 42(7):1950–1959, 2011.

[132] Sriram Ganesan. *Microstructural Response of Magnesium Alloys: 3D Crystal Plasticity and Experimental Validation*. PhD thesis, University of Michigan, Ann Arbor, 2017.

[133] Vito Volterra. Sur l'équilibre des corps élastiques multiplement connexes. In *Annales scientifiques de l'École normale supérieure*, volume 24, pages 401–517, 1907.

[134] Carlo Somigliana. Sulla teoria delle distorsioni elastiche. *Il Nuovo Cimento (1911-1923)*, 11(1):177–192, 1916.

[135] JD Eshelby. Elastic inclusions and inhomogeneities. *Progress in solid mechanics*, 2(1):89–140, 1961.

[136] J Hadamard. Lectures on cauchy's problem in linear differential equations new york, 1952.

[137] DN Dai, DA Hills, and D Nowell. Formulation and implementation of the eigenstrain method employing higher order elements. *International journal of solids and structures*, 33(3):331–342, 1996.

[138] Y Murakami and S Nemat-Nasser. Growth and stability of interacting surface flaws of arbitrary shape. *Engineering Fracture Mechanics*, 17(3):193–210, 1983.

[139] MK Kassir and George C Sih. Three-dimensional stress distribution around an elliptical crack under arbitrary loadings. *Journal of Applied Mechanics*, 33(3):601–611, 1966.

[140] Y Murakami. Analysis of stress intensity factors of modes i, ii and iii for inclined surface cracks of arbitrary shape. *Engineering Fracture Mechanics*, 22(1):101–114, 1985.

[141] Shang Sun and Veera Sundararaghavan. Modeling crack propagation in polycrystalline microstructure using variational multiscale method. *Mathematical Problems in Engineering*, 2016(4715696):1 – 14, 2016.

[142] Veera Sundararaghavan and Nicholas Zabaras. Design of microstructure-sensitive properties in elasto-viscoplastic polycrystals using multi-scale homogenization. *International Journal of Plasticity*, 22(10):1799 – 1824, 2006.

[143] Veera Sundararaghavan and Nicholas Zabaras. A multi-length scale sensitivity analysis for the control of texture-dependent properties in deformation processing. *International Journal of Plasticity*, 24(9):1581 – 1605, 2008.

[144] V. Sundararaghavan and A. Kumar. Probabilistic modeling of microstructure evolution using finite element representation of statistical correlation functions. *International Journal of Plasticity*, 30:62 – 80, 2012.

[145] S. Sun and V. Sundararaghavan. A peridynamic implementation of crystal plasticity. *International Journal of Solids and Structures*, 51(19):3350 – 3360, 2014.

[146] V. Sundararaghavan, A. Kumar, and S. Sun. Crystal plasticity simulations using nearest neighbor orientation correlation function. *Acta Materialia*, 93:12 – 23, 2015.

[147] Abhishek Kumar and Veera Sundararaghavan. Simulation of magnetostrictive properties of galfenol under thermomechanical deformation. *Finite Elements in Analysis and Design*, 127:1 – 5, 2017.

[148] J Luo, A Ramazani, and V Sundararaghavan. Simulation of micro-scale shear bands using peridynamics with an adaptive dynamic relaxation method. *International Journal of Solids and Structures*, 130:36–48, 2018.

[149] Pınar Acar, Ali Ramazani, and Veera Sundararaghavan. Crystal plasticity modeling and experimental validation with an orientation distribution function for ti-7al alloy. *Metals*, 7(11):459, 2017.

[150] Richard Regueiro. Embedded discontinuity finite element modeling of three-dimensional strong discontinuities in rocks. In *Golden Rocks 2006, The 41st US Symposium on Rock Mechanics (USRMS)*. American Rock Mechanics Association, 2006.

[151] Veera Sundararaghavan and Siddhartha Srivastava. Microfract: An image based code for microstructural crack path prediction. *SoftwareX*, 6:94 – 97, 2017.

[152] Veera Sundararaghavan and Nicholas Zabaras. Linear analysis of texture-property relationships using process-based representations of rodrigues space. *Acta Materialia*, 55(5):1573 – 1587, 2007.

[153] Pinar Acar and Veera Sundararaghavan. Utilization of a linear solver for multiscale design and optimization of microstructures. *AIAA Journal*, 54(5):1751 – 1759, 2016.

[154] V Sundararaghavan and N Zabaras. A dynamic material library for the representation of single-phase polyhedral microstructures. *Acta Materialia*, 52(14):4111 – 4119, 2004.

[155] V Sundararaghavan and N Zabaras. Classification and reconstruction of three-dimensional microstructures using support vector machines. *Computational Materials Science*, 32(2):223 – 239, 2005.

[156] Veera Sundararaghavan and Nicholas Zabaras. A statistical learning approach for the design of polycrystalline materials. *Statistical Analysis and Data Mining*, 1(5):306–321, 2009.

[157] Ruoqian Liu, Abhishek Kumar, Zhengzhang Chen, Ankit Agrawal, Veera Sundararaghavan, and Alok Choudhary. A predictive machine learning approach for microstructure optimization and materials design. *Scientific reports*, 5(11551):1 – 12, 2015.

[158] Arindam Paul, Pinar Acar, Ruoqian Liu, Wei-Keng Liao, Alok Choudhary, Veera Sundararaghavan, and Ankit Agrawal. Data sampling schemes for microstructure design with vibrational tuning constraints. *AIAA Journal*, 56(3):1239–1250, 2018.

[159] V Sundararaghavan and N Zabaras. On the synergy between texture classification and deformation process sequence selection for the control of texture-dependent properties. *Acta Materialia*, 53(4):1015 – 1027, 2005.

[160] Pinar Acar and Veera Sundararaghavan. Linear solution scheme for microstructure design with process constraints. *AIAA Journal*, 54(12):4022 – 4031, 2016.

[161] S. Ganesan and V. Sundararaghavan. An atomistically-informed energy based theory of environmentally assisted failure. *Corrosion Reviews*, 33(6):455 – 466, 2015.

[162] Shang Sun and Veera Sundararaghavan. A probabilistic crystal plasticity model for modeling grain shape effects based on slip geometry. *Acta Materialia*, 60(13):5233 – 5244, 2012.

[163] N Zabaras, V Sundararaghavan, and S Sankaran. An information theoretic approach for obtaining property pdfs from macro specifications of microstructural uncertainty. *TMS letters*, 3(1):1 – 4, 2006.

[164] Pinar Acar and Veera Sundararaghavan. Uncertainty quantification of microstructural properties due to variability in measured pole figures. *Acta Materialia*, 124:100 – 108, 2017.

[165] Pinar Acar and Veera Sundararaghavan. Uncertainty quantification of microstructural properties due to experimental variations. *AIAA Journal*, 55(8):2824 – 2832, 2017.

[166] Pinar Acar, Siddhartha Srivastava, and Veera Sundararaghavan. Stochastic design optimization of microstructures with utilization of a linear solver. *AIAA Journal*, 55(9):3161–3168, 2017.

[167] DN Dai, DA Hills, and D Nowell. Modelling of growth of three-dimensional cracks by a continuous distribution of dislocation loops. *Computational Mechanics*, 19(6):538–544, 1997.

[168] AEH Love. A treatise on the mathematical theory of elasticity, cambridge university press. *Cambridge,*, 1927.

[169] Raymond D Mindlin. Force at a point in the interior of a semi-infinite solid. *Physics*, 7(5):195–202, 1936.